



Topical Review

Annual research review of perovskite solar cells in 2023

Qisen Zhou¹, Xiaoxuan Liu¹, Zonghao Liu^{1,2,*}, Yanqing Zhu³, Jianfeng Lu^{3,*} , Ziming Chen⁴, Canjie Li⁴, Jing Wang⁵, Qifan Xue⁴ , Feifei He⁶, Jia Liang⁶ , Hongyu Li⁷, Shenghao Wang⁷, Qidong Tai^{8,*}, Yiqiang Zhang^{9,*}, Jiehua Liu¹⁰, Chuantian Zuo^{11,*}, Liming Ding¹¹ , Zhenghong Xiong¹², Renhao Zheng¹³, Huimin Zhang¹³, Pengjun Zhao^{13,*}, Xi Jin^{14,15}, Pengfei Wu^{16,17}, Fei Zhang^{16,17}, Yan Jiang^{14,15,*} , Huanping Zhou¹⁸, Jinsong Hu¹⁹, Yang Wang²⁰, Yanlin Song²⁰, Yaohua Mai²¹, Baomin Xu²², Shengzhong Liu²³, Liyuan Han²⁴ and Wei Chen^{1,2,*} 

¹ Wuhan National Laboratory for Optoelectronics, Huazhong University of Science and Technology, Luoyu Road 1037, Wuhan 430074, People's Republic of China

² Optics Valley Laboratory, Hubei 430074, People's Republic of China

³ State Key Laboratory of Silicate Materials for Architectures, Wuhan University of Technology, Wuhan 430070, People's Republic of China

⁴ State Key Laboratory of Luminescent Materials and Devices, Institute of Polymer Optoelectronic Materials and Devices, School of Materials Science and Engineering, South China University of Technology, Guangzhou 510640, People's Republic of China

⁵ School of Materials and Energy, Guangdong University of Technology, Guangzhou 510006, People's Republic of China

⁶ Department of Materials Science, State Key Laboratory of Photovoltaic Science and Technology, Fudan University, 220 Handan Road, Shanghai 200433, People's Republic of China

⁷ Materials Genome Institute, Shanghai University, Shangda Rd. 99, Shanghai 200444, People's Republic of China

⁸ The Institute of Technological Sciences, Wuhan University, Wuhan 430072, People's Republic of China

⁹ College of Chemistry, Zhengzhou University, Zhengzhou 450001, People's Republic of China

¹⁰ Future Energy Laboratory, School of Materials Science and Engineering, Hefei University of Technology, Hefei 230009, People's Republic of China

¹¹ Center for Excellence in Nanoscience (CAS), Key Laboratory of Nanosystem and Hierarchical Fabrication (CAS), National Center for Nanoscience and Technology, Beijing 100190, People's Republic of China

¹² School of Chemical Engineering, Center for Antibonding Regulated Crystals, Sungkyunkwan University, Suwon 16419, Republic of Korea

¹³ State Key Laboratory of Functional Materials and Devices for Special Environmental Conditions; Xinjiang Key Laboratory of Electronic Information Materials and Devices, Xinjiang Technical Institute of Physics & Chemistry, CAS, 40-1 South Beijing Road, Urumqi 830011, People's Republic of China

¹⁴ School of Materials Science and Engineering, Beijing Institute of Technology, Beijing 100081, People's Republic of China

¹⁵ Songshan Lake Materials Laboratory, Dongguan, Guangdong 523429, People's Republic of China

¹⁶ School of Chemical Engineering and Technology, Tianjin University, Tianjin 300072, People's Republic of China

¹⁷ Collaborative Innovation Center of Chemical Science and Engineering (Tianjin), Tianjin 300072, People's Republic of China

* Authors to whom any correspondence should be addressed.



Original content from this work may be used under the terms of the [Creative Commons Attribution 4.0 licence](https://creativecommons.org/licenses/by/4.0/). Any further distribution of this work must maintain attribution to the author(s) and the title of the work, journal citation and DOI.

¹⁸ Beijing Key Laboratory for Theory and Technology of Advanced Battery Materials, Key Laboratory of Polymer Chemistry and Physics of Ministry of Education, School of Materials Science and Engineering, Peking University, Beijing, People's Republic of China

¹⁹ Beijing National Laboratory for Molecular Sciences, Institute of Chemistry, Chinese Academy of Sciences, Beijing 100190, People's Republic of China

²⁰ Key Laboratory of Green Printing, CAS Research/Education Center for Excellence in Molecular Sciences, Institute of Chemistry, Chinese Academy of Sciences, Beijing 100190, People's Republic of China

²¹ Institute of New Energy Technology, College of Physics & Optoelectronic Engineering, Jinan University, Guangzhou 510632, People's Republic of China

²² Department of Materials Science and Engineering and Shenzhen Engineering Research and Development Center for Flexible Solar Cells, Southern University of Science and Technology, Shenzhen 518055, People's Republic of China

²³ Key Laboratory for Applied Surface and Colloid Chemistry, National Ministry of Education, Shaanxi Engineering Lab for Advanced Energy Technology, School of Materials Science and Engineering, Shaanxi Normal University, Xi'an 710119, People's Republic of China

²⁴ State Key Laboratory of Metal Matrix Composites, Shanghai Jiao Tong University, Shanghai 200240, People's Republic of China

E-mail: liuzonghao@hust.edu.cn, jianfeng.lu@whut.edu.cn, qdtai@whu.edu.cn, yqzhang@zzu.edu.cn, zuocht@nanoctr.cn, zhaopj@ms.xjb.ac.cn, yan.jiang@bit.edu.cn and wnlochenwei@mail.hust.edu.cn

Received 1 April 2024, revised 19 April 2024

Accepted for publication 22 April 2024

Published 31 May 2024



Abstract

Perovskite (PVK) solar cells (PSCs) have garnered considerable research interest owing to their cost-effectiveness and high efficiency. A systematic annual review of the research on PSCs is essential for gaining a comprehensive understanding of the current research trends. Herein, systematic analysis of the research papers on PSCs reporting key findings in 2023 was conducted. Based on the results, the papers were categorized into six classifications, including regular n-i-p PSCs, inverted p-i-n PSCs, PVK-based tandem solar cells, PVK solar modules, device stability, and lead toxicity and green solvents. Subsequently, a detailed overview and summary of the annual research advancements within each classification were presented. Overall, this review serves as a valuable resource for guiding future research endeavors in the field of PSCs.

Keywords: perovskite solar cells, annual review, systematic review

Contents

1. Introduction	3	3.2.1. HTL and buried interface	10
2. Regular n-i-p PSCs	3	3.2.2. Management of the bulk properties of PVK films	11
2.1. Brief introduction	4	3.2.3. Surface modification	12
2.2. Organic-inorganic PSCs	4	3.2.4. Other strategies	13
2.2.1. ETL and buried interface	4	3.3. Inorganic 3D PSCs	13
2.2.2. PVK film management	6	3.3.1. Charge-transporting layer	13
2.2.3. Surface modification	7	3.3.2. Surface modification	13
2.2.4. Others	7	3.3.3. Other methods	14
2.3. Inorganic PSCs	7	3.4. Sn-based PSCs	14
2.3.1. ETL and buried interface	7	3.5. 2D PSCs	16
2.3.2. PVK film management	7	3.5.1. Design of novel organic spacer cations	16
2.3.3. Surface modification	8	3.5.2. Regulation of crystallization kinetics	18
2.4. Sn-based PSCs	8	3.5.3. Exploration of 2D Pb-Sn mixed PVKs	18
3. Inverted p-i-n PSCs	9	3.5.4. Niche research directions of 2D PVKs	19
3.1. Brief introduction	9	3.6. Single-crystal based PSCs	20
3.2. Organic-inorganic 3D PSCs	10	3.6.1. Organic molecule inducing method	20
		3.6.2. Crystal interface inducing method	21

3.7. Flexible PSCs (FPSCs)	21
3.7.1. PVK film management	21
3.7.2. Modification of buried interfaces	21
4. PVK-based TSCs	22
4.1. Brief introduction	22
4.2. 2T PVK/silicon TSCs	22
4.3. 2T PVK/PVK TSCs	22
4.4. 2T PVK/organic TSCs	23
4.5. 4T TSCs	24
4.6. Summary	25
5. PSMs	25
5.1. Brief introduction	25
5.2. Blade coating	25
5.3. Slot-die coating	25
5.4. Spray coating	27
5.5. Inkjet printing	28
5.6. Screen printing	29
5.7. Vapor deposition	29
6. Device stability	29
6.1. Brief introduction	29
6.2. Humidity stability	30
6.3. Thermal stability	31
6.4. Light soaking stability	32
6.5. Operational conditions	33
6.6. Radiation and mechanical stability	34
6.7. Future perspectives	35
7. Lead toxicity and green solvents	35
7.1. Brief introduction	35
7.2. Eco-friendly device processing	35
7.3. Mitigation of lead leakage during device operation	40
7.4. Summary	42
8. Future perspectives	42
References	43

1. Introduction

Due to the advantages of low cost and high efficiency, perovskite (PVK) solar cells (PSCs) have developed rapidly, and many key findings related to their development are reported every year. A systematic annual review of research papers with notable findings is essential for researchers to stay informed about the latest advancements in PSC research and for guidance for related future studies. For literature retrieval, the following journals were searched with ‘perovskite’ as the theme and ‘2023’ as the publication year. The retrieved papers were then screened individually, with a focus on selecting those related to PSCs. As shown in figure 1, 290 papers were identified across various journals, including Nature (13 papers), Nature Energy (13 papers), Nature Photonics (2 papers), Nature Sustainability (3 papers), Nature Communications (9 papers), Science (11 papers), Joule (7 papers), Energy & Environmental Science (19 papers), Advanced Materials (54 papers), Advanced Energy Materials (26 papers), Advanced Functional Materials

(37 papers), Angewandte Chemie International Edition (19 papers), Journal of the American Chemical Society (8 papers), ACS Energy Letters (33 papers), ACS Nano (1 paper), Nano Letters (3 papers), Chem (1 paper), Matter (6 papers), Nano Energy (8 papers), and some other journals (17 papers).

Subsequently, a categorization system was established for literature pertaining to PSCs, encompassing six classifications: regular n–i–p PSCs, inverted p–i–n PSCs, PVK-based tandem solar cells (TSCs), PVK solar modules (PSMs), device stability, and lead toxicity and green solvents. The statistical diagram of the number of papers related to these six classifications is shown in figure 2. Regular n–i–p PSCs were classified by focusing on research related to PSCs with n–i–p device structures, comprising 50 papers. The inverted p–i–n PSCs were classified by focusing on studies centered on PSCs with p–i–n device structures, totaling 108 papers. Regular n–i–p PSCs and inverted p–i–n PSCs were classified by focusing on research reporting on the methods for improving the device efficiency. Similarly, PVK-based TSCs were classified by focusing on PVK-related TSCs, including PVK/silicon TSCs, PVK/PVK TSCs, PVK/organic TSCs, and PVK/copper indium gallium selenide (CIGS) TSCs, totaling 46 papers. For PSM classification, research on large-scale PSMs were focused on, with a total of 13 papers. Device stability was classified by focusing on research that reported on improving the stability of PSC devices, with a total of 60 papers. Lead toxicity and green solvents were classified by focusing on studies related to lead toxicity and its alternative methods, as well as the advancement of green solvents, with a total of 13 papers. It is noted that Sn–Pb mixed PSCs and pure Sn-based PSCs are not included in this category but summarized in the n–i–p PSCs, p–i–n PSCs, TSC, or device stability category. Each article is assigned to a single category based on its primary research focus. This review comprehensively summarizes the latest progress on PSCs in 2023 based on these classifications gain a thorough understanding of current research trends in PSCs and offer guidance for future research in this field.

2. Regular n–i–p PSCs

Jianfeng Lu¹, Yanqing Zhu¹, Ziming Chen², Canjie Li², Qifan Xue², Jing Wang³, Feifei He⁴, Jia Liang⁴, Hongyu Li⁵ and Shenghao Wang⁵

¹ State Key Laboratory of Silicate Materials for Architectures, Wuhan University of Technology, Wuhan 430070, People’s Republic of China

² State Key Laboratory of Luminescent Materials and Devices, Institute of Polymer Optoelectronic Materials and Devices, School of Materials Science and Engineering, South China University of Technology, Guangzhou 510640, People’s Republic of China

³ School of Materials and Energy, Guangdong University of Technology, Guangzhou 510006, People’s Republic of China

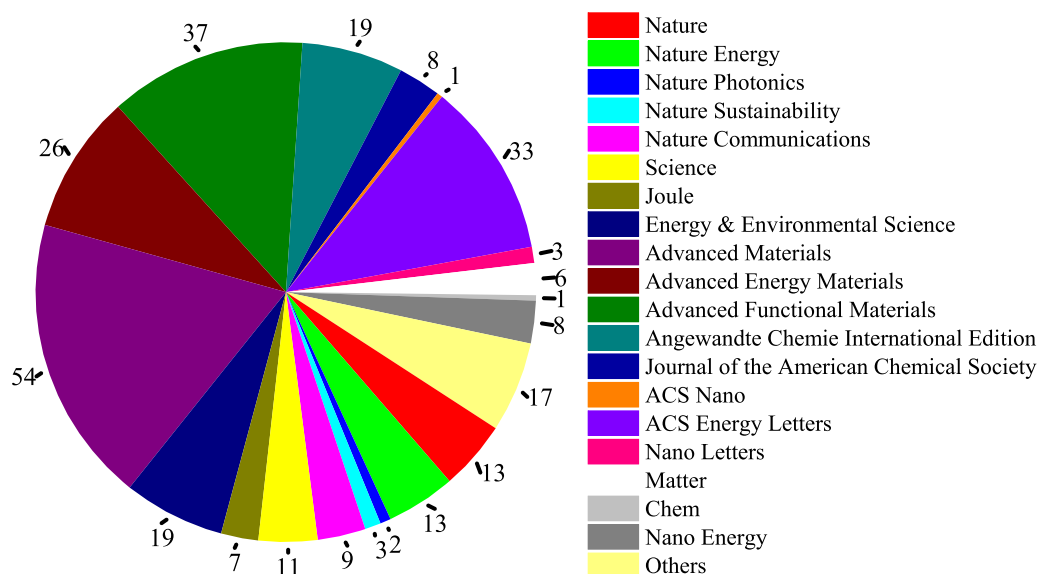


Figure 1. Statistical diagram of papers related to PSCs used in this review.

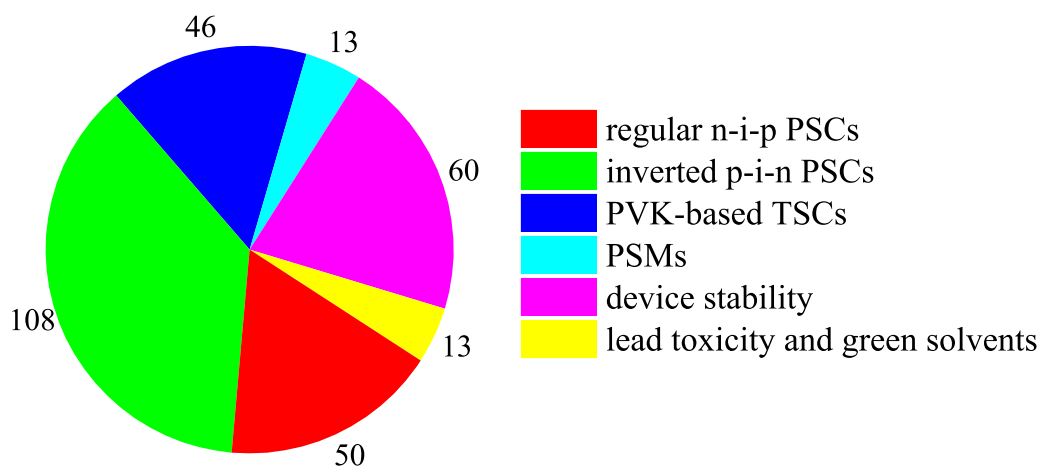


Figure 2. Statistical diagram of related papers in six classifications published in 2023.

⁴ Department of Materials Science, State Key Laboratory of Photovoltaic Science and Technology, Fudan University, 220 Handan Road, Shanghai 200433, People's Republic of China

⁵ Materials Genome Institute, Shanghai University, Shangda Rd. 99, Shanghai 200444, People's Republic of China

2.1. Brief introduction

The efficiency of PSCs has continuously increased over the past year. Figure 3 shows the representative proceedings on regular PSCs in 2023. These studies mainly focus on crystal regulation of PVK, optimization of charge transport layer, and improvement of interface properties, thereby further enhancing the photovoltaic performance of PSCs [1–5]. Figure 4(a) shows the efficiency record of small cells (0.08 cm²) based on the regular n-i-p structure reported in 2023 is 25.80%, demonstrating the high competitiveness of n-i-p structure. The efficiency improvements in 2023 are attributed to factors such as the use of advanced

film deposition techniques and new passivation strategies. The latest advances in n-i-p PSCs based on organic–inorganic, inorganic, and Sn-based PVKs are described herein from the perspectives of electron transport layers (ETLs) and buried interfaces, PVK film management, and surface modification.

2.2. Organic–inorganic PSCs

2.2.1. ETL and buried interface. Studies conducted in 2023 on the ETLs in n-i-p PSCs primarily focused on adjusting band structures and surface states via doping [6, 7] and interface modification [8–10]. These modifications successfully passivated interface defects and enhanced charge carrier extraction and transport capabilities, ultimately yielding high-performance devices.

To passivate the buried interface defects and improve charge transfer. Xu *et al* [9] codoped Nb⁵⁺ and Ta⁵⁺ in the involved SnO₂ substrate, which effectively tuned its

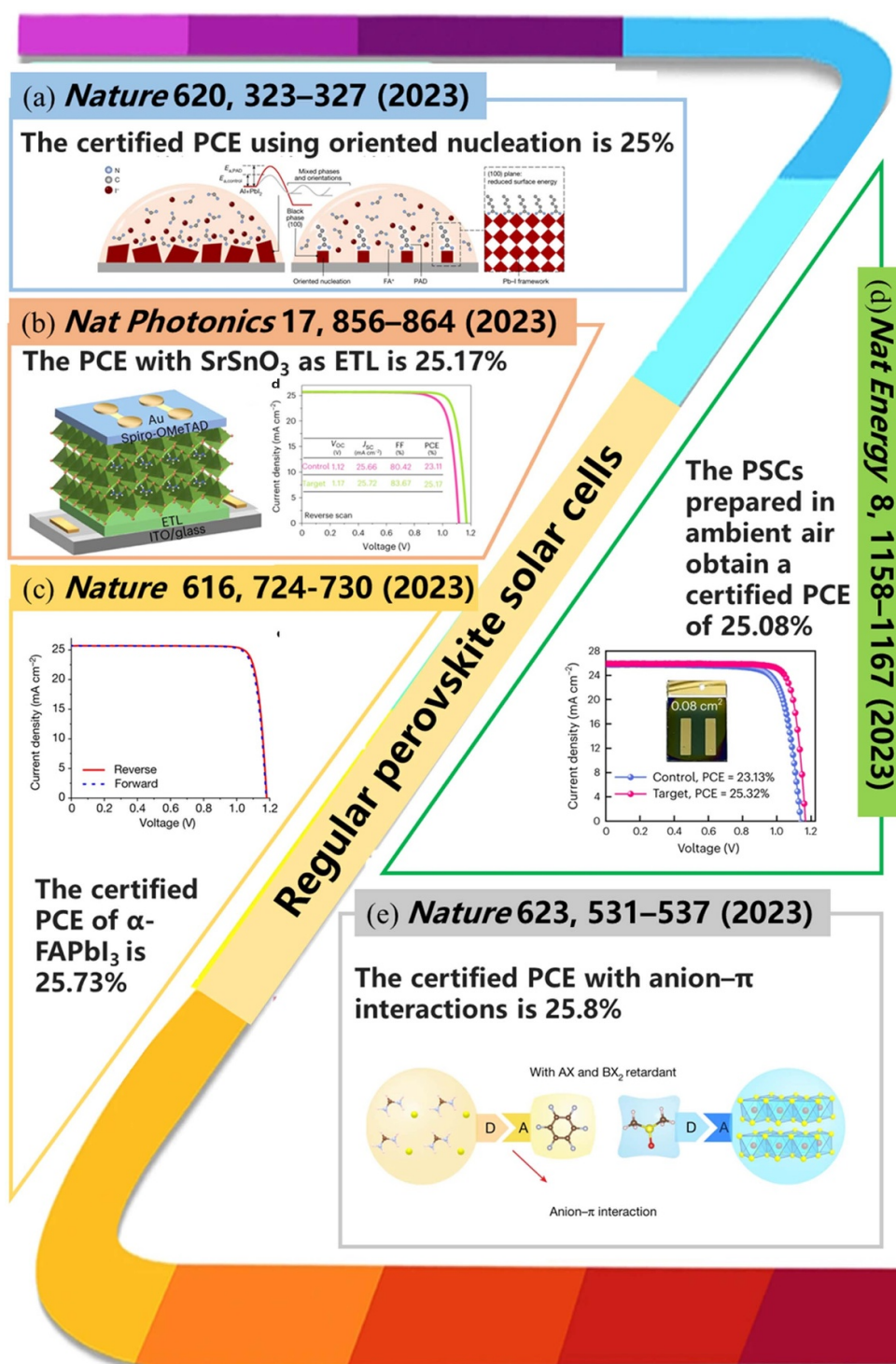


Figure 3. Representative proceedings on regular PSCs in 2023. (a)–(e) Reproduced from [1–5], respectively, with permission from Springer Nature.

optoelectronic properties such as conductivity, carrier mobility, trap states, and energy levels. The low surface roughness of the SnO_2 substrate improved the crystallinity of PVK films, and they achieved an impressive power conversion efficiency (PCE) of 25.30%. Luo *et al* suggested that ETLs may influence the initiation of disordered growth of PVK films at the buried

interface, and they synthesized a new PVK oxide (SrSnO_3) as an ETL (figure 4(b)). The high lattice matching between SrSnO_3 and PVK enabled ordered growth of FAPbI_3 PVKs, preventing the formation of defects at the buried interface. This buried interface reduced the ion migration of PVK films. The best-performing PSCs had PCE of 25.17% [2].

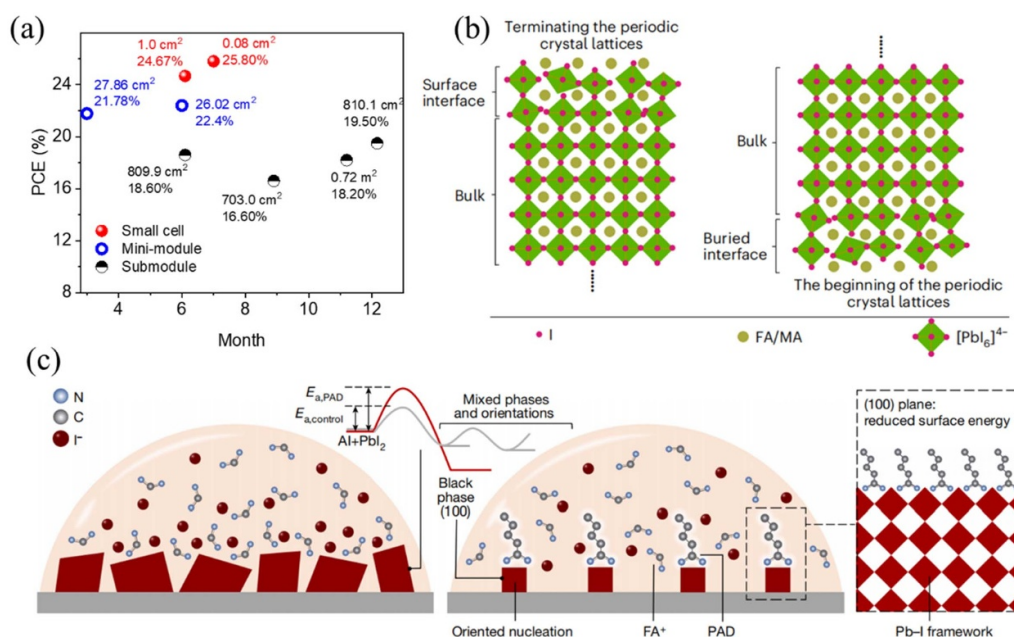


Figure 4. (a) Efficiencies of small cells (red), mini-modules (blue), and submodules (black) recorded in 2023 [5, 11]. (b) ETL initiated disordered growth of PVK films at the buried interface. Reproduced from [2], with permission from Springer Nature. (c) Schematic of the thermodynamic driving force and the kinetics of the oriented nucleation of PVK films. Reproduced from [1], with permission from Springer Nature.

2.2.2. PVK film management. In 2023, most high-efficiency PSCs used FAPbI₃ PVK as the light absorber [1, 5, 12, 13]. Additive inducing oriented nucleation, seed-mediated growth, and 2D/3D heterostructure construction were adopted to inhibit the lattice distortion of PVK crystals and realize phase-stable FAPbI₃ PVK, thus ensuring effective PVK film management.

2.2.2.1. Oriented nucleation. Introducing additives into the precursor solution to induce oriented nucleation in PVKs along one of the crystal faces is an effective method for the formation of stable black phase α -FAPbI₃ [1, 14–17]. Shi *et al* [1] introduced pentanamidine hydrochloride (PAD) into the organic cation precursor and *in situ* monitored the crystallization of PVK. They observed that PAD effectively eliminated the intermediate phase, induced oriented nucleation along the (100) crystal face, and prevented the formation of yellow phase in PVKs (figure 4(c)). The resulting PSCs exhibited a PCE of 25.4%. Oriented nucleation can also be achieved via antisolvent engineering [13, 18]. Sun *et al* used isopropanol (IPA) as an antisolvent [13], which interacted with PbI₂. Thus, PbI₂ exhibited a corner-sharing structure rather than an edge-sharing octahedral, which suppressed the formation of an intermediate phase. When the IPA evaporated, FA⁺ replaced it to form α -FAPbI₃ along the (111) direction. Compared with randomly oriented PVKs, the (111)-oriented PVK exhibited improved carrier mobility, a more-uniform surface potential, lesser film defects, and enhanced photostability.

2.2.2.2. Seed-mediated growth. PVK nanocrystals (NCs) exhibit notable advantages in optimizing the film quality when used as additives; their composition and lattice structure are similar to those of bulk PVK matrix. They can serve as seeds for heterogeneous crystallization and film growth, which can modify microstructures and nanoscale structures of the PVK host. Importantly, the addition of PVK NCs can effectively suppress phase transitions. Hu *et al* [19] incorporated butylamine-capped CsPbI₃ nanocrystals (BPNCs) as an additive in PSCs. These BPNCs acted as nucleation sites during PVK film growth, facilitating the growth of larger grains, relieving lattice strain, and promoting carrier transport. Thus, PSCs incorporating BPNCs achieved a champion PCE of up to 25.41%.

2.2.2.3. 2D/3D heterostructures. The formation of 2D/3D heterostructures positively impacts the device stability but may be detrimental for charge transport at the interfaces. Yang *et al* [20] designed a 2D/3D heterostructure based on the FAPbI₃ PVK and an amidino-based Dion–Jacobson (DJ)-type 2D PVK ((4AP)PbI₄, 4AP = 4-aminopyridine). 4AP-based DJ PVKs have a more flexible adjacent $[PbI_6]^{4-}$ linkages and the higher tolerance to lattice distortion than traditional amino analogs. Therefore, they yield a more stable PVK crystal structure and more efficient charge transport. PSCs based on 2D/3D heterostructures have the highest efficiencies of 24.9% and 22.3% on rigid and flexible substrates, respectively, among all 2D/3D composite solar cells.

2.2.3. Surface modification. The nonradiative recombination losses at the PVK surface considerably impact the V_{oc} and fill factor (FF) of PSCs [21]. Therefore, efficient interface passivators have been developed to minimize voltage losses [22–24]. You *et al* designed a bifunctional molecule (CBz–PAI) containing carbazole-triphenylamine (CBz) and phenylammonium iodide (PAI) moieties to passivate the defects on the PVK film surface [22]. Due to the favorable energy level alignment with PVK, CBz–PAI functioned as a hole shuttle between the PVK layer and hole transport layer (HTL) and minimized the quasi-Fermi level splitting of the PVK, reducing voltage losses. By modifying CBz–PAI, the solar cell achieved a stabilized PCE of 24.7%. Dual-interface modulation can realize the dual management of the buried interface and surface, which are key to obtaining high photovoltaic performance in lead halide PSCs [25–27]. Guo *et al* [25] reported a strategy for dual-interface modulation using functional covalent organic frameworks (COFs). Specifically, the COFs at the buried interface could improve the order of PVK crystal growth, release the tensile strain of PVKs, and enhance the resistance of devices to ultraviolet radiation. In addition, they reported that COFs on the surface can passivate surface defects and inhibit nonradiative recombination. Benefiting from these merits, the modified device achieved a champion PCE of 24.26%.

2.2.4. Others. Spiro-OMeTAD is a commonly used material in high-efficiency n–i–p PSCs. However, these PSCs are vulnerable at high temperatures ($>85\text{ }^{\circ}\text{C}$) [28]. Therefore, stabler HTLs are being designed to replace spiro-OMeTAD. He *et al* [29] designed a semiconducting polymer (p-O5H-E-POZ-E) and used it as the HTL. Compared to spiro-OMeTAD and poly-[bis(4-phenyl)(2,4,6-trimethylphenyl)amine] (PTAA), p-O5H-E-POZ-E showed superior properties such as excellent film morphology, high conductivity, and high glass-transition temperature ($187\text{ }^{\circ}\text{C}$). It also exhibited high elastic modulus and fracture strength and reduced water penetration in its composite film. Using P-doped p-O5H-E-POZ-E composites as the HTL, PSCs achieved high PCE of 24.9% and thermostability at $85\text{ }^{\circ}\text{C}$.

2.3. Inorganic PSCs

Compared with organic–inorganic hybrid PVKs, all-inorganic PVKs have strong resistance to environmental stresses such as high temperature and humidity. CsPbX_3 PSCs were first proposed with a modest PCE of 2.9% in 2015 [30]; their PCE has reached 21.59% in just a decade [31]. CsPbX_3 PVKs can be classified into four categories depending on halide composition: CsPbI_3 , CsPbI_2Br , CsPbIBr_2 , and CsPbBr_3 . These PVKs have high PCEs of 21.59%, 17.7%, 15.54%, and 11.08%, respectively, in the n–i–p structure in addition to other advantages and drawbacks [31–35]. However, all-inorganic

PVKs have low PCE, which can be addressed using different approaches such as by optimizing their structure via different methods such as additive-assisted airflow drying method [36], adding passivators such as surface passivation agents and bulk passivators [37], optimizing the composition of the carrier transport layer [38], adding different layer structures [39], fabricating PVK–PVK stacks [40], and optimizing the ratio between alloy PVK atoms. These methods have effectively improved the photoelectric conversion efficiency of PSCs; however, they have not yet reached the Shockley–Queisser (S–Q) limit of 33.7%. Therefore, the current research progress on all-inorganic PVKs must be summarized to suggest future developments.

2.3.1. ETL and buried interface. The ETL of inorganic PSCs has been extensively studied. TiO_2 was first used as the ETL owing to its excellent mobility and stability. However, it has energy level mismatch and unavoidable defects, which are substantial drawbacks. The energy level of TiO_2 can be effectively enhanced by doping it with other metals. Besides, SnO_2 , ZnO , and composite layers can be used as ETLs. Recently, Luo *et al* suggested using a Ti-doped ZnO thin film (TZO) as a cathode buffer layer to optimize the energy level alignment between SnO_2 and ITO, thereby enhancing the carrier transport efficiency (figures 5(a) and (b)) [41]. This buffer layer is a highly effective material for interface modification.

2.3.2. PVK film management. Additive engineering and solvent engineering are pivotal strategies for enhancing the quality of PVK films. In line with the recent advancements in inorganic devices, Ren *et al* incorporated sodium formate into the CsPbI_2Br PVK precursor solution to effectively enhance the crystallinity of PVKs and reduce defects [35]. Liu *et al* introduced bis(triphenylphosphine)iminium bis(trifluoromethyl-sulfonyl)imide ([PPN][TFSI]) to inhibit the degradation of the PVK phase and achieve stable CsPbI_3 films in an ambient environment [43]. Yue *et al* incorporated cesium cyclopropane acid (C3) into the PVK to enhance its moisture resistance [44]. Sun *et al* introduced lead acetate (PbAc_2), which effectively reduced the crystallization barrier of the PVK [37]. Wang *et al* introduced bis(pentafluorobenzene)zinc ($\text{Zn}(\text{C}_6\text{F}_5)_2$) into the antisolvent (CB), which can suppress PVK phase segregation and hinder ion migration [45]. Wu *et al* introduced ammonium chloride (MACl) to alter the crystallization path of the PVK [46]. Zhang *et al* introduced a dye (rhodamine bisothiocyanate, RBITC) to regulate PVK crystallization and passivate defects (figures 5(c) and (d)) [42]. Additionally, Xiao *et al* developed a unique film processing method, wherein a PVK film with low defect density and no pinholes was obtained by airflow drying and the addition of lead acetate trihydrate [36].

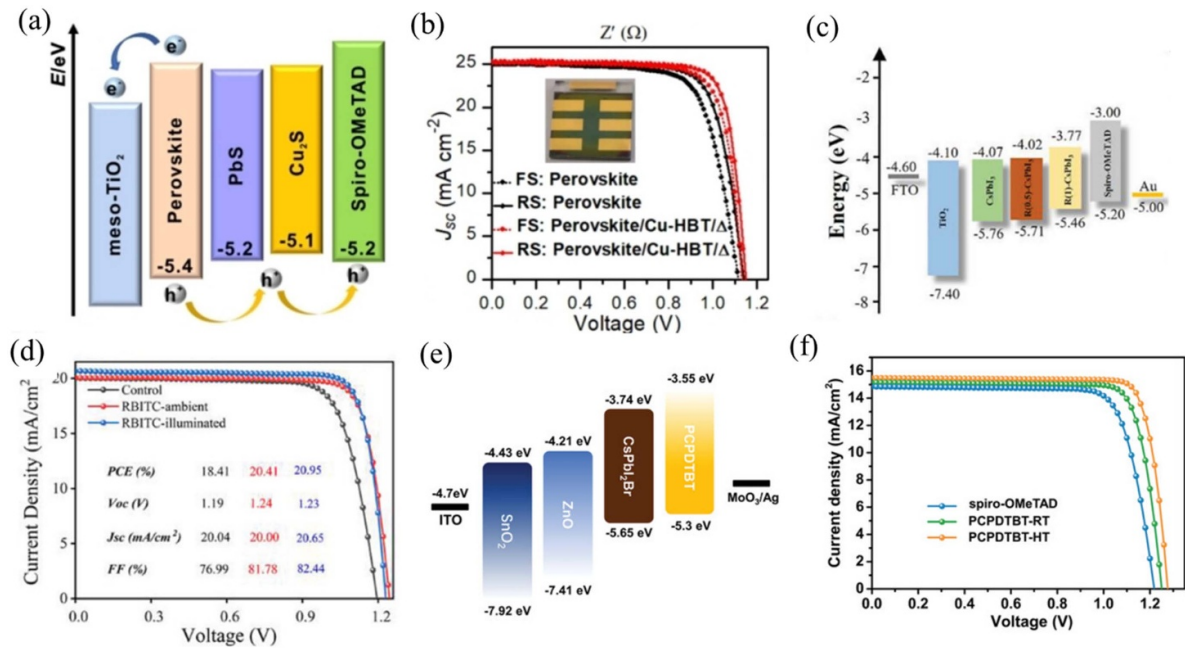


Figure 5. (a) Energy levels of perovskite, PbS, Cu₂S and spiro-OMeTAD and (b) best $J-V$ data tested in reverse (RS) and forward (FS) scans of PSCs of pristine PSC device and treated by Cu-HBT after thermal treatment; (a), (b) [39] John Wiley & Sons. © 2023 Wiley-VCH GmbH. (c) The energy levels of fabricated CsPbI₂Br-based PSCs and (d) $J-V$ characteristics of devices with different HTLs; (c), (d) [42] John Wiley & Sons. © 2023 Wiley-VCH GmbH. (e) The schematic energy level alignment of TiO₂, perovskite films, HTL and Au electrode and (f) $J-V$ curves under 100 mW cm⁻² irradiation (AM 1.5) condition. (e), (f) [38] John Wiley & Sons. © 2023 Wiley-VCH GmbH.

2.3.3. Surface modification. Surface defects in inorganic PVKs have persistently posed considerable challenges. These defects can induce nonradiative recombination and primarily contribute to the loss of overall PCE. Defect passivation is the most prevalent surface modification method, wherein small molecules or polymers are introduced such as bidentate ligand 2,2'-Bipyridine (2Bipy), Boc-S-4-methoxybenzyl-L-cysteine (BMBC), polylactic acid (PLA), trifluoroacetamide (TFA), and 2-(4-aminophenyl) ethylamine cations [47–51].

Other surface modification methods have also undergone developments. For instance, Ren *et al* proposed ethyl formate (EC) antisolvent engineering, which not only adjusts the crystallinity of PVK but also utilizes residual EC for passivation and energy level optimization [52]. Liu *et al* introduced biocompatible material tryptamine (TA) as a dopant to spiro-OMeTAD for defect passivation. Concurrently, TA inhibited the reaction between HTL and water, thereby enhancing its water stability [53]. Chu *et al* developed an *in situ* surface reactivation strategy for PVKs treated with CsF, effectively passivating the defects [54]. Suitable hole transport materials doped with hygroscopic additives are being researched to replace spiro-OMeTAD. Recently, non-doped poly[2,6-(4,4-bis(2-ethylhexyl)-4H-cyclopenta[2,1-b;3,4-b']dithiophene)-alt-4,7-(2,1,3-benzothiadiazole)] (PCPDTBT) has been reported as an effective surface modification strategy (figures 5(e) and (f)) [38].

2.4. Sn-based PSCs

Advancements in Sn-based PSCs (TPSCs) have predominantly focused on p-i-n structured devices in 2023 and their n-i-p counterparts. Notably, Hu *et al* established a new efficiency benchmark for n-i-p devices with remarkable performance (figure 6(a)) [55]. They substituted the conventional dopant, lithium bis(trifluoromethanesulfonyl) imide (Li-TFSI), in spiro-OMeTAD with 4-isopropyl-4'-methylidiphenyliodonium tetrakis(pentafluorophenyl)borate (DPI-TPFB) and achieved an impressive solar cell efficiency of 10.9% (figure 6(b)). This outstanding performance was due to the enhanced electrical conductivity facilitated by DPI-TPFB, acting as a Lewis acid, and its coordination with Sn²⁺ ions on the FASnI₃ surface (figure 6(c)).

Besides organic-inorganic Sn-based PVKs, the all-inorganic orthorhombic phase CsSnI₃ stands out as a Sn-based PVK material with desirable properties for PSCs. With a band gap of 1.3 eV close to the S-Q limit, CsSnI₃ is well-suited for efficient light absorption [57]. It does not contain volatile organic cations, such as MA⁺ and FA⁺, which contribute to its good intrinsic thermal stability. However, Sn-based PVK materials have challenges similar to those in organic-inorganic Sn-based PVKs, such as rapid crystallization, easy oxidation of Sn²⁺ to Sn⁴⁺, and low formation energy of Sn²⁺ vacancies [58]. To address these challenges and enhance the efficiency and stability of CsSnI₃ PSCs, the PVK films are optimized. One common strategy involves adding additives that interact

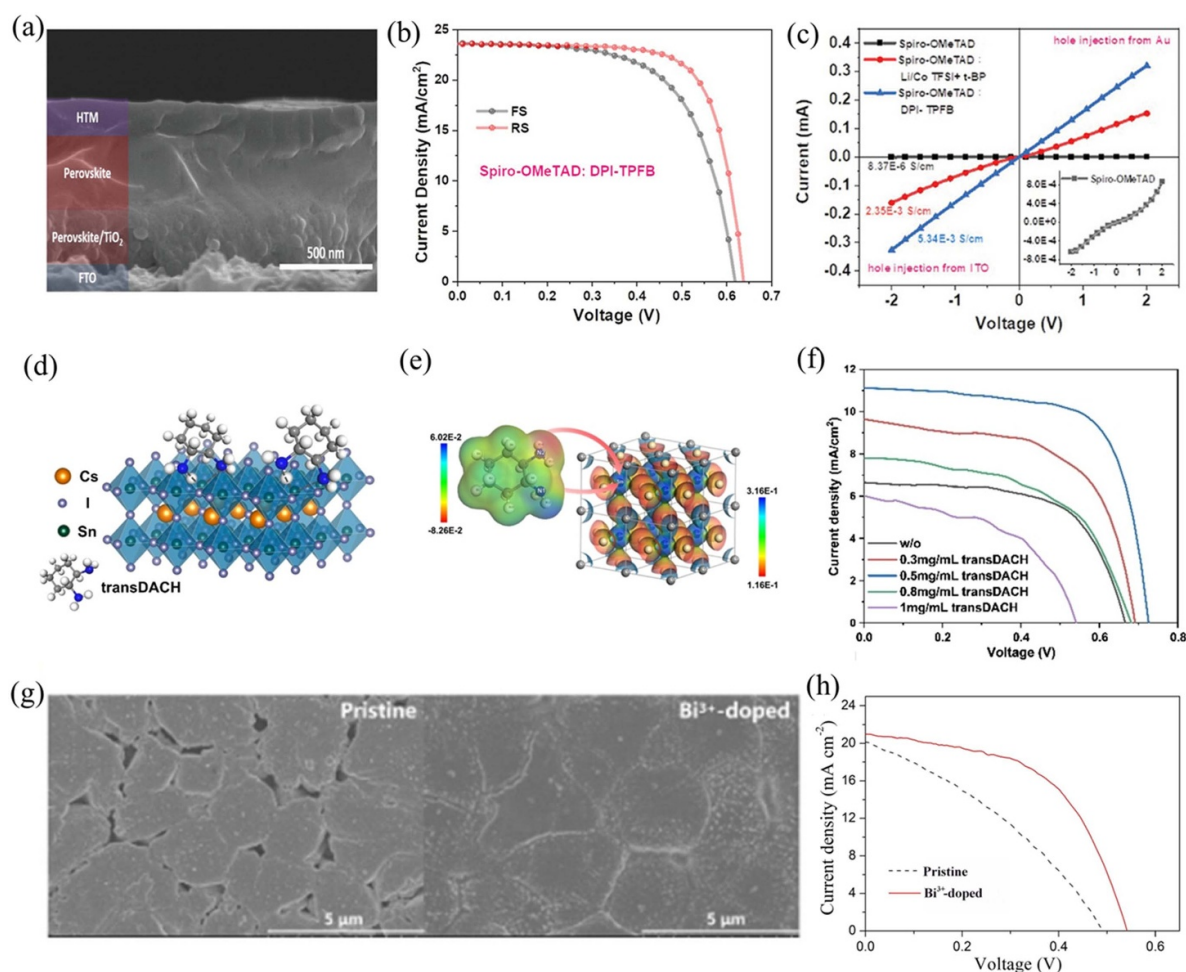


Figure 6. (a) Cross-sectional SEM image. (b) J - V curves of the highest-performing PSCs. (c) Electrical conductivity of the HTM films of spiro-OMeTAD doped by Li/Co/t-BP and DPI-TPFB. The inset shows the undoped spiro-OMeTAD film. (a)–(c) [55] John Wiley & Sons. © 2023 Wiley-VCH GmbH. (d) Schematic of the interaction between transDACH and CsSnI_3 . (e) Electrostatic potential surfaces of CsSnI_3 and CsSnI_3 -transDACH (negative and positive electrostatic potentials are indicated in red and blue, respectively). (f) J - V curves of champion CsSnI_3 -based PSCs doped with various transDACH contents. (d)–(f) [27] John Wiley & Sons. © 2022 Wiley-VCH GmbH. (g) SEM images of pristine and Bi^{3+} -doped CsSnI_3 PVK films. (h) J - V curves of PSCs with pristine and Bi^{3+} -doped CsSnI_3 PVKs. (g), (h) Reprinted from [56], © 2023 Elsevier B.V. All rights reserved.

with Sn^{2+} into the PVK precursor solution, which decelerate film crystallization and improve antioxidant capacity [59]. For instance, Yang *et al* found that two lone electrons on the $-\text{NH}_2$ of (1 R, 2 R)-(—)-1,2-diaminocyclohexane (transDACH) exhibited the strongest negative potential, whereas CsSnI_3 had a positive electrostatic potential near Sn^{2+} (figures 6(d) and (e)). Therefore, upon introducing transDACH into the CsSnI_3 precursor solution, a denser corresponding film was obtained due to the interaction between transDACH and Sn^{2+} . The PCE of this CsSnI_3 -transDACH device prepared in air reached 5.49% (figure 6(f)) [27].

Composition engineering is another effective approach for the direct modification of material properties [59]. Meng *et al* found that by incorporating Bi^{3+} ions into the CsSnI_3 lattice, larger grains and considerably denser film surface can be obtained (figure 6(g)). Owing to Bi^{3+} doping, the PCE of the device increased from 3.44% to 6.11% (figure 6(h)); the device showed enhanced air stability [56].

3. Inverted p-i-n PSCs

Qidong Tai¹, Yiqiang Zhang² and Jiehua Liu³

¹ The Institute of Technological Sciences, Wuhan University, Wuhan 430072, People's Republic of China

² College of Chemistry, Zhengzhou University, Zhengzhou 450001, People's Republic of China

³ Future Energy Laboratory, School of Materials Science and Engineering, Hefei University of Technology, Hefei 230009, People's Republic of China

3.1. Brief introduction

Compared with regular PSCs, inverted PSCs (IPSCs) are more favorable for commercial production owing to their advantages of excellent stability, negligible hysteresis, and low-temperature manufacturing. Benefiting from the intense research efforts in recent years, IPSCs have

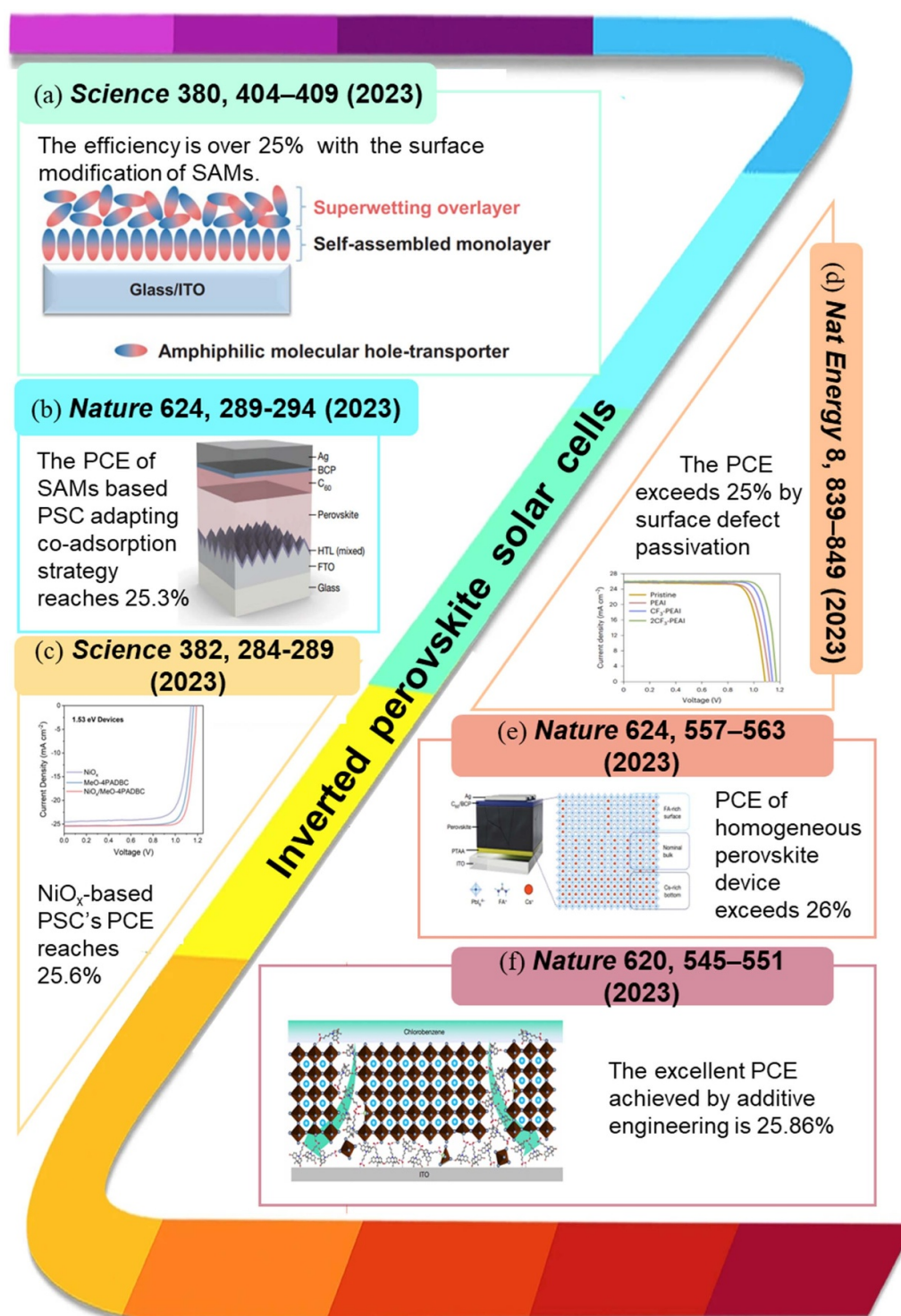


Figure 7. Representative proceedings on Pb-based inverted PSCs in 2023 [60–65]. (a), (c) From [60]. Reprinted with permission from AAAS. From [61]. Reprinted with permission from AAAS. (b), (d)–(f) Reproduced from [62], with permission from Springer Nature. Reproduced from [63], with permission from Springer Nature. Reproduced from [64]. CC BY 4.0. Reproduced from [65], with permission from Springer Nature.

similar PCEs to that of regular PSCs (figure 7). In this section, we will summarize the most astonishing achievements on IPSCs in the last year and the PVK types used in these devices, focusing on different technologies used for performance enhancement.

3.2. Organic–inorganic 3D PSCs

3.2.1. HTL and buried interface. HTLs are crucial in transporting holes and blocking electrons in PSCs. For n–i–p PSCs, HTL deposition on the PKK layer requires various suitable

properties, including energy levels matched with PVK to ensure effective hole extraction and electron blocking, not damaging the quality of PVK to prevent its decomposition, excellent conductivity for efficient hole transport. For p-i-n IPSCs, a PVK layer is deposited on the involved HTL, wherein the HTL directly affects the film formation and morphology of PVK [66, 67]. Therefore, the selection of suitable HTL materials and tailoring the HTL/PVK interface (buried interface) in IPSCs are crucial [68–70]. In addition to the properties similar to the HTL of n-i-p PSCs mentioned above, the HTL of p-i-n IPSCs also needs to have unique properties, including wettability suitable for the growth of high-quality PVK films, and high transmittance to reduce incident light loss. Although several HTL materials have been explored for IPSCs, PTAA and self-assembled monolayer (SAM) organic HTLs [60, 71] and nickel oxide (NiO_x) inorganic HTLs have been explored [60, 61, 72].

PTAA has long been used in IPSCs and has demonstrated excellent efficiency and stability. However, its poor surface wettability and defect-rich buried interface caused by small PVK crystals remain a challenge for its further development [73, 74]. Zhang *et al* improved the surface wettability of PTAA using PFN-Br to modify the PTAA surface and obtained high-quality PVK films by passivating the bottom PVK halide vacancy with Br groups [75, 76]. Zhu *et al* modified PTAA via the interfacial functionalization of the organometallic compound ferrocene-dithiophene-2-carboxylate (FCTC2). FCTC2 reduced the trap state of the buried interface via Pb-O binding and accelerated the hole extraction via its own functional group. The final device achieved a PCE of 25% and maintained >98% of its initial efficiency in long-term operational stability tests with continuous 1-sun illumination for >1500 h [71]. Pan *et al* proposed a carrier viaduct strategy using an interfacial molecular bridge comprising $\text{Ph-CH}_2\text{N}^+\text{H}_{3-n}(\text{CH}_3)_n$ ammonium cations (where n is the degree of substitution), which improved directional carrier management and redistributed a homogeneous environment at the heterointerface. Finally, the PTAA HTL enabled achieving a champion PCE of 25.45% [77].

SAMs are ordered organic molecules with one or several layers of molecular arrays formed by spontaneous adsorption to the bottom surface [78]. At present, carbazol-phosphonic acid (PACz)-based SAMs, including 2-(9H-carbazol-9-yl)ethylphosphonic acid (2PACz) [62, 79], 2-(3,6-dimethoxy-9H-carbazol-9-yl)ethylphosphonic acid (MeO-2PACz) [80, 81], and [4-(3,6-dimethyl-9H-carbazol-9-yl)butyl] phosphonic acid (Me-4PACz) [82, 83], are one class of the most-promising HTL materials for IPSCs. These materials have high hole selectivity, and are used in the fabrication of devices with high PCEs via simple processes. In addition, the presence of dipoles on the SAM surface is beneficial to the improvement of the performance of IPSCs [84].

Sargent *et al* showed that cluster formation during phosphonic acid adsorption could lead to incomplete SAM (2PACz) coverage. Therefore, they designed a coadsorption strategy to ensure the homogeneous distribution of phosphate molecules, which resulted in minimized interfacial recombination and improved interfacial electronic structures. The

corresponding IPSC exhibited a PCE of 25.3% (24.8% certified) [62]. Xu *et al* proposed a porous insulating contact design to suppress the recombination loss at the buried interface by inserting a ~ 100 nm Al_2O_3 layer with random nanoscale openings at the SAM/PVK interface; the resulting device with a champion PCE of 25.5% was obtained [83].

For the large-scale fabrication of IPSCs, the PVK precursor solution must have high wettability on the SAM surface. Wu *et al* designed an amphiphilic (2-(4-(bis(4-methoxyphenyl)amino)phenyl)-1-cyanovinyl)phosphonic acid (MPA-CPA) molecule that formed bilayer HTLs comprising a SAM and a superwetting overlayer on the ITO substrate, leading to high-quality PVK film with minimized defects at the buried interface. Moreover, the energy level of MPA-CPA is better matched with the PVK layer than the conventional SAMs. The corresponding IPSCs showed a high certified PCE of 25.4%, together with a PCE of 22%–23.4% for 10 cm^2 minimodules [60]. Chen *et al*, considered the surface wettability and feasibility of SAM coated on the TCO substrate and designed a polymerized PACz (poly-4PACz), which exhibited excellent hole extraction capability at the buried interface and good tolerance to layer thickness. Thus, it was ideal for scalable coating and achieved excellent PCEs of 24.4% and 20.7% for the blade-coated IPSCs and modules, respectively [85]. Therefore, the dense coverage of SAM on the substrate is crucial for achieving efficient large-area high-performance IPSCs. Based on the aforementioned research, strategies for achieving dense coverage of SAM on substrates include appropriate modification of SAM molecules to regulate their wettability on the substrate, and the formation of SAM polymers. In addition, adding co-adsorbed molecules that can form suitable interactions with the substrate in SAM may also be helpful in forming a dense coverage of SAM. Furthermore, the coverage characterization of SAM on a large scale is equally important. However, research in this filed is still relatively lacking, so more research is needed to enhance its commercialization potential.

Inorganic NiO_x HTLs are promising for fabricating IPSCs with enhanced stability and reduced material cost. However, the surface of NiO_x HTL has abundant defects (Ni^{3+} states), which needs to be well passivated during device fabrication [70, 86] to achieve very high efficiency. For instance, Yu *et al* first treated NiO_x with hydrogen peroxide to improve its conductivity and then applied Me-4PACz SAM coating, which yielded a certified PCE of 25.2% and high stability [87]. Li *et al* designed a novel (4-(3,11-dimethoxy-7H-dibenzo[c,g]carbazol-7-yl)butyl)phosphonic acid (MeO-4PADC) SAM to anchor on the NiO_x HTL and achieved high stability with a remarkable certified PCE of 25.6%; this value was the highest reported thus far for NiO_x -based IPSCs [61].

3.2.2. Management of the bulk properties of PVK films

The fabrication of high-quality PVK films, as a cornerstone of PSCs, encounters notable challenges, which demand the exploration of numerous strategies such as additive engineering, solvent engineering, composition engineering, and

interfacial engineering. 1,3-bis(diphenylphosphino)propane (DPPP), a diphosphine Lewis base, enhanced the durability of PSCs by binding undercoordinated lead atoms at interfaces and grain boundaries [88]. The black PVK phase was stabilized and improved solar cell performance was achieved at varying temperatures using the ordered dipolar structure of β -poly (1, 1-difluoroethylene) (β -pV2F) to control the crystallization and energy alignment of PVK films [89]. 4-guanidinobenzoic acid hydrochloride, a nonvolatile additive, was used to modulate PVK film growth via a hydrogen-bond-bridged intermediate phase, which resulted in large and coherent grain growth [90].

Distinct additives such as methylamine formate (MAFa), an ionic liquid (IL) additive, mitigated octahedra distortion, suppressing the phase transition of α -FAPbI₃ to δ -FAPbI₃ [91]. Poly(dimethylsiloxane-co-methylsiloxane acrylate) improved the solubility and passivated defects [92], and potassium hexafluoroprop-ane-1,3-disulfonimide inhibited PbI₂ crystallization, adjusted crystal orientation, and passivated defects [93]. Pemirolast potassium considerably ameliorated carrier dynamics and mitigated residual stress [94]. 1-(phenylsulfonyl)pyrrole prevented cation segregation in FA-Cs PVKs and counteracted compositional inhomogeneity, thereby enhancing the photovoltaic performance of PSCs [64].

Yang *et al* ingeniously embedded α -lipoic acid (LA) into the PVK/NiO_x interface and bulk PVKs, transforming LA into a dynamic poly(LA) network via covalent and noncovalent bonds and optimizing the interfacial contact, residual stress, and photovoltaic output of PVK films [95]. The integration of (4-(2,7-dibromo-9,9-dimethylacridin-10(9H)-yl)butyl)phosphonic acid (DMAcPA) is also promising. Notably, DMAcPA was extruded to the grain boundaries and film surface, promoting well-matched PVK/ITO contact and achieving comprehensive passivation [65].

Innovative approaches such as the synthesis of halogenated tertiary ammonium by Ning *et al*, the introduction of a new 2D PVK based on 3-pyridinylmethylammonium ((3-PyA)₂PbI₄) by Ge *et al*, and utilization of 2-aminoindan hydrochloride additive by Zang *et al*, have contributed to the PVK film growth and quality by modulating interfacial contact and crystal orientation as well as reducing photochemical degradation [70, 96, 97]. Similarly, the use of multiple additives such as 1-butyl-3-methylimidazolium tetrafluoroborate IL, alkylamine ligands oleylamine (OAm), and benzylhydrazine hydrochloride creates robust and high-performing IPSCs [98]. Robust, high-performing PSCs with inhibited phase segregation and high photovoltaic performance were obtained using deformable coumarin [99].

Li *et al* proposed *in situ* buried-interface passivation strategies using a cyanoacrylic-acid-based molecular additive (BT-T) and Chen *et al* used low-volatile dibutyl sulfoxide Lewis base additive to address issues such as passivation agent dissolution, defect density, and internal stress, thereby enhancing the stability and crystallinity of the PVKs [63, 100].

2-methoxyethanol (2-ME) solvents notably coordinate with ammonium halide species, thus enabling the formation of

uniform small colloids and triggering the homogeneous nucleation and swift crystallization of PVK films, even under ambient conditions [101]. Using a two-component solvent system that amalgamated tetrahydrofuran (THF) and 2-ME, crystalline MAPbI₃ thin films were fabricated at room temperature, further demonstrating that THF expedites solvent removal to allow the deposition of highly crystalline MAPbI₃ PVK films [102].

In summary, PSCs with excellent performance can be fabricated using various additives and advanced solvent systems.

3.2.3. Surface modification PSCs experience voltage losses primarily due to defect-induced nonradiative recombination at the interfaces between the PVK and carrier transport layers. High-quality, low-defect PVK films can be fabricated via surface modification, ultimately enhancing the PSC performance. Inorganic salts, organic amines and their corresponding salts, and other liquid or solid organic molecules are a few examples of such surface modifiers.

MA thiocyanate (MASCN) post-treatment eradicates long ligands from the film surface and forms a MAPbI₃ overlayer, resulting in a planar heterojunction. This considerably reduces nonradiative recombination and defect density, promoting effective charge transport [103]. Ion diffusion management using guanidinium chloride bonds with octylammonium iodide limits OA diffusion and fosters quasi-2D PVK growth, thereby ensuring optimal energy level alignment [104]. The multifunctional amino acid salt 3-amino-4-phenylbutyric acid hydrochloride (ApaCl) encourages I⁻ interaction through its -NH₂ group and Pb²⁺ interaction through its -COOH group, causing surface passivation [105]. Similarly, the introduction of a 3-(aminomethyl) piperidinium iodide (3AMP)-based 2D capping layer presents an enhanced interface, which reduces the PVK/ETL junction defects, extends electron diffusion length, and accelerates extraction rates [106].

The combination of D-J PVK (DJP)-forming ligands 3-aminomethylpyridine (3-AMPY) and 4-aminomethylpyridine (4-AMPY) with 2, 2, 2-trifluoroethanol solvent yields $n = 3$ and 4 dominated 2D capping layers. This process considerably reduces defect density and promotes efficient electron tunneling [107]. The molecular structure of Calix[4]pyrrole, leveraging electropositive N-H bonds, anchors the surface halide anions of PVK and enhances the stability of PVK films and PSCs [108]. PY-IT, a polymerized small molecular acceptor, incorporated into the PVK/ETL interface, decreases trap states and promotes n -type surface and transport-friendly PVK orientation [109]. Similarly, a valinomycin-based macrocyclic molecule is introduced for removing defects and aligning the energy levels between the PVK and ETL [110]. 2-thiopheneethylammonium chloride treatments improve the energy level alignment with suitable offsets, fostering charge extraction. DFT calculations revealed a strengthened interplay between PVK and C₆₀ ETL [111]. Moreover, 3-mercaptopropyl(dimethoxy)methylsilane (MDMS) modification ensures surface trap passivation, ion migration, and moisture protection [112]. The utilization of

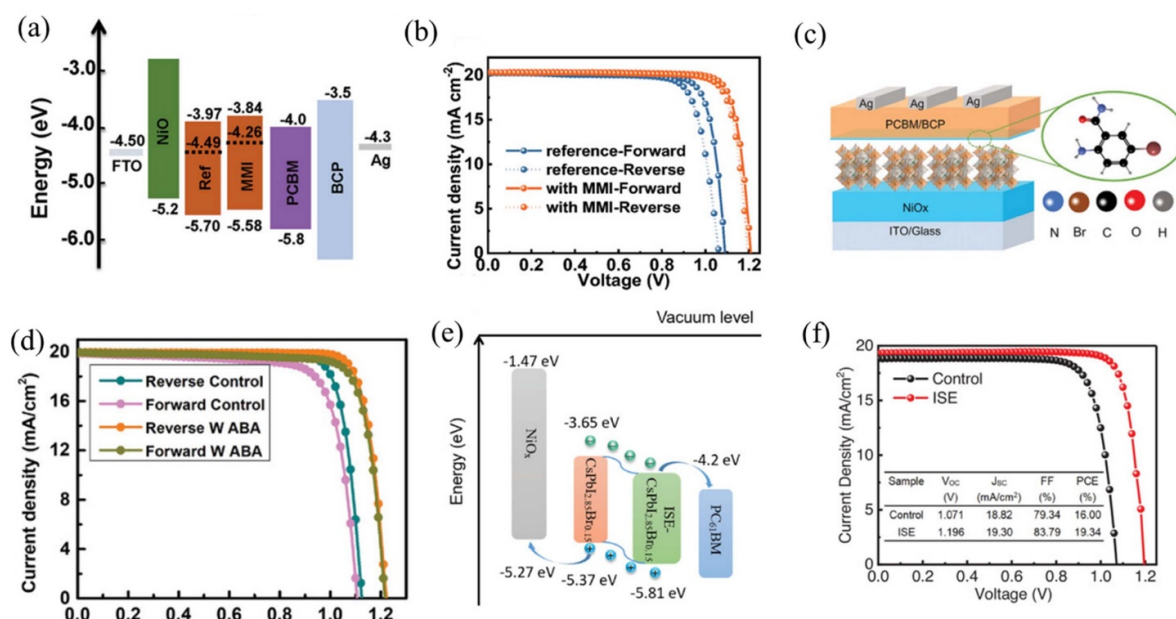


Figure 8. (a) Energy diagram of PSCs (with MMI treatment) and (b) J - V performance of PSCs with and without MMI treatment and hysteresis. [128] John Wiley & Sons. © 2023 Wiley-VCH GmbH. (c) Schematic illustration of the inverted IPSCs (with ABA treated) and (d) J - V curves of the champion control and ABA treated p-i-n IPSCs under one-sun illumination. [129] John Wiley & Sons. © 2023 Wiley-VCH GmbH. (e) Energy level structure diagram of IPSC and (f) J - V curves of control device and ISE-device. [126] John Wiley & Sons. © 2023 Wiley-VCH GmbH.

3,5-bis(trifluoromethyl) phenethylammonium iodide (2CF₃-PEAI) as an interface passivator optimized the energy levels, passivated defects, and protected the PVK films against moisture [63].

3-(aminomethyl)pyridine selectively interacts with surface formamidinium ions, which reduces the surface roughness and potential fluctuations and ensures effective n -type doping [113]. Solvent-free transfer-imprinting-assisted growth (TIAG) strategy fosters an enhanced 2D/3D PVK heterojunction, thereby improving the film quality, reducing trap density, and suppressing ion migration after introducing a uniform 2D PVK interlayer [114]. Furthermore, a rapid vapor method introduces a hydrophobic capping layer, with a thermodynamically stable alternating-cation-interlayer structure on 3D PVKs, reducing device defects and increasing efficiency [115].

3.2.4. Other strategies. The performance of IPSCs can also be improved by modifying the ETLs [116–118] or the ETL/PVK interface [119–122]. Qin *et al* found that the ferroelasticity of PVKs is accountable for suppressing the nonradiative recombination in IPSCs because of ferroelastic lattice deformation under electric activation [123]. Direct and alternating current (DC and AC) poling was applied to tune the lattice structure of PVKs and a PCE of 23.12% was obtained for MAPbI₃-based IPSCs; this value is one of the highest PCEs reported for MAPbI₃ [124]. These studies suggest the microscopic crystallographic structure modulation could be promising way to enhance the performance of PSCs.

3.3. Inorganic 3D PSCs

IPSCs constitute a major subset of inorganic PSCs. These devices, when compared to their upright counterparts, exhibit enhanced stability due to the use of undoped HTLs that are stabler than the doped spiro-OMeTAD typically used in upright structures. Moreover, the ETL in IPSCs usually comprises [6,6]-Phenyl-C61-butyric acid methyl ester (PCBM), which can be prepared at low temperatures, unlike TiO₂ used in upright structures that necessitates annealing at 500 °C. Currently, the PCEs of inorganic IPSCs such as CsPbI₃ (20.17%), CsPbI_{2.85}Br_{0.15} (19.34%), and CsSnI₃ (10.90%) have considerably improved [125–127]. However, compared to upright PSCs, IPSCs require further development.

3.3.1. Charge-transporting layer. PCBM is indeed a prevalent electron transport material. However, its high energy level mismatch and nonradiative charge recombination are notable factors contributing to the performance gap between IPSCs and regular PSCs (figure 8(a)). Consequently, the manipulation of the PVK/ETL interface properties emerges as a crucial strategy for developing high-performance IPSCs [128]. The commonly used hole transport materials for inorganic IPSCs are PTAA and NiO_x.

3.3.2. Surface modification. Interface modification is indeed crucial for enhancing the device efficiency, particularly inorganic PVK. The incorporation of physical moisture-proof layers, passivation agent polishing, and using organic

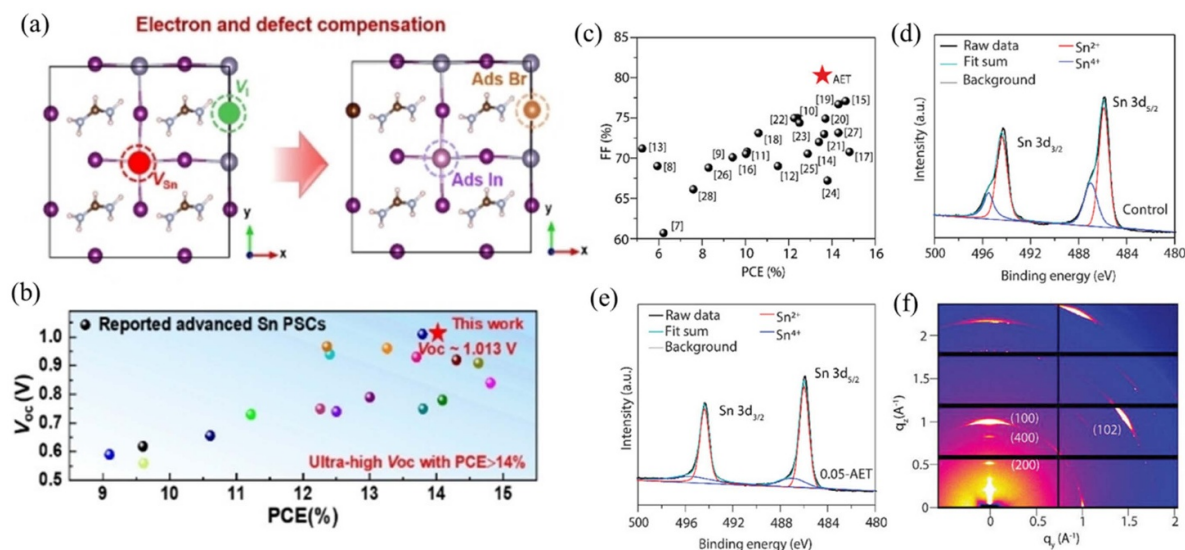


Figure 9. (a) DFT calculations of optimized slab models for pristine Sn PVK with V_{Sn} and V_I defects and In- and Br-co-doped Sn PVK (V_{Sn} and V_I are the Sn and I vacancies, respectively). (b) Summarized PCEs and V_{oc} values for the reported advanced TPSCs. (a), (b) [138] John Wiley & Sons. © 2023 Wiley-VCH GmbH. (c) Comparison of the FFs of 0.05-AET TPSC with previously reported TPSCs, revealing the highest FF achieved. High-resolution XPS spectra showing the Sn 3d regions of (d) control and (e) 0.05-AET Sn-based PVKs. (f) GIWAXS patterns of 0.05-AET Sn-based PVK films. (c)–(f) [136] John Wiley & Sons. © 2023 Wiley-VCH GmbH.

small molecule passivation agents (figures 8(b)–(f)) [126, 128–131] can facilitate charge transfer between PVK and the ETL, thereby improving the efficiency and stability of the device. This highlights the importance of continued research and development in this area to further optimize these processes and potentially discover new methods for interface modification.

3.3.3. Other methods. Considerable advancements have been made in the realm of high-performance n–i–p structure devices [31, 32]. To surpass the single-junction S–Q limit, multicell series batteries must be developed. In this context, efficient p–i–n structure batteries that can deliver high voltage output are vital [132] because IPSCs can be processed at low temperatures, making them more suitable for large-scale manufacturing. Furthermore, compared with traditional PSCs that typically employ hygroscopic dopants, these devices exhibit superior stability. This underscores the potential of IPSCs for use in efficient and stable solar energy solutions.

3.4. Sn-based PSCs

Studies on TPSCs in 2023 have predominantly revolved around p–i–n devices for optimizing PVK composition [86, 133–139]. These optimizations have considerably enhanced the two critical parameters of Sn PVKs, V_{oc} and FF.

Liu *et al* introduced an electron and defect collaborative compensation strategy (EDC) to minimize V_{oc} losses [138]. By incorporating a small quantity of the heterovalent metal halide, indium bromide ($InBr_3$), into the Sn PVK lattice, the electronic structure and defect distribution of PVK can be simultaneously adjusted (figure 9(a)). This strategic addition

increased the Fermi level of Sn PVKs by ~ 0.12 eV and considerably reduced the interfacial charge transfer barrier. Thus, the recombination losses within the bulk phase and at the interface of the PVK material were effectively reduced. The device fabricated using this innovative EDC strategy achieved an excellent V_{oc} of 1.013 V and a champion efficiency of 14.02% (figure 9(b)). This breakthrough also narrowed the voltage loss gap compared to lead-based PVKs (~ 0.30 V).

Li *et al* fabricated a Sn-based device with a FF as high as 80% by incorporating an organic small molecule, 2-(2-aminoethyl)-2-thiopseudourea dihydrobromide (AET), into the Sn PVK structure [136]. This is the highest reported FF for narrow-bandgap (NBG) TPSCs (figure 9(c)). They not only confirmed the strong interaction between AET and Sn PVKs but also discovered that AET effectively suppressed the problematic oxidation of Sn PVK and considerably retarded its crystallization rate (figures 9(d) and (e)). Thus, Sn PVKs with superior crystallinity and morphology were formed (figure 9(f)). Moreover, the encapsulated device exhibited commendable long-term stability, retaining 80% of its initial performance even after being stored for 700 h.

Improved electron transport materials, such as diethyl malonate 60 double adduct (DCBA) [140] and single-isomer C_{60} - and C_{70} -based diethylmalonate functionalized bisadducts ($C_{60}BB$ and $C_{70}BB$) [141], are being developed to optimize the ETL. Sun meticulously separated four regional isomers of DCBA, namely trans-2, trans-3, trans-4, and e [140]. A comprehensive characterization revealed that the molecular structure of regioisomers directly impact the energy levels, molecular packing, interface contact, and even photovoltaic performance. Ultimately, the device based on trans-3 achieved a certified efficiency of 14.30% (figure 10(a)). Similarly, Yang *et al* designed and synthesized single-isomer C_{60} - and C_{70} -based

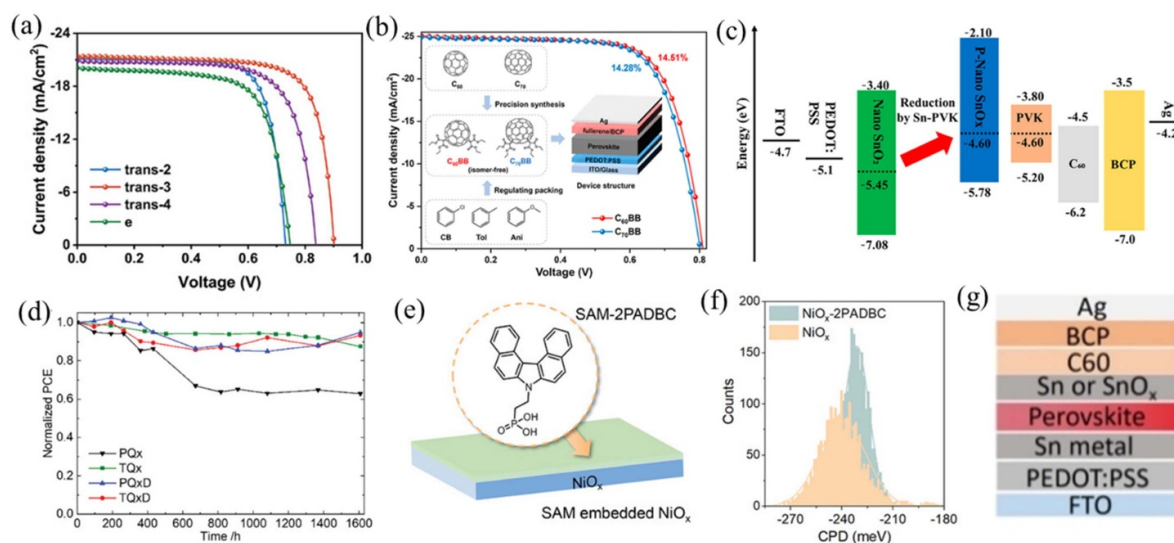


Figure 10. (a) Characteristic $J-V$ curves of TPSCs incorporated with different ETLs (four regional isomers of DCBA, namely trans-2, trans-3, trans-4, and e). [140] John Wiley & Sons. © 2023 Wiley-VCH GmbH. (b) Characteristic $J-V$ curves of TPSCs incorporated with C60BB and C70BB. Reprinted with permission from [141]. Copyright (2023) American Chemical Society. (c) Energy diagram of Sn PSCs incorporated with SnO_x HTL. Reprinted with permission from [142]. Copyright (2023) American Chemical Society. (d) $J-V$ curves of the devices made of PQx, TQx, PQxD, and TQxD. [143] John Wiley & Sons. © 2023 Wiley-VCH GmbH. (e) SAM-embedded NiO_x for oxidation suppression. (f) Contact potential difference for NiO_x and 2PADBC-embedded NiO_x films. (e), (f) [144] John Wiley & Sons. © 2023 Wiley-VCH GmbH. (g) Structure of Sn-based PSCs inserted with Sn metal on both the upper and lower surfaces of the PVK layer. [145] John Wiley & Sons. © 2023 Wiley-VCH GmbH.

diethylmalonate functionalized bisadducts (C60BB and C70BB) [141]. The devices based on C60BB and C70BB achieved high efficiencies of 14.51% and 14.28%, respectively (figure 10(b)).

To optimize the HTL, new inorganic small molecules and polymers have been developed as alternative materials to poly (3,4-ethylenedioxythiophene) polystyrene sulphonic acid (PEDOT:PSS) because its acidity can potentially damage Sn PVKs [142, 143, 146–148]. For instance, Kitamura *et al* discovered that nano-SnO₂ transforms into SnO_x ($x < 2$) nanoparticles (P-Nano SnO_x) upon contact with Sn PVKs [142]. Using P-Nano SnO_x as an HTL, solar devices achieved a PCE of 9.77% with improved stability (figure 10(c)). Moreover, Wei *et al* developed a range of new triphenylamine (TPA) functionalized isomeric polythiophenes [147] and X-type quinoxaline-based organic dye SAMs [143] as hole transport materials for inverted TPSCs. Among these materials, the device based on TQxD (4) achieved PCE of 8.3%, which is the highest reported result for SAM-based TPSCs to date (figure 10(d)). Furthermore, devices based on this type of p-type SAM exhibited excellent long-term stability.

Various intermediate layers, such as [2-(3,6-dimethoxy-9Hcarbazol-9-yl)ethyl]phosphonic acid (MeO-2PACz) SAM [149], 4AMPY(Ac)₂ ((aminomethyl)pyridinium acetate) [150], and (4-(7H-dibenzo[c,g]carbazol-7-yl)ethyl)phosphonic acid (2PADBC) [144], have been incorporated between the Sn PVK and the HTL. Li *et al* identified the hole transport barrier at the PVK–NiO_x interface and developed a self-assembled single-layer interface, which

reduced the voltage loss and increased the PCE of small-area devices to 14.19% and large-area (1 cm²) devices to 12.05% (figures 10(e) and (f)) [144]. Furthermore, the introduction of 2PADBC enabled the device to maintain over 93% of its initial performance after 1000 h. Dual-interface optimization is another strategy currently under exploration. Wang *et al* discovered the presence of Sn⁴⁺ concentration on both the upper and lower surfaces of the PVK layer and inserted a Sn metal layer at these interfaces, thereby effectively reducing the Sn⁴⁺ density and defects (figure 10(g)) [145]. This optimization technique yielded a high PCE of 14.3%.

All-organic TPSCs were also studied recently besides organic–inorganic TPSCs. Yan *et al* found that the lone electrons on the –NH₂ and –CO units of carbazide (CBZ) interacted with Sn²⁺, decelerating the film crystallization and resulting in a pinhole-free film with enlarged grains after annealing at 80 °C (figure 11(a)). The ratio of Sn⁴⁺ to Sn²⁺, $n(\text{Sn}^{4+})/n(\text{Sn}^{2+})$, also decreased from 0.85 to 0.43. Finally, compared with the reference device (PCE = 4.12%), the PCE of the CsSnI₃–CBZ device reached 11.21%, which is the highest PCE reported for CsSnI₃ PSCs thus far (figure 11(a)) [125].

Notably, most PVK precursor solutions currently studied are obtained by directly mixing CsI with an equimolar amount or an excess of commercial SnI₂ into an organic solvent. However, due to unavoidable oxygen exposure during their synthesis, SnI₂ [even with the highest purity (99.9999%)] may contain a substantial amount of Sn⁴⁺. This affects the quality of Sn-based PVKs precursor solution [152]. Wang *et al* first synthesized high-quality CsSnI₃ single crystals using a

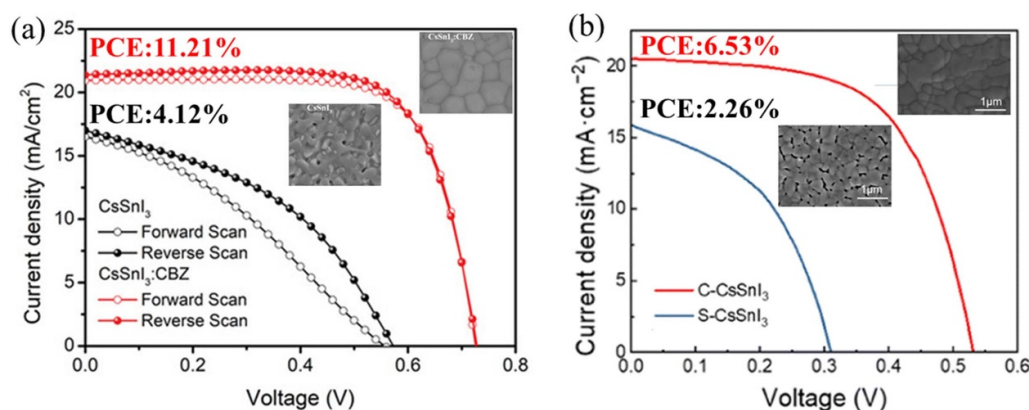


Figure 11. (a) J - V characteristic curves of the CsSnI_3 solar cells based on without CBZ and with CBZ. Insets: SEM Images the pristine CsSnI_3 and $\text{CsSnI}_3\text{:CBZ}$ films. [125] John Wiley & Sons. © 2023 Wiley-VCH GmbH. (b) Photocurrent density-voltage curves of the optimized C- CsSnI_3 and S- CsSnI_3 PSCs. Insets: SEM images of S- CsSnI_3 and C- CsSnI_3 films. Reproduced from [151] with permission from the Royal Society of Chemistry.

wet chemical method for Sn source purification; they then dissolved it to obtain an additive-free precursor solution (crystal-derived CsSnI_3 , C- CsSnI_3). The average colloidal particle size of the precursor solution (salt-derived CsSnI_3 , S- CsSnI_3) that directly dissolved CsI and SnI_2 was 20 nm, whereas the average colloidal particle size of C- CsSnI_3 was 60 nm. This indicated rapid nucleation occurred in the C- CsSnI_3 precursor solution, resulting in a denser morphology of the film surface (figure 11(b)). Correspondingly, compared to the PCE of S- CsSnI_3 (2.26%), C- CsSnI_3 device exhibited a higher PCE (6.53%; figure 11(b)) [151].

Thus, the manipulation and optimization of Sn PVKs will remain a central focus in future research endeavors. Concurrently, the design and development of electron transport materials, hole transport materials, and interlayer materials are equally effective strategies for minimizing losses and enhancing the overall device performance.

3.5. 2D PSCs

Two-dimensional (2D) PVKs was extensively studied in 2023 owing to their superior environmental and structural stability. The insertion of bulky organic spacer cations [e.g. aliphatic *n*-butylammonium (BA) and aromatic phenylethylammonium (PEA)] could protect the inorganic PVK from corrosion by external stimuli (e.g., heat, moisture, and illumination) and ensure long-term device stability. These organic spacers can also suppress ion migration in 2D PVKs, considerably enhancing their thermal and photostabilities compared to 3D PVKs [153, 154]. Despite the superior environmental stabilities of 2D PVKs, the 2D PSCs still exhibited inferior PCE compared to 3D devices because [153] (1) bulky organic spacers produced strong quantum and dielectric confinement effects, inducing a large exciton binding energy and inhibiting the charge carrier transport and (2) 2D PVKs have anisotropic crystallization features, and the bulky insulating organic spacer hinders vertical charge transport between the inorganic PVK sheets.

Thus, the design of novel organic spacer cations with large dielectric constant and crystallization kinetics regulation on the crystal plane orientation are two effective strategies for enhancing the performance of 2D PSCs [155, 156]. The construction of 2D/3D heterostructures is also an effective strategy to enhance the performance of PSCs; this approach combines the high stability of 2D PVKs and high performance of 3D PVKs [157]. Moreover, Pb-Sn-based PSCs have demonstrated superior advantages in applications of single and tandem photovoltaics; however, but they suffer from low device stabilities. The layered structure of 2D PVKs is expected to mitigate degradation issues associated with environmental factors and enhance bandgap tunability [158, 159].

Herein, we summarize the progress in four aspects: design of novel organic spacer cations, regulation of crystallization kinetics, exploration of 2D Pb-Sn PVKs, and niche research directions of 2D PVKs. Given the limited research on regular 2D PSCs, a few studies on regular 2D PSCs are summarized here. We expect that this section of the paper will help shed light on further advancements in 2D PVK photovoltaics in terms of efficiency and stability.

3.5.1. Design of novel organic spacer cations. Fortunately, the diversity of organic spacer cations provides an ideal platform for investigating and optimizing the carrier properties of efficient 2D PSCs. The large organic spacer cations may hinder the transport of photo-generated carriers, increase exciton binding energy (E_b), and ultimately lead to poor photovoltaic performance of the PSCs. Therefore, the design criteria for efficient organic spacer cations is to reduce E_b while improving the transport of photo-generated carriers. Exploring new organic spacer cations to reduce the E_b while simultaneously constructing a ‘charged bridge’ for carriers to cross the energy gap inside 2D PVKs is an innovative solution for ensuring high PCE and long lifetime of 2D PSCs. Li *et al* synthesized a new family of low-dimensional Ruddlesden-Popper (RP) PVKs, $(\text{GABA})_2\text{MA}_{n-1}\text{Pb}_n\text{I}_{3n+1}$ ($n = 1, 2, 3$, and 4; $\text{MA}^+ = \text{CH}_3\text{NH}_3^+$), with suppressed

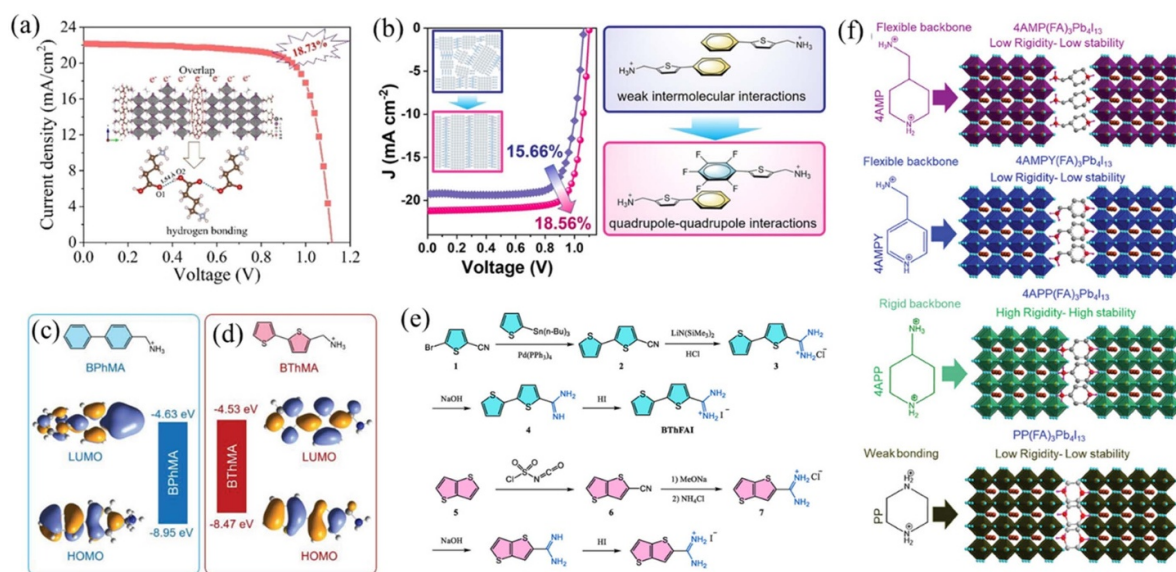


Figure 12. (a) Strong hydrogen bonding (O—H...O) linking adjacent spacing sheets in (GABA)₂MA₃Pb₄I₁₃ crystal, which enhanced the PCE of the corresponding 2D RP PSCs. [160] John Wiley & Sons. © 2023 Wiley-VCH GmbH. (b) Devices based on two unique semiconductor spacers with strong interactions, with PCEs increasing considerably from 15.66% to 18.56%. [162] John Wiley & Sons. © 2023 Wiley-VCH GmbH. (c) Chemical structure and DFT-calculated energy levels of the BPhMA spacer. Reproduced with permission. (d) Chemical structure and DFT-calculated energy levels of the BThMA spacer. (c), (d) [163] John Wiley & Sons. © 2023 Wiley-VCH GmbH. (e) Synthetic routes of two organic spacer cations, BTFAI and TTFAI. [164] John Wiley & Sons. © 2023 Wiley-VCH GmbH. (f) Schematic of (A(FA)₃Pb₄I₁₃)-based DJ 2D PVKs and chemical structure of all-organic spacers studied herein. [165] John Wiley & Sons. © 2023 Wiley-VCH GmbH.

dielectric confinement using γ -aminobutyric acid (GABA) as the organic spacer cation [160]. As shown in figure 12(a), the hydrogen bonds between the spacers link the adjacent PVK slabs, enabling charge localization in the van der Waals gap. Thus, a charged bridge for efficient charge carrier transfer through the spacer area is successfully generated. The PCE of (GABA)₂MA₄Pb₅I₁₆ 2D RP PSCs with superior charge-carrier transport properties was up to 18.73%. Zhang *et al* synthesized a new spacer cation of β -fluorophenylethanamine (β -FPEA) for fabricating high-performance FA-based 2D RP PSCs [161]. The addition of fluoro functional group increased the dipole moment of the spacer cation, causing stronger interactions between the cations and [PbI₆]⁴⁻ octahedra, and thus, more efficient charge carrier dissociation. The resultant quasi-2D RP PSCs had PCEs of 19.11%.

Owing to the anisotropic feature of the crystal structure, the charge-carrier transport properties of 2D PVKs are considerably affected by the crystal growth and orientation. Chen *et al* [162] synthesized two semiconducting organic spacers, phenylthiophenmethanamine iodide (PTMAI) and perfluorophenylthiophenmethanamine iodide (5FPTMAI), to synthesize the ((5FPTMA)_{0.1}(PTMA)_{0.9})₂MA_{*n*-1}Pb_{*n*}I_{3*n*+1} (nominal *n* = 5, 5F/PTMA–Pb) PVK films. The introduction of fluoro group resulted in a preferred vertically oriented film with reduced grain boundaries and increased lattice strain. Finally, owing to the decreased exciton binding energy and increased charge carrier transport, the 5F/PTMA–Pb device exhibited a PCE of 18.56% with enhanced thermal and illumination stability (figure 12(b)).

Dong *et al* proposed the quantum confinement breaking in 2D PVKs using organic semiconductor spacers with suitable energy levels (figures 12(c) and (d)) [163]. The strong orbital coupling between [PbI₆]⁴⁻ octahedral slabs and a bithiophene-based long conjugated spacer (BThMA) resulted in the breaking of multiple QW structures. Owing to the improved film quality, enhanced dielectric constant, and decreased exciton binding energy, BThMA-based 2DRP PSCs demonstrated a decent PCE of 18.05%; this value was higher than that of the BPhMA-based device (PCE = 12.96%). Wang *et al* successfully synthesized two FA-based spacers, TTFA (containing fused-bithiophene) and BTFA (containing unfused-bithiophene), for 2D RP PSCs (figure 12(e)) [164]. The TTFA spacer reduced the energy barrier of nucleation and facilitated PVK crystallization, resulting in improved film quality and preferred crystal vertical orientation. The resultant devices based on (TTFA)₂MA_{*n*-1}Pb_{*n*}I_{3*n*+1} (*n* = 5) achieved a record efficiency of 19.41% for 2D RP PSCs that used FA-based spacers.

Pure-phase 2D PVKs with uniform QW widths and fixed low-*n* values are highly desirable for high efficiency and stability. However, their uncontrollable crystallization continues to be a challenge, resulting in random well-width distribution of multiple QWs with disordered orientation. Ahmad *et al* fabricated 4APP(FA)₃Pb₄I₁₃-based 2D DJ PSCs using 4APP (4-aminopiperidinium) as the organic spacer (figure 12(f)) [165]. The rigid backbone and strong hydrogen bonding of 4APP, combined with tri-solvent engineering strategy, induced the formation of high-quality pure-phase 2D DJ PVK films with

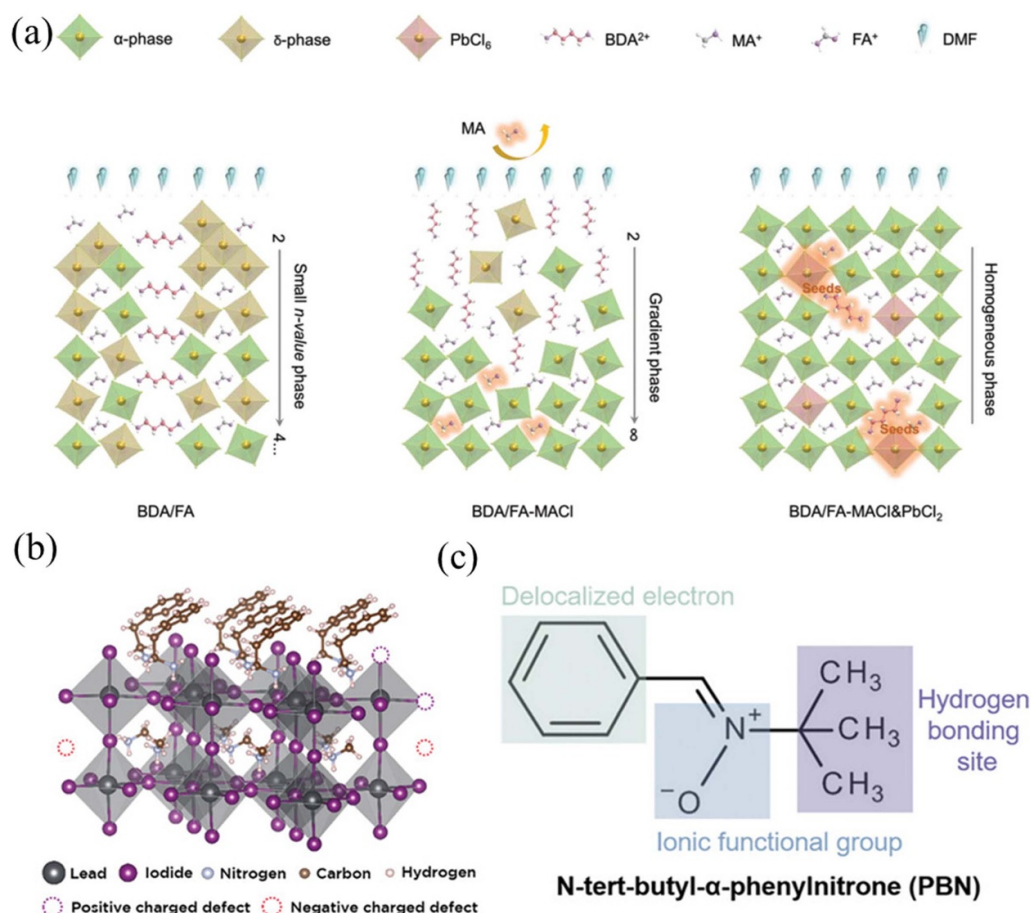


Figure 13. (a) Hypothesized crystallization mechanism of BDA/FA, BDA/FA-MACl, and BDA/FA-MACl & PbCl_2 films. BDA/FA film comprises a δ phase and low-dimensional phase, while BDA/FA-MACl film gradually exhibits the appearance of both δ and low-dimensional phases as chlorine evaporates. BDA/FA-MACl & PbCl_2 film, grown epitaxially under the induction of preformed seeds, yields a highly robust α phase 2D PVK. [166] John Wiley & Sons. © 2023 Wiley-VCH GmbH. (b) Schematic of an $n = 5$ RP PVK $(\text{PEA})_2\text{MA}_4\text{Pb}_5\text{I}_{16}$ film and corresponding charged defect sites in PVKs. (c) PBN molecular structure and possible function of each functional group, including the benzene group (green), nitron group (blue), and t-butyl group (purple). (b), (c) [167] John Wiley & Sons. © 2023 Wiley-VCH GmbH.

uniform QW width and superior crystallization orientation. The PCE of the resultant FA-based 2D DJ PSCs increased by 48% compared to other control devices.

3.5.2. Regulation of crystallization kinetics. Crystallization kinetics regulation is crucial for the fabrication of 2D PVK films for solar cells. Uniform and well-ordered crystalline structures are obtained by appropriately controlling crystallization, which directly impact the optoelectronic properties of the as-fabricated films. This regulation influences factors such as grain size, orientation, and defect density, which collectively determine the overall performance and stability of PSCs. Optimizing crystallization kinetics enhances charge carrier mobility, reduces recombination losses, and improves the overall efficiency and durability of 2D PSCs.

Two-dimensional (2D) DJ PSCs have lower PCE compared to 2D RP PSCs, largely because of uncontrollable phase distribution and limited charge-carrier transport efficiency of 2D DJ PVKs. Wu *et al* used an organic ligand containing 1,4-butanediammonia diiodide (BDAl_2) to construct 2D DJ PVKs

and added MACl and PbCl_2 to modulate the nucleation and crystallization of PVKs (figure 13(a)) [166]. Seeds comprising MAPbCl_3 and BDAPbI_4 can facilitate the epitaxial growth of high-quality FA-based 2D DJ PVK films. The resultant film successfully suppressed the δ phase and efficiently mitigated random phases ($n = 2, 3, 4, \dots$), minimizing energy loss, achieving a high PCE of 20.0%, and maintaining 98% of its initial efficiency after 1344 h of storage. Furthermore, Kim *et al* introduced zwitterionic n-tert-butyl- α -phenylnitrone (PBN) as the top passivator of 2D RP PVK $(\text{PEA})_2\text{MA}_4\text{Pb}_5\text{I}_{16}$, $n = 5$ to induce vertically oriented crystallization and improve the charge carrier transport (figures 13(b) and (c)) [167]. After this surface treatment, 2DRP PSCs exhibited superior operational stability and their PCE improved from 17.53% to 20.05%.

3.5.3. Exploration of 2D Pb–Sn mixed PVKs. Pb–Sn PVKs have a higher potential for single-junction and TSCs because of their tunable NBG and reduced toxicity. However, easy oxidation of Sn^{2+} may result in inferior device stability.

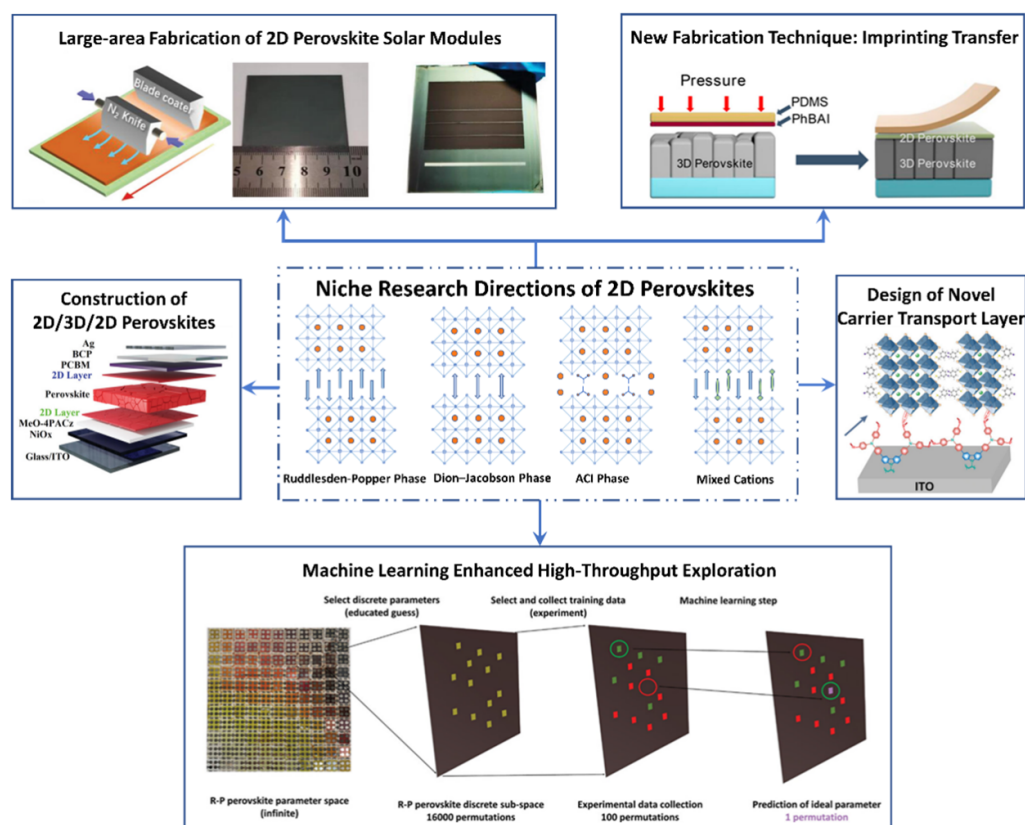


Figure 14. Niche research directions of 2D PVKs. (1) Large-area fabrication of 2D PSMs: schematic of the PVK coating process, optical image of the large-area $\text{FA}_{0.4}\text{MA}_{0.6-x}\text{GA}_x\text{PbI}_3$ PVK film prepared on the $\text{SnO}_2/\text{CATNI}$ sample, and front view optical images of the planar n-i-p PSMs. [170] John Wiley & Sons. © 2023 Wiley-VCH GmbH. (2) New fabrication technique of imprinting transfer: schematic of the solvent-free transfer-imprinting-assisted growth process. Reprinted with permission from [114]. Copyright (2023) American Chemical Society. (3) Construction of 2D/3D/2D PVKs: schematic of the device structure. [171] John Wiley & Sons. © 2023 Wiley-VCH GmbH. (4) Design of a novel carrier transport layer: the proposed passivation mechanism of PVKs influenced by different polymers. [68] John Wiley & Sons. © 2023 Wiley-VCH GmbH. (5) Machine learning-enhanced high-throughput exploration: summary of the design of experimental approach for 2D PVKs. [172] John Wiley & Sons. © 2023 The Authors. Advanced Energy Materials published by Wiley-VCH GmbH.

Owing to the presence of large organic spacer cations, 2D PVKs have superior moisture resistance and high structural stability, which can be applied to Pb–Sn PVKs for enhancing device stability. Chen *et al* proposed a two-step blade coating process to fabricate quasi-2D RP Pb–Sn IPSCs based on $\text{PEA}_2(\text{FA}_{0.5}\text{MA}_{0.5})_4(\text{Pb}_{0.5}\text{Sn}_{0.5})_5\text{I}_{16}$ [168]. Furthermore, SnSe was *in situ* prepared on the top of blade-coated PVKs, reacting Sn(II) acetate (SnAc_2) with and N,N-dimethylselenourea (DMS). This hydrophobic SnSe-protective layer can reduce nonradiative recombination and suppress ion migration. Consequently, this quasi-2D RP Pb–Sn IPSCs based on SnSe passivation exhibited an improved PCE of 15.06%. The optimized device also showed superior environmental and operational stability. To further enhance the performance of 2D Pb–Sn PSCs, Qin *et al* explored the preferred crystal orientation by tuning the Pb/Sn ratio. A superior PCE of 18.06% was achieved based on 2D RP Pb–Sn PVKs ($\text{iso-BA}_2\text{MA}_4(\text{Pb}_x\text{Sn}_{1-x})_5\text{I}_{16}$) ($n = 5$ and $x = 0.7$) [169]. Introducing a multifunctional 2D PVK layer with an antioxidant capability is ideal for enhancing the performance of Pb–Sn PSCs by relying on the dopamine cation (DAH^+) organic spacer with reductive capability.

3.5.4. Niche research directions of 2D PVKs. We rationalize several encouraging niche research directions of 2D PVKs based on publications in 2023 (figure 14).

- (1) Exploring large-area fabrication techniques for 2D PSMs is promising for scalable and cost-effective deployment. Large-area PSCs and PSMs have considerably lower PCEs than small lab-scale cells. To commercialize fabrication techniques of PSCs, large-scale fabrication processes for high-performance PSCs and PSMs must be explored. More importantly, the combination of 2D PVK and large-scale fabrication technique is quite appealing to achieve stable and reliable PSCs and PSMs with high efficiencies. Wang *et al* developed an interfacial engineering strategy for fully printing quasi-2D $\text{GA}(\text{MA})_n\text{Pb}_n\text{I}_{3n+1}$ PSCs ($n = 4$) with SnO_2 as the ETL [170]. A thin naphthaleneimide derivative (CATNI) was inserted between SnO_2 and the PVK layer for defect passivation and energy loss suppression. Consequently, the CATNI-based 2D PSC and PSM (25 cm^2) with enhanced stability demonstrated the optimized PCEs of 18.9% and 14.6%, respectively.

- (2) The innovative imprinting transfer technique opens avenues for the efficient and precise fabrication of 2D PVK films, thereby enhancing the quality of manufacturing processes. Jiang *et al* developed a solvent-free TIAG method to fabricate 2D/3D PVK heterojunctions [114]. The TIAG process induced a spatially confined growth of the 2D PVK interlayer with uniform morphology on the surface of 3D PVK. Furthermore, the pressure generated by the TIAG process improved the crystalline orientation, leading to enhanced charge-carrier transport. Consequently, the IPSC demonstrated a PCE of 23.09% (with certified 22.93%) with great thermal and light stability. The flexible IPSCs exhibited a PCE of 21.14%.
- (3) The construction of 2D/3D/2D heterostructures is another effective strategy to further enhance the performance of PSCs compared to 2D/3D heterostructures. These sandwiched 2D/3D/2D heterostructures combined the high stability of 2D PVKs and high performance of 3D PVKs. More importantly, these 2D/3D structures achieved a higher PCE than their 3D counterparts owing to the passivation ability of 2D PVKs to reduce the nonradiative recombination and improve the energy bandgap alignment to enhance the built-in electric field. Zhang *et al* fabricated the 2D/3D/2D PVK heterostructure film with optimized top/buried interface [171]. Typically, phenethylammonium bromide (PEABr) was deposited on top, while 2D $\text{PEA}_2\text{FA}_2\text{Pb}_3\text{Br}_{10}$ PVK was at the bottom of 3D $\text{Cs}_{0.07}\text{FA}_{0.85}\text{MA}_{0.08}\text{Pb}(\text{I}_{0.95}\text{Br}_{0.05})_3$ PVK. As a result, an improved PCE of 24.2% was achieved for the IPSCs based on 2D/3D/2D PVK owing to the minimal nonradiative recombination.
- (4) The design of a novel carrier transport layer is the key focus for enhancing the charge mobility and reducing recombination losses in 2D PSCs. For instance, polymer hole-transporting materials (HTMs) with functional passivation groups are expected to improve the buried interface and crystallization of PVKs. Pan *et al* synthesized two side-chain functionalized polymer HTMs of PVCz-SMeTPA and PVCz-SMeDAD [68]. The methylthio groups in the side-chain of the as-prepared polymers can passivate the buried interface defects and improve the crystallinity. Furthermore, owing to the π -acceptor capability of the sulfur atom, PVCz-SMeTPA and PVCz-SMeDAD achieved well bandgap alignment with quasi-2D PVK, facilitating the charge transfer at the PVK buried interface. As a consequence, the inverted quasi-2D PSCs using PVCz-SMeTPA and PVCz-SMeDAD as HTM exhibited the champion PCEs of 21.41% and 20.63%, respectively.
- (5) Leveraging machine learning for high-throughput exploration enhances the efficiency of material discovery and optimization of 2D PSCs. Specifically, optimizing the quality of PVK films involves a number of factors, such as precursor concentration, substrate temperature and roughness, surface wetting properties, solvent volatility and viscosity, and ambient conditions (pressure, humidity, temperature, and atmosphere). Exploring these factors

is highly laborious and manual experiments are usually uncontrollable. Meftahi *et al* developed a methodology for efficiently exploring the vast compositional space of 2D RP PSCs [172]. They employed a combination of machine learning and a high-throughput robotic fabrication process for further optimizing the PCE and stability of PSCs. The drop-cast 2D RP PSCs based on machine learning optimization achieved a PCE of 16.9%.

For large-area PSC fabrication, maintaining a uniform film thickness continues to be a challenge. Therefore, the PVK film deposition must be optimized and crystallization uniformity must be ensured to enhance the reliability of large-area 2D PVK modules. The sensitivity of imprinting to substrate variations is a concern and refining the process to accommodate diverse substrates and ensure consistent outcomes would strengthen its applicability. The potential interlayer of 2D/3D/2D PVKs affects the device stability; therefore, interfacial engineering and stability mechanisms must be further investigated to improve the device stability. Current carrier transport layer design may not fully optimize charge transport, and new materials and interface engineering techniques must be explored to enhance the carrier mobility and reduce losses. Finally, overreliance on limited datasets in machine learning-based techniques may not yield accurate predictions. Thus, datasets must be continuously expanded and diversified to refine machine learning models and improve their predictive capabilities in 2D PVK research.

3.6. Single-crystal based PSCs

PVK single crystals, as single-crystal silicon beyond polycrystalline silicon based solar cells, are expected to be used for improving efficiency and stability performance of PSCs due to fewer interfacial defects and long carrier lifetime, which are superior to PVK polycrystalline films [27, 173–176]. Monocrystalline PSCs have garnered considerable research attention. In the past year, PVK single crystals were used in PSCs by organic molecule and crystal interface inducing methods. Given the limited research on single-crystal PSCs, we also summarize a few regular single-crystal based PSCs research here.

3.6.1. Organic molecule inducing method. Bifunctional MDMS was used for surface trap passivation and reducing the moisture in thin MAPbI_3 single crystals obtained using the space-limited method. The sulfur atom in MDMS coordinated with Pb^{2+} on the MAPbI_3 interface to reduce surface defect density and nonradiative recombination. The PSCs exhibited a high efficiency of 22.2% and enhanced reverse-bias stability. Moreover, the cross-link of silane molecules enhanced the moisture stability of devices [112]. Almasabi *et al* reported a method to grow mixed-cation $\text{FA}_{0.6}\text{MA}_{0.4}\text{PbI}_3$ PVK single crystals on a hydrophilic SAM HTL ($\text{MeO}-2\text{PACz}$) surface. $\text{MeO}-2\text{PACz}$ improved the mechanical adhesion of the PVK on the substrate, enabling the fabrication of solar cells with

enhanced stability and a PCE of 23.1% [177]. Lintangpradipto *et al* fabricated $\text{Cs}_{0.05}\text{FA}_{0.95}\text{PbI}_3$ single-crystal PSCs with a 20 μm -thick single-crystal absorber layer. The devices achieved new stability (maintained 90% efficiency after 900 h at 53 °C) and high efficiency of 24.29% for single-crystal PSCs. Accelerated aging tests showed that they endured the damp heat test, and $\text{Cs}_{0.05}\text{FA}_{0.95}\text{PbI}_3$ single crystals approximately twice as long as polycrystalline films at 85 °C/65% RH [178]. Liu *et al* resolved the surface contamination issue by introducing an amphiphilic long-chain organic amine (cetyltrimethylammonium chloride, CTAC) into the PVK crystal growth solution. Inspired by the self-cleaning effect of lotus leaf, the self-assembly of CTAC provided a hydrophobic crystal surface, which induced spontaneous removal of residual solution. This process yielded a high-quality surface and higher efficiency of 23.4% for $\text{FA}_x\text{MA}_{1-x}\text{PbI}_3$ PSCs [179].

3.6.2. Crystal interface inducing method. Crystal interface inducing method was proposed to fabricate 2D/3D PSCs with high 2D crystal stability and efficiency of 3D PSCs [180]. Yang *et al* demonstrated *in situ* phase reconstruction of 2D/3D PVKs using a 2D PVK single-crystal-assisted method via the gradient phase distribution of 2D RP PVKs onto the 3D PVK surface, followed by thermal annealing. The obtained 2D/3D film exhibited reduced trap density, increased carrier mobility, and superior moisture resistance. The optimized 2D/3D devices achieved a champion PCE of 24.87% with a high V_{oc} of 1.185 V. The unencapsulated solar cells demonstrated considerably enhanced operational stability (>97% retention after continuous irradiation for 1500 h) [180].

3.7. Flexible PSCs (FPSCs)

Although the PCE of FPSCs still lags behind that of rigid PSCs, FPSCs can meet the requirements of industrial roll-to-roll preparation, giving them considerable commercialization potential. In addition, FPSCs can also expand their usage scenarios, including wearable and portable power devices. Therefore, FPSCs are also a highly significant field for future development. In 2023, the research of FPSCs mainly focuses on PVK film management and modification of buried interfaces. Given the limited research on FPSCs, we also summarize a few regular FPSCs research here.

3.7.1. PVK film management. Unlike rigid PSCs, FPSCs are subjected to external mechanical stress during devices preparation and operation. The grain boundaries of PVK films usually contain more defects and degradation sites. When PVK films are subjected to external mechanical stress, the grain boundaries often act as the sites for sudden changes in the film's morphology and structure. Therefore, it is crucial to reduce the adverse states in PVK grain boundaries, such as cracks, defects, and residual lattice strain, through appropriate PVK film management strategies for the preparation

of high-performance FPSCs. Jiang *et al* used a solvent-free TIAG method to *in situ* grow 2D/3D PVK heterojunctions. The pressure and heat related to the TIAG process promote close contact and chemical reactions between organic salts and PVKs, thereby obtaining high-quality PVK films. As a result, a PCE of 21.14% was achieved for FPSCs, and the PCE maintained 80% of their initial value after 10 000 bending cycles under a 3 mm bending radius [114]. Han *et al* designed a ferroelectric 2D PVK based on pyridine heterocyclic ring as the organic interlayer. This 2D crystal seed can form more uniform and highly oriented PVK crystals, which helps with the growth of 3D PVK crystals. Therefore, FPSC with excellent environmental stability achieved a high PCE of over 23% [181]. Chen *et al* carefully designed a cross-linkable monomer (5-(1,2-dithiolan-3-yl) pentanehydrazide hydroiodide (TA-NI) with dynamic covalent disulfide bonds, H-bonds, and ammonium. Crosslinked TA-NI shows elastomeric properties and can form 1D PVK, thereby acting as a 'ligament'. These 'ligaments' can play various roles, including passivating grain boundaries, enhancing moisture resistance, releasing residual tensile strain and mechanical stress, and dynamically repairing mechanical cracks caused by bending in PVK films. As a consequence, the recorded PCEs of 23.84% and 21.66% were achieved for FPSCs with active area of 0.062 and 1.004 cm^2 , respectively. Moreover, the FPSCs also show excellent stability with $T_{90} > 20\ 000$ bending cycles [182].

3.7.2. Modification of buried interfaces. Except for the grain boundaries of PVK, the buried interface of FPSCs is a weak link when subjected to external stress. There are differences in properties such as thermal expansion coefficient between PVK and charge transport layer, which can cause tearing under external stress. Accordingly, adopting appropriate interface modification strategies can alleviate the adverse effects of property differences between PVKs and charge transport layers. Liu *et al* introduced a novel multifunctional organic salt, metformin hydrochloride, into the top and buried surface of PVKs to passivate cation and anion defects. Consequently, the FPSCs achieved a impressive PCE of 22.04% with excellent stability and retained 80% of the initial PCE after 10 000 bending cycles [183]. Meng *et al* added 3-aminopropionic acid hydroiodide (3AAH) to the ETL to modify the buried interface. 3AAH can template the growth of PVK grains and improve the quality of ETL, which releases residual stress in PVK and converts it into micro compressive stress. As a consequence, the FPSCs gave a high PCE of 23.36%, and the PCE maintained 84% of their initial value after 4000 bending cycles under a 5 mm bending radius [184]. Cai *et al* added trace amounts of titanium tetrachloride (TiCl_4) to SnO_2 to suppress adsorbed oxygen active sites and oxygen vacancies. The introduction of TiCl_4 helps to passivate defects, increase the conductivity of SnO_2 , optimize the band alignment of interface, and improve device charge extraction, thereby achieving a high PCE of 23.7% at 218 K. Moreover, the device maintained 89% of its initial PCE after 2500 cycles of bending with a 6 mm bending radius [185].

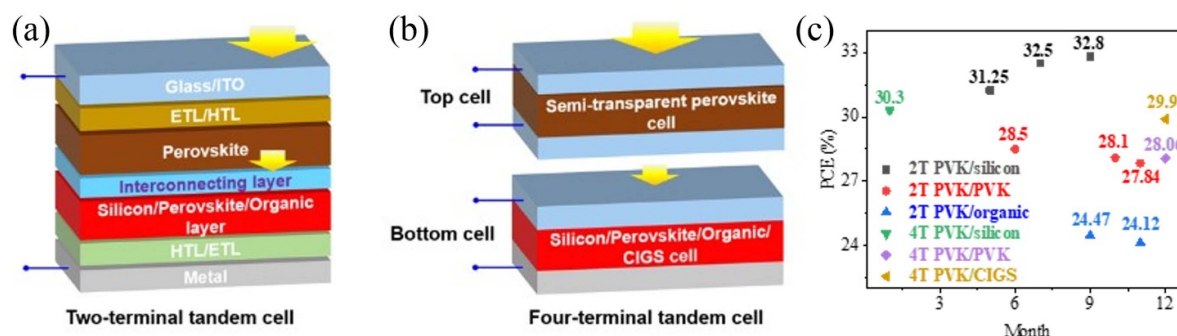


Figure 15. Structure of (a) two-terminal (monolithic) and (b) four-terminal tandem solar cells. (c) The timeline for the landmark efficiency of PVK-based TSCs in 2023 [186–196].

4. PVK-based TSCs

Chuantian Zuo and Liming Ding

Center for Excellence in Nanoscience (CAS), Key Laboratory of Nanosystem and Hierarchical Fabrication (CAS), National Center for Nanoscience and Technology, Beijing 100190, People's Republic of China

4.1. Brief introduction

TSCs contain more than one light harvesting layer with different bandgaps. Double-junction TSCs have a top cell with a wide-bandgap (WBG) light absorber and a bottom cell with a NBG absorber. The top cell absorbs short-wavelength light, whereas the bottom cell absorbs long-wavelength light. This configuration reduces energy loss of the short-wavelength light while maintaining a wide light harvesting range, enabling a higher PCE. TSCs are of two types: two-terminal (2T, monolithic) and four-terminal (4T) (figures 15(a) and (b)). In this section, the main progresses in PVK-based TSCs, including PVK/silicon, PVK/PVK, PVK/organic, and PVK/CIGS TSCs, will be discussed. The easily tunable bandgaps of PVKs make them ideal for TSCs. Figure 15(c) exhibits the timeline for the landmark efficiency of PVK-based TSCs in 2023. Driven by the progresses in new materials and fabrication methods, the PCEs of PVK-based TSCs improved considerably in 2023 [186–196]. In addition, representative high-efficiency research results of different types of TSCs were summarized, including device structure and photovoltaic parameters, as shown in tables 1 and 2. The high efficiencies of different types of TSCs were listed to provide an intuitive understanding of TSC research in 2023.

4.2. 2T PVK/silicon TSCs

PVK/silicon TSCs use WBG PVKs (~ 1.68 eV) and silicon layers for the top and bottom cells, respectively. Mariotti *et al* fabricated PVK/silicon TSCs with a certified PCE of 32.5% via piperazinium iodide interfacial modification to improve the band alignment, reduce nonradiative recombination, and enhance charge extraction in the PVK top cell [187]. Aydin improved the SAM coverage using ultrathin (5 nm) amorphous indium zinc oxide (IZO) as the interconnecting TCO,

achieving an independently certified PCE of 32.5% [186]. Chin *et al* developed a tandem cell with a PVK layer conformally coated on a silicon bottom cell featuring micrometric pyramids (industry standard) to improve its photocurrent and obtained a certified PCE of 31.25% (1.17 cm^2) [188]. Liu *et al* implemented a sequential interface engineering strategy that involved the deposition of ethylenediamine diiodide (EDAI_2) and 4-fluoro-phenethylammonium chloride (4FPEACl) sequentially to improve the PCE of the PVK top cell. TSCs with double-textured silicon featuring sub-micrometer pyramid structures exhibited a stabilized PCE of 29.6% (1 cm^2) (certified 29.0%) [197]. Zheng *et al* incorporated a tunneling recombination layer comprising boron- and phosphorus-doped polycrystalline silicon into the tandem cell to improve the charge carrier transport and obtained a PCE of 29.2% (28.76% certified) [198]. Ren *et al* found that adding a small amount of cadmium acetate (CdAc_2) into the PbI_2 solution promoted favorable crystal orientation and suppressed nonradiative recombination in the PVK layer, yielding a PCE of 29.25% (0.5003 cm^2) for PVK/silicon TSCs [199]. Besides the improvement in small-area cells, hundred-watt power systems, outdoor measurements, degradation-dependent energy yields, reverse-bias resiliences, large-area tandem modules, and efficiency loss analysis of PVK/silicon TSCs were investigated [200, 214–218].

4.3. 2T PVK/PVK TSCs

PVK/PVK (all-PVK) TSCs comprise a WBG PVK top cell and NBG PVK bottom cell. The WBG PVK has a bandgap of ~ 1.78 eV (e.g. $\text{FA}_{0.8}\text{Cs}_{0.2}\text{Pb}(\text{I}_{0.62}\text{Br}_{0.38})_3$), while the NBG PVK has a bandgap of ~ 1.25 eV (e.g. $\text{FA}_{0.7}\text{MA}_{0.3}\text{Pb}_{0.5}\text{Sn}_{0.5}\text{I}_3$) [189]. Lin *et al* designed an immiscible 3D/3D bilayer PVK heterojunction to suppress the interfacial nonradiative recombination and facilitate charge extraction, thereby enhancing the PCEs of single-junction Pb–Sn cells and TSCs to 23.8% and 28.5% (certified 28.0%), respectively [189]. He *et al* developed a SAM material ((4-(7H-dibenzo[c,g]carbazol-7-yl)butyl)phosphonic acid) as the HTL for WBG PSCs to reduce energy loss. All-PVK TSCs with a PCE of 27.0% (certified 26.4%) and an aperture area of 1.044 cm^2 were fabricated [203]. Liu *et al* reported a diammonium-methylthio dual passivation strategy to passivate the defects in PVKs,

Table 1. Summary of the performance of two-terminal PVK-based tandem solar cells.

Type	Structure	V_{oc} (V)	J_{sc} (mA cm ⁻²)	FF (%)	PCE (%)	References
PVK/silicon	Ag finger/MgF ₂ /IZO/SnO ₂ /PDAI/LiF/C ₆₀ /PVK/2PACz/IZO/nc-Si(n)/a-Si(i)/c-Si/a-Si(i)/IZO/MgF ₂ /Ag	1.949	20.9	80.5	32.8	[186]
	Ag contact/LiF/IZO/SnO ₂ /PI + C ₆₀ /PVK/2PACz/TCO/Si heterojunction	1.98	20.24	81.18	32.5	[187]
	Ag finger/MgF ₂ /IZO/SnO ₂ /C ₆₀ /PVK/Me-4PACz/ITO/nc-SiH(n ⁺ /p ⁺)/a-SiH(i/n)/c-Si/a-SiH(i)/nc-Si:H(p)/ITO/Ag	1.91	20.47	79.8	31.25	[188]
	Ag finger/MgF ₂ /IZO/SnO ₂ /C ₆₀ /PVK/NiO/MeO-2PACz/ITO/a-Si:H(i/n)/c-Si(n)/a-Si:H(i/p)/ITO/Ag	1.941	20.1	76.6	29.8	[197]
	Ag finger/LiF _x /IZO/BCP/C ₆₀ /PVK/MeO/poly-Si(p ⁺)/poly-Si(n ⁺)/SiO _x /c-Si/SiO _x /poly-Si(p ⁺)/Cr/Ag	1.83	19.7	81.0	29.2	[198]
	PDMS/Ag/IZO/SnO ₂ /C ₆₀ /PVK/HTL/ITO/a-Si:H(n)/a-Si:H(i)/c-Si/a-Si:H(i)/a-Si:H(p)/ITO	1.86	19.77	79.38	29.25	[199]
	Ag finger/MgF _x /IZO/BCP/Ag/C ₆₀ /PVK/IZO/SAM/poly-Si(n)/SiO _x /c-Si(n)/SiO _x /poly-Si(p)/Cr/Ag	1.85	19.4	81.8	29.3	[200]
	ITO/NiO/SAM/WBG PVK/C ₆₀ /SnO ₂ /Au/PEDOT:PSS/NBG PVK/C ₆₀ /BCP/Cu	2.112	16.5	81.9	28.5	[189]
PVK/PVK	FTO/NiO _x /Me-4PACz/WBG PVK/C ₆₀ /SnO _x /Au/PEDOT:PSS/NBG PVK/C ₆₀ /SnO _x /Ag	2.14	15.6	84.0	28.1	[191]
	ITO/NiO/SAM/WBG PVK/C ₆₀ /ALD-SnO ₂ /IC-CH/NBG PVK/C ₆₀ /ALD-SnO ₂ /Cu	2.11	16.7	79.5	28.1	[201]
	ITO/NiO _x -SAM/WBG PVK/C ₆₀ /ALD-SnO ₂ /ITO NCs/NBG PVK/C ₆₀ /ALD-SnO ₂ /Cu	2.135	16.2	81.5	28.1	[202]
	ITO/2PACz/WBG PVK/C ₆₀ /ALD-SnO ₂ /Au/PEDOT:PSS/NBG PVK/C ₆₀ /BCP/Cu	2.11	16.02	82.2	27.84	[190]
	ITO/SAM/WBG PVK/C ₆₀ /SnO ₂ /IZO/PEDOT:PSS/NBG PVK/C ₆₀ /SnO ₂ /Cu	2.11	15.37	83.13	27.01 (1 cm ²)	[203]
	ITO/Cl@MZO/CsPbI ₂ Br/PM6/MoO ₃ /Ag/PFN-Br/PM6:BTP-eC9/MoO ₃ /Ag	2.152	13.89	80.57	24.07	[204]
	ITO/NiO _x /2PACz/FA _{0.8} Cs _{0.2} Pb(I _{0.5} Br _{0.5}) ₃ /C ₆₀ /BCP/Au/MoO _x /PM6:PM7:Y6:PC ₇₁ BM/C ₆₀ /BCP/Ag	2.14	14.17	80.71	24.47	[192]
PVK/organic	FTO/c-TiO ₂ /mp-TiO ₂ /CsPbI _{2.2} Br _{0.8} /PTACl/PBDB-T/MoO ₃ /Ag/ZnO/PDIN/PM6:Y6:PC ₆₁ BM/MoO ₃ /Ag	2.11	13.65	80.1	23.07	[205]
	ITO/MeO-2PACz/FA _{0.8} Cs _{0.2} Pb(I _{0.6} Br _{0.4}) ₃ /C ₆₀ /CC1-P/ITO/MoO ₃ /PM6:BTP-eC9:PC ₇₁ BM/TPMA/Ag	2.09	14.58	78.99	24.07	[206]
	ITO/ZnO/SnO ₂ /MAFm/CsPbI ₂ Br/MAFm/PDCBT/MoO ₃ /Au/ZnO/BCP/PM6:CH1007/MoO ₃ /Ag	2.10	14.23	77.70	23.21	[207]
	ITO/4PACDB/FAMACsPb(I _{0.5} Br _{0.5}) ₃ /C ₆₀ /SnO ₂ /Au/MoO ₃ /PM6:BTP-eC9:PCBM/PNDIT-F3N/Ag	2.197	14.15	77.6	24.12	[193]

achieving a PCE of 28.1% [191]. Zhou *et al* introduced aspartate hydrochloride (AspCl) into both the HTL and bulk PVK layers, followed by another AspCl treatment to improve the performance of Sn–Pb cells. The PCEs of 22.46% and 27.84% (certified 27.34%) were achieved for single-junction Sn–Pb cells and all-PVK TSCs, respectively [190]. Liu *et al* used mixed carbazolyl hole-selective molecules to anchor on ITO NCs to improve the subcell performance, thereby achieving a PCE of 28.1% for TSCs [201]. Wen *et al* used a 3D to 2D PVK conversion approach to prepare 2D PVKs ($n \geq 2$) atop WBG PVK layers (1.78 eV), achieving PCEs of 19.6% and 28.1% for WBG PVK cells and TSCs, respectively. Some other strategies were also developed to improve the performance of subcells and TSCs, such as surface treatment, addition

of additives into the PVK precursors, and modification of the charge transport layers [202, 219–223]. In addition to these strategies for improving the PCE, tandem solar modules and strategies to reduce cost were also reported [224–226].

4.4. 2T PVK/organic TSCs

PVK/organic TSCs use low-bandgap organic photovoltaic materials in the bottom cells [227–230]. Mali *et al* fabricated inorganic CsPbI_{2.2}Br_{0.8} PVK/organic TSCs with a PCE of 23.07% [205]. Sun *et al* used CsPbI₂Br to fabricate inorganic PVK/organic TSCs and achieved a PCE of 23.21% [207]. Jiang *et al* developed Cl@MZO ETL to improve the energy level alignment in CsPbI₂Br PVK/organic TSCs, achieving

Table 2. Summary of the performance of four-terminal PVK-based tandem solar cells.

Type	Structure	Top cell PCE (%)	Bottom cell PCE (%)	Total PCE (%)	References
PVK/silicon	Top: ITO/SnO ₂ /PVK/Spiro-OMeTAD/MoO ₃ /IZO/Au Bottom: PERL silicon cell	22.6	7.7	30.3	[194]
	Top: ITO/SnO ₂ /ZnO/PVK/Spiro-OMeTAD/MoO ₃ /ITO Bottom: TOPCon silicon cell	19.15	9.68	28.83	[208]
	Top: ITO/MeO-2PACz/PVK/C ₆₀ /BCP:Ag/IZO/MgF _x Bottom: TOPCon silicon cell	19.2	9.2	28.4	[209]
PVK/PVK	Top: ITO/MeO-2PACz/1.66 eV PVK/C ₆₀ /SnO ₂ /ITO Bottom: ITO/PEDOT:PSS/1.25 eV PVK/C ₆₀ /BCP/Cu	20.13	7.93	28.06	[195]
	Top: ITO/MeO-2PACz/PVK/C ₆₀ /SnO ₂ /ITO Bottom: ITO/PEDOT:PSS/1.25 eV PVK/C ₆₀ /BCP/Cu	19.82	7.25	27.07	[210]
	Top: ITO/DCB-BPA/1.77 eV PVK/C ₆₀ /SnO ₂ /IZO Bottom: ITO/PEDOT:PSS/1.25 eV PVK/C ₆₀ /BCP/Cu	17.87	9.03	26.9	[211]
PVK/CIGS	Top: ITO/NiO _x /PVK/C ₆₀ /SnO _x /ITO/LiF Bottom: Mo/CIGS/CdS/i-ZnO/ZnO:Al	21.8	7.3	29.9	[196]
	Top: ITO/poly-TPD/PVK/C ₆₀ /SnO _x /IZO Bottom: Mo/CIGS/CdS/i-ZnO/AZO	19.1	9.3	28.4	[212]
PVK/organic	Top: ITO/SnO ₂ /ZnO/CsPbI _{2.25} Br _{0.75} /PTAA/MoO ₃ /ITO Bottom: ITO/PEDOT:PSS/D18-Cl-B:N3:PC ₆₁ BM/PDIN/Ag	15.52	6.82	22.34	[213]

a PCE of 24.07% [204]. Ma *et al* fabricated PVK/organic TSCs with a PCE of 24.07% using a organic–inorganic hybrid PVK, FA_{0.8}Cs_{0.2}Pb(I_{0.6}Br_{0.4})₃ [206]. Wang *et al* modulated the surface of WBG FA_{0.8}Cs_{0.2}Pb(I_{0.5}Br_{0.5})₃ PVK to reduce energy loss, achieving a high V_{oc} of 1.35 V for WBG PVK cells. TSCs with an FF of 83.29% and a PCE of 24.47% were also fabricated [192]. An *et al* used a multifunctional phenylethylammonium acetate (PEAAc) additive to improve the performance of the PVK layer, achieving a PCE 24.12% for PVK/organic TSCs [193]. The PCE of PVK/organic TSCs is limited by the organic subcell, which reduces the light loss of the interconnecting layer. Improving the performance of the organic layer considerably improved the PCE [207, 231].

4.5. 4T TSCs

Four-terminal (4T) TSCs underwent considerable development in 2023. Contrary to 2T TSCs, 4T TSCs comprise two independent subcells (top cell and bottom cell); therefore, they do not require photocurrent matching between the subcells. Wu *et al* fabricated 4T PVK/silicon TSCs with a PCE of 28.4%

by reconstructing the ITO surface of the top cell using hydrofluoric acid [209]. Li *et al* fabricated 4T PVK/silicon TSCs with a PCE of 28.84% using an *in situ* epitaxial growth strategy to improve the PCE of the top cell [208]. Duong *et al* reported a PCE of 30.3% for 4T PVK/silicon TSCs, in which the performance of the top cell was improved by the addition of 4M-PEACl into the PVK precursor [194]. Hu *et al* reported 4T PVK/PVK TSCs with a PCE of 26.3% [232]. Li *et al* synthesized a new SAM material for top PVK cells and achieved a high V_{oc} of 1.339 V. They further fabricated 4T PVK/PVK TSCs with a PCE of 26.9% [211]. Zhang *et al* reported a bottom-up modification method to enhance the performance of NBG Pb–Sn PVK bottom cells, thereby achieving a PCE of 27.07% for 4T PVK/PVK TSCs [210]. Improving the performance of WBG PVK via ligand anchoring increased the PCE of 4T PVK/PVK TSCs to 28.06% [195]. Liu *et al* fabricated 4T PVK/CuInGaSe₂ TSCs with a 28.4% PCE by optimizing the subcells and ensuring their bandgap matching [212]. Liang *et al* reported a PCE of 29.9% for 4T PVK/CuInGaSe₂ TSCs, which were realized via carrier and optical management [196]. Liu *et al* reported 4T PVK/organic TSCs with a PCE of 22.34% [213], which was lower than the other PVK-based

TSCs, due to the lack of high-performance organic photovoltaic materials. Thus, the PCE will increase obviously if better organic materials are developed.

4.6. Summary

The progresses in charge-transporting materials, interconnecting layers, and preparation techniques of the subcells have considerably enhanced the PCE of PVK-based TSCs. Currently, the PCEs of these cells are considerably lower than the theoretical limit, which can be improved by developing low-loss interconnecting layers and improving the performance of subcells TSCs.

5. PSMs

Xiaoxuan Liu¹ and Zonghao Liu^{1,2}

¹Wuhan National Laboratory for Optoelectronics, Huazhong University of Science and Technology, Luoyu Road 1037, Wuhan 430074, People's Republic of China

²Optics Valley Laboratory, Hubei 430074, People's Republic of China

5.1. Brief introduction

The rapid development of PSCs makes it the most-promising emerging photovoltaic technology. Remarkable progress in their efficiency and stability has been demonstrated in lab-scale small-area PSCs. However, PSCs must be upscaled to module scale to successfully transition toward commercialization [233, 234]. In the past years, several scalable fabrication methods have been proposed for the fabrication of PSMs, such as blade coating, slot-die coating, spray coating, inkjet printing, screen printing, and vapor deposition [233, 235–239]. Herein, we will briefly summarize the progress in the scalable fabrication of PSMs.

5.2. Blade coating

Figure 16(a) shows the blade coating method used for PSM fabrication [240]. In blade coating, solvent engineering is commonly used to optimize the ink-dispersing properties, ink viscosity, and surface tension as well as PVK nucleation/growth process for fabricating high-efficiency PSMs [241, 242]. DMSO and *N,N*-dimethylformamide (DMF) are commonly used solvents for PVK solutions as they can coordinate with the lead-iodine octahedron and form an intermediate phase. They then volatilize to form the PVK phase during annealing [243]. DMSO evaporates and the amorphous regions move to the bottom of PVK films during film formation, thereby decreasing the device performance [244]. Fei *et al* innovatively introduced bathocuproine (BCP), a lead chelation molecule (LCM), into the HTL [245]. BCP strongly interacted with Pb²⁺ and weakened the interaction of DMSO with Pb²⁺. Thus, the amount of DMSO vestige reduced, which effectively reduced the amorphous regions at the bottom of PVK

films and passivated the PVK bottom surface (figure 16(b)). The target module showed a high certified PCE of 21.8%, with an aperture area of 26.9 cm² (figure 16(c)). Yan *et al* reported a new PVK solution system comprising 2-ME/1,3-dimethyl-imidazolidinone (DMI) [246]. Compared with the traditional PVK solution system based on DMF/DMSO or 2-Me/NMP, DMI exhibited an appropriate dipole polarity and higher solvation energy, which was favorable to the formation of a relative PbI₂–DMI stable intermediate and easier to pull out (figure 16(d)). Moreover, the retarded crystallization of the PbI₂–DMI intermediate enabled a broader operation window than other mixtures (figure 16(e)). The 2-Me/*N*-methyl pyrrolidone (NMP)-based PSM device exhibited a champion PCE of 20.10% and 20.15% with an aperture area of 36 and 81 cm², respectively. Additive engineering is also an effective strategy for fabricating high-efficiency PSMs. As effective additives, surfactants can ameliorate the interfacial wettability and enhance the quality of PVK films, which is favorable for fabricating PVK films for PSMs. Liu *et al* systematically investigated 14 types of quaternary ammonium cationic surfactants (QACs) as additives for fabricating large-area PVK films and found that double-chain QACs exhibited superior capability in regulating the PVK crystallization behavior (figure 16(f)) [247]. They demonstrated that dimethyldioctadecylammonium bromide (DMDO) is the optimal cationic surfactant. As shown in figure 16(g), the DMDO-modified devices achieved a champion PCE of 19.74% with an active area of 175 cm². Furthermore, Gu *et al* developed bifacial PVK modules with a p–i–n architecture using the doctor blade method (figures 16(h) and (i)) [234]. The bifacial modules achieved a front efficiency of 20.2% (certified 19.2%), comparable to opaque mono-facial counterparts. Their rear efficiency was 15.0% (certified 14.1%), with an aperture area of ~22.0 cm² (figure 16(j)).

5.3. Slot-die coating

Slot-die coating is a precise coating technique that has a faster coating speed and yields higher accuracy and more-uniform film thickness during the continuous scalable fabrication of PSMs than blade coating (figure 17(a)) [248]. Similar to doctor blade method, the engineering of PVK precursor solutions is important for fabricating high-quality large-area PVK films and high-efficiency PSMs via slot-die coating. Li *et al* used acetonitrile (ACN) as a cosolvent to regulate the viscosity of 2-Me based PVK precursor inks [249]. The introduction of ACN can ameliorate the uniformity of PVK films and avoid unfavorable film microstructure (figure 17(b)). At an optimized amount of 46 vol% ACN, a champion PCE of 17.1% with an active area of 12.7 cm² was achieved (figure 17(c)). Meanwhile, Na *et al* reported a rheological engineering-based locally supersaturated PVK ink (LSPI) strategy, in which a small amount of 1,2-dichlorobenzene (DCB) was added to DMSO and used for the slot-die coating of large-area PVK films for PSM fabrication (figure 17(d)) [250]. The DCB can adjust the rheological properties of the DMSO-based PVK precursor ink, lower its high surface tension and ink viscosity,

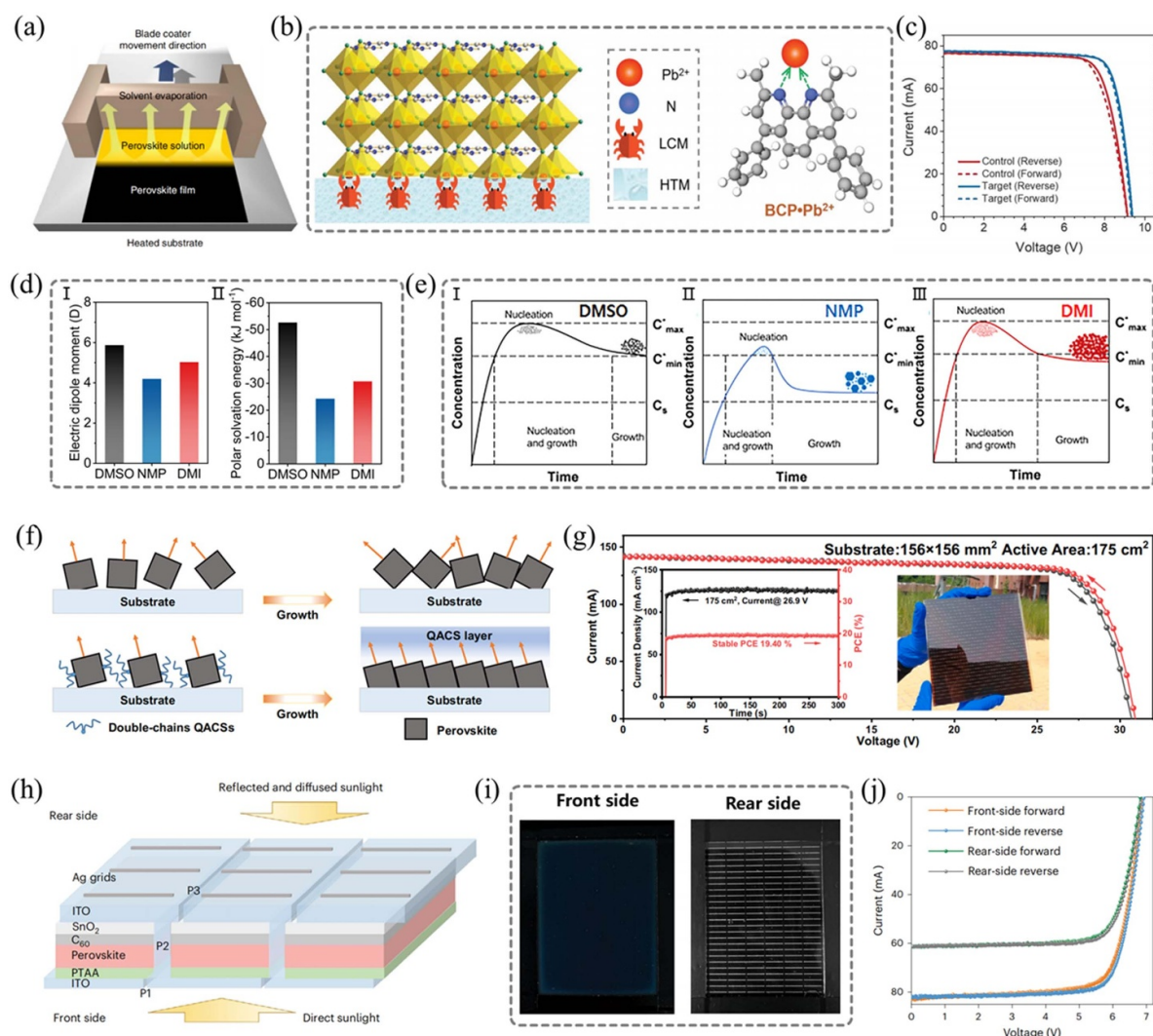


Figure 16. (a) Schematic of the blade coating method. Reproduced from [235], with permission from Springer Nature. (b) Illustration of the chelation of the LCMs (in the HTL) with Pb^{2+} ions at the bottom side of the PVK films. (c) $I-V$ curves of the control and target modules. (b), (c) From [245]. Reprinted with permission from AAAS. (d) (I) Electric dipole moment and (II) polar solvation energy of DMSO, NMP, and DMI. (e) Schematic of the nucleation and crystallization of (I) DMF/DMSO, (II) 2-Me/NMP, and (III) 2-Me/DMI complexes based on LaMer mechanism. (d), (e) [246] John Wiley & Sons. © 2023 The Authors. Advanced Energy Materials published by Wiley-VCH GmbH. (f) Schematic of the crystallization of control and double-chain QACS-based PVK. (g) $I-V$ curves of the champion DMDO module. The left inset shows the steady-state power output and current of the champion module. The right inset shows an image of the module. (f), (g) Reprinted from [247], © 2023 Elsevier Inc. (h) Structure of the PVK bifacial module. P1, P2, and P3 are the three scribing lines in thin-film modules connected in series. (i) An image of the PVK bifacial module from the front and rear sides with Ag grids, respectively. The aperture area size of the module is $39\text{ mm} \times 55\text{ mm}$. (j) $I-V$ curves of the champion bifacial module with light coming from the front and rear sides. (h)–(j) Reproduced from [234], with permission from Springer Nature.

and form locally supersaturated PVK colloids (figure 17(e)). Moreover, DCB improved the infiltration of PVK precursor inks on the NiO-coated ITO substrate and decreased the contact angle from 37.06° to 11.02° , resulting in a more-uniform and thicker film (figures 17(f) and (g)). This strategy delivered uniform PVK films and a high PCE of 18.66%, with an active area of 8.64 cm^2 . In addition to the rheological properties of PVK precursor inks, abundant intrinsic point defects and surface imperfections were formed during fabrication. These issues affect the overall device performance. Mathews

et al introduced a hydrophobic all-organic salt, fluorinated anilinium benzyl phosphonate (FABP), to modify the top surface of the PVK layer fabricated via slot-die coating [251]. FABP has two anchoring functional groups that binding to the FA-site vacancy and undercoordinated Pb ions, exhibiting secondary interactions with the PVK surface (figure 17(h)). This salt could efficiently passivate the defects and inhibit their migration on the PVK surfaces. The treated PSMs realized high PCEs of 19.28% (active area of 58.5 cm^2) (figure 17(i)) and 17.62% (aperture area of 64 cm^2), respectively.

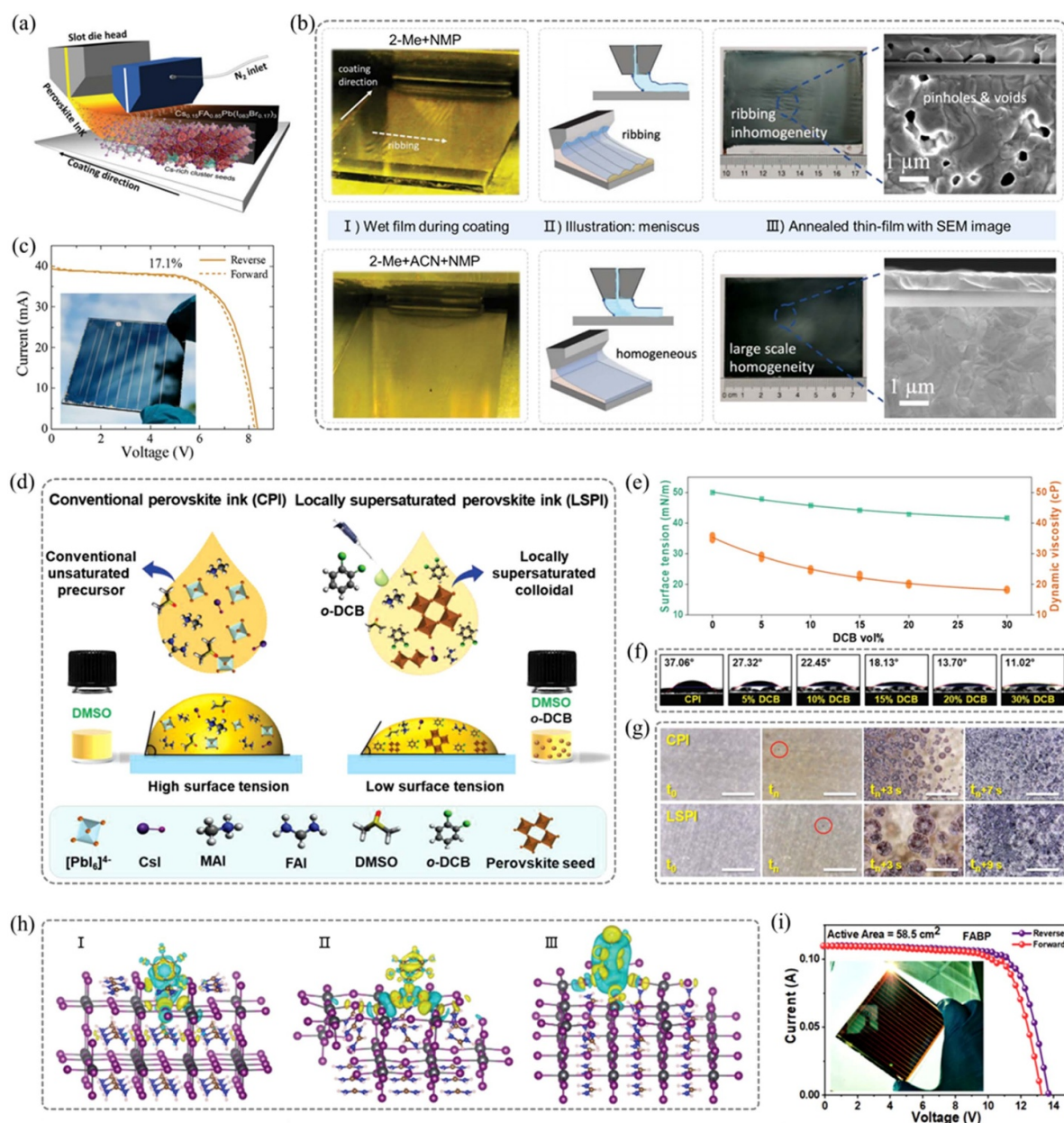


Figure 17. (a) Schematic of slot-die coating. [251] John Wiley & Sons. © 2023 Wiley-VCH GmbH. (b) Comparison of PVK layer homogeneity for two precursor inks: 92-vol% 2-Me/8-vol% NMP/0-vol% ACN and 46-vol% 2-Me/8-vol% NMP/46-vol% mixed inks. (I) Images of the as-coated wet PVK film; (II) sketches of the meniscus and resulting ribbing phenomena are illustrated; and (III) images of the annealed PVK film and corresponding top-view (above) and cross-sectional (below) SEM images. (c) I - V curves of a PSM; the inset is a corresponding optical image. (b), (c) Reproduced from [249]. CC BY 4.0. (d) Schematic of the locally supersaturated PVK precursor inks. (e) Changes in surface tension and dynamic viscosity of PVK precursor inks with different DCB contents. (f) Contact angles of the corresponding PVK precursor ink with different DCB contents measured on the NiO-coated ITO substrate. (g) *In situ* optical microscopy images with a scale bar 100 μm showing the crystal growth process in conventional PVK ink (CPI) and LSPI-based PVK films (t_0 represents the PVK wet film state and t_n represents the initiation of nucleation and grain growth). (d)-(g) [250] John Wiley & Sons. © 2023 Wiley-VCH GmbH. (h) DFT calculations of FAPB-treated films. Yellow (cyan) denotes the charge accumulation (losses) of the FAPbI₃ surface with (I) FA vacancy passivated by pentafluoroanilinium cation; (II) I vacancy passivated by pentafluorobenzyl phosphonate anion; and (III) Pb vacancy passivated by pentafluoroanilinium cation. (i) I - V curve of the best-performing passivated PSMs (inset: PSM with 13 subcells). (h), (i) [251] John Wiley & Sons. © 2023 Wiley-VCH GmbH.

5.4. Spray coating

Spray coating is a low-temperature deposition technique widely used in the manufacturing industry (figure 18(a)). The mass and thickness of the film can be controlled by controlling

the precursor ink concentration, spray speed, and number of spray cycles. This method can be used to manufacture PSCs with low cost, high volume, rapid manufacturing, and high material utilization. However, during the spray coating process, the newly sprayed droplets will dissolve the formed films.

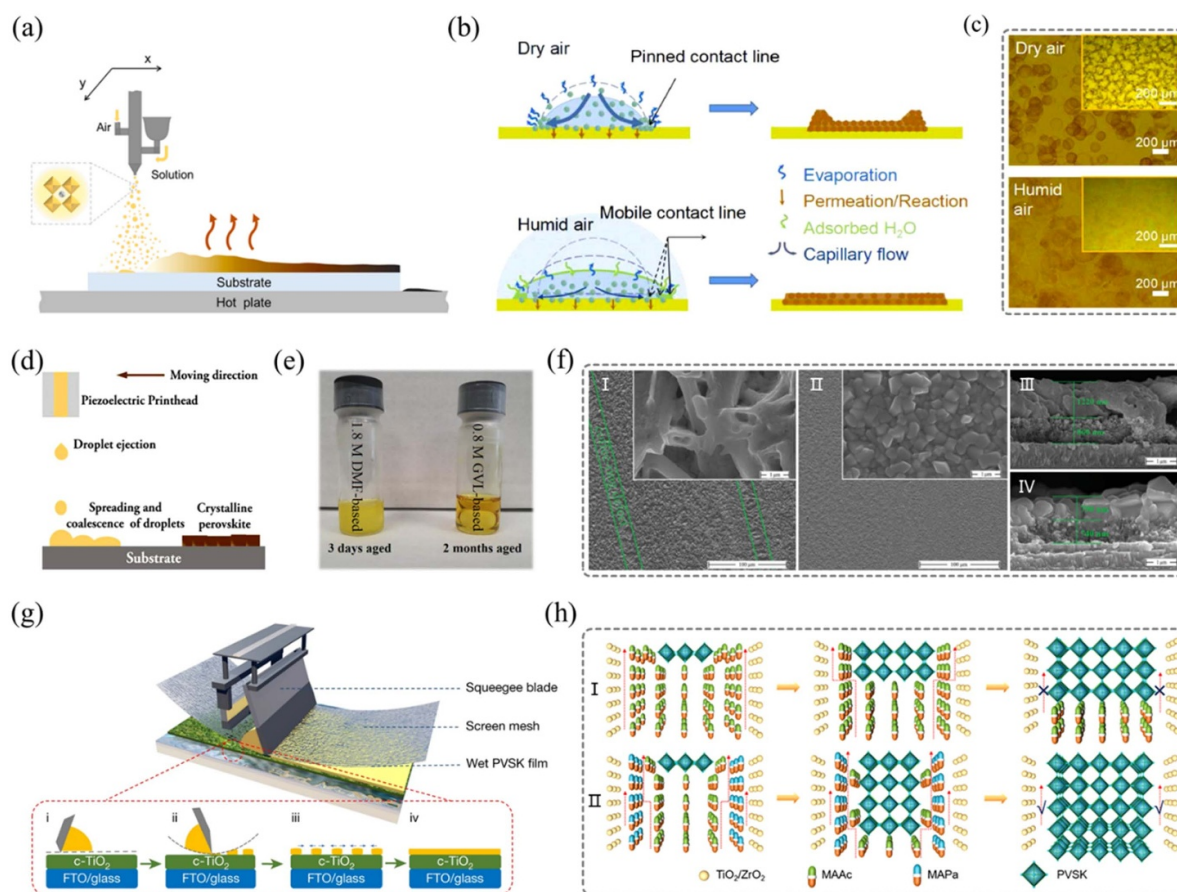


Figure 18. (a) Schematic of spraying coating. Reprinted from [236], © 2022 Elsevier B.V. All rights reserved. (b) Schematic of the drying behavior of droplets sprayed in dry air and humid air. (c) Optical microscopy (OM) images of the films prepared by spraying the trace solution on CsI/PbI₂ film in dry and humid air; insets are the corresponding OM images of freshly formed films without annealing after complete spraying. (b), (c) Reprinted from [253], © 2023 Elsevier Ltd. All rights reserved. (d) Schematic of inkjet printing. [237] John Wiley & Sons. © 2021 Wiley-VCH GmbH. (e) Image of the aged PVK precursor inks. (f) Top-view and cross-sectional SEM images of the PVK layer fabricated on top of the m-TiO₂ layer using (I), (III) 1.8 M DMF- and (II), (IV) 0.8 M GVL-based PVK precursor inks. (e), (f) Reproduced from [254]. CC BY 4.0. (g) Diagram of the screen printing method for the deposition of PVK films. Reproduced from [238], with permission from Springer Nature. (h) Schematic of the growth process of the PVK NCs in the mesoporous layer based on (I) MAAc and (II) MAAc/MAPa solvent systems. [255] John Wiley & Sons. © 2023 Wiley-VCH GmbH.

This affects the coverage of the film, and the sputtered droplets pollute the production environment. In addition, poor reproducibility is common in the spray-coated device, primarily due to moisture gradually being absorbed into PVK precursor materials, as well as the ‘coffee ring’ effect (CRE) induced by the non-uniform evaporation of the solution [252]. Cheng *et al* systematically studied the effect of humidity on the crystallization and morphology of spray-coated PVK films. They discovered that an appropriate RH level can suppress the CRE and result in the formation of a uniform film (figure 18(b)) [253]. The morphology of PVK film deposited in humid air shows more homogeneous and dense deposition than that deposited in dry air (figure 18(c)). Hence, they present a moisture-assisted strategy that involves spraying a water-containing PVK precursor ink in a suitable humidity environment to inhibit the CRE while simultaneously regulating crystallization. Thus, the device showed an optimal PCE of 16.75% (an active area of 64.8 cm²) and exhibited superior device reproducibility with an average PCE of 16.08 ± 0.32%.

5.5. Inkjet printing

Inkjet printing is a technique for fabricating multifunctional layers using uniform, colloidal liquid-phase ink. In this technique, the PVK precursor ink is poured into the ink cartridge. Then, the ink nozzle is pointed at the substrate and the ink evenly ejects, such that the PVK precursor solution is evenly deposited on the substrate (figure 18(d)). The ink nozzle controls the PVK precursor ink size and deposition trajectory. The main processing advantages of this method are that it can scale from small-area lab cells to large-area industrial production, with low cost and less material consumption [237]. Chalkias *et al* introduced a solution system comprising gamma-valerolactone (GVL), a green solvent, to replace the toxic solvent, DMF [254]. The 0.8 M GVL-based PVK precursor ink exhibited high performance and stability and could be used for high-quality PVK film preparation even after storing for 2 months at room temperature in the dark. However, the 1.8 M DMF-based PVK precursor ink became

turbid after a few days (figure 18(e)). The PVK film prepared using the 1.8 M DMF-based ink showed an uneven and rod-shaped PVK structure, resulting in incomplete surface coverage (figure 18(f)). In contrast, uniform and compact PVK films without pinholes and caves were obtained using the 0.8 M GVL-based ink (figure 18(f)). Notably, the champion PSM achieved a PCE of 10.07%, with an active area of 52.4 cm².

5.6. Screen printing

In screen printing, a rubber scraper is used to force the ink through the screen mesh and print it on a substrate (figure 18(g)) [238]. The ink should have high viscosity because low-viscosity traditional organic solvents pose difficulties in the screen printing of PVK films and do not meet the required standards. ILs are potential solvents for precursor inks to realize the screen printing of PVK films owing to its adjustable viscosity, negligible vapor pressure, and excellent chemical stability. Chen *et al* used methylamine acetate (MAAc) as the IL to regulate the viscosity of PVK precursor inks and introduced methylamine propionate (MAPa) as the cosolvent to control the coordination ability and volatilization rate of MAAc, thereby controlling the PVK crystallization process [255]. MAPa has strong coordination abilities and a lower volatilization rate, and it establishes solvent volatilization channels in the mesoporous structure during annealing. This promotes complete MAAc volatilization and considerably improves the filling degree of PVK crystals in the mesoporous structure. MAPa is also beneficial for the vertical growth of PVK crystals, and nonvolatile MAPa can coordinate with unbonded Pb²⁺ on the PVK surface, resulting in the efficient charge exaction and energy level alignment (figure 18(h)). Finally, fully printed PSM device, which uses 75% MAAc + 25% MAPa solvent systems, yields a champion PCE of 11.8%, with an active area of 16.37 cm².

5.7. Vapor deposition

Vapor deposition, including physical vapor deposition and chemical vapor deposition (CVD), is a conventional method for depositing large-area and uniform PVK films without using solvents. It is a promising technology for the scaled-up production of PSCs (figure 19(a)) [239]. However, the efficiency of vapor-deposited PSCs is considerably lower than that of PSCs fabricated using solutions. This seriously limits the application of vapor deposition for PVK industrialization.

The uncontrollable top-down reaction between organic vapor and solid substrate during vapor deposition may lead to the formation of PVK films with inferior crystallinity. The films contain small grains with many grain boundaries and small pinholes in the bulk, resulting in the unsatisfactory performance of vapor-deposited PSCs. Wang *et al* proved that a certain amount of solvent vapor can form an intermediate phase at the grain boundaries, resulting in grain coarsening and the secondary growth of small grains into large ones [256]. They effectively regulated grain coarsening and irregular distribution of grain sizes by managing the evolution of the PbI₂–DMSO intermediate phase (figure 19(b)). As shown

in figure 19(c), a diffraction peak can be observed at 10.3° for PbI₂(DMSO)₂, attributed to its conversion to the PbI₂–DMSO intermediate phase during the treatment. Additionally, solvent annealing as a post-treatment method can enhance the quality of vapor-deposited PVK films by eliminating grain boundaries and pinholes. Remarkably, PSMs (10.0 cm²) achieved a champion PCE of 19.9% under AM 1.5G irradiation. Tan *et al* have successfully employed a combination of vacuum evaporation of PbI₂ and solution processing of organic ammonium halide to fabricate PVK films that exhibit large-area homogeneous PVK films with large grains [257]. This approach effectively mitigated the challenges associated with the evaporation of organic ammonium halide while simultaneously capitalizing on the benefits offered by vapor deposition, resulting in a uniform and dense PVK film (figure 19(d)). The resulting vapor-deposited PSMs demonstrated an impressive PCE of 20.0% over an active area of 16 cm². Qi *et al* discovered that oxygen loss in the SnO₂ layer during hybrid chemical vapor deposition (HCVD) increases the interface defect density and carrier recombination [258]. Therefore, they introduced a passivation layer comprising potassium sulfamate (H₂KNO₃S), which mitigated the oxygen loss in SnO₂ and passivated the uncoordinated Pb²⁺ in the PVK film (figure 19(e)). Simultaneously, using NMP as a solvent to dissolve PbI₂ formed the PbI₂•NMP intermediate phase. NMP also plays a crucial role in reducing the energy barrier for PVK nucleation during HCVD (figure 19(f)). Additionally, the incorporation of PVK seeds further influenced the kinetics of PVK crystal growth and enhanced the grain size (figure 19(g)). Thus, the employed PSMs demonstrated champion PCEs of 16.16% (22.4 cm²) and 12.12% (91.8 cm²), respectively.

6. Device stability

Zhenghong Xiong¹, Renhao Zheng², Huimin Zhang² and Pengjun Zhao²

¹ School of Chemical Engineering, Center for Antibonding Regulated Crystals, Sungkyunkwan University, Suwon 16419, Republic of Korea

² State Key Laboratory of Functional Materials and Devices for Special Environmental Conditions; Xinjiang Key Laboratory of Electronic Information Materials and Devices, Xinjiang Technical Institute of Physics & Chemistry, CAS, 40-1 South Beijing Road, Urumqi 830011, People's Republic of China

6.1. Brief introduction

Owing to its instinct chemical properties and device architecture, PSCs suffer instability against environmental stress, including humidity, temperature, and light soaking. These instabilities primarily hinder the commercialization of PVK photovoltaics. Similar to crystalline silicon photovoltaic devices and panels, PSCs must meet the stability standards of IEC61215:2016 qualification tests, i.e. continuous operation for 1000 h under 85 °C and 85% RH simultaneously, described by the International Electrotechnical Commission,

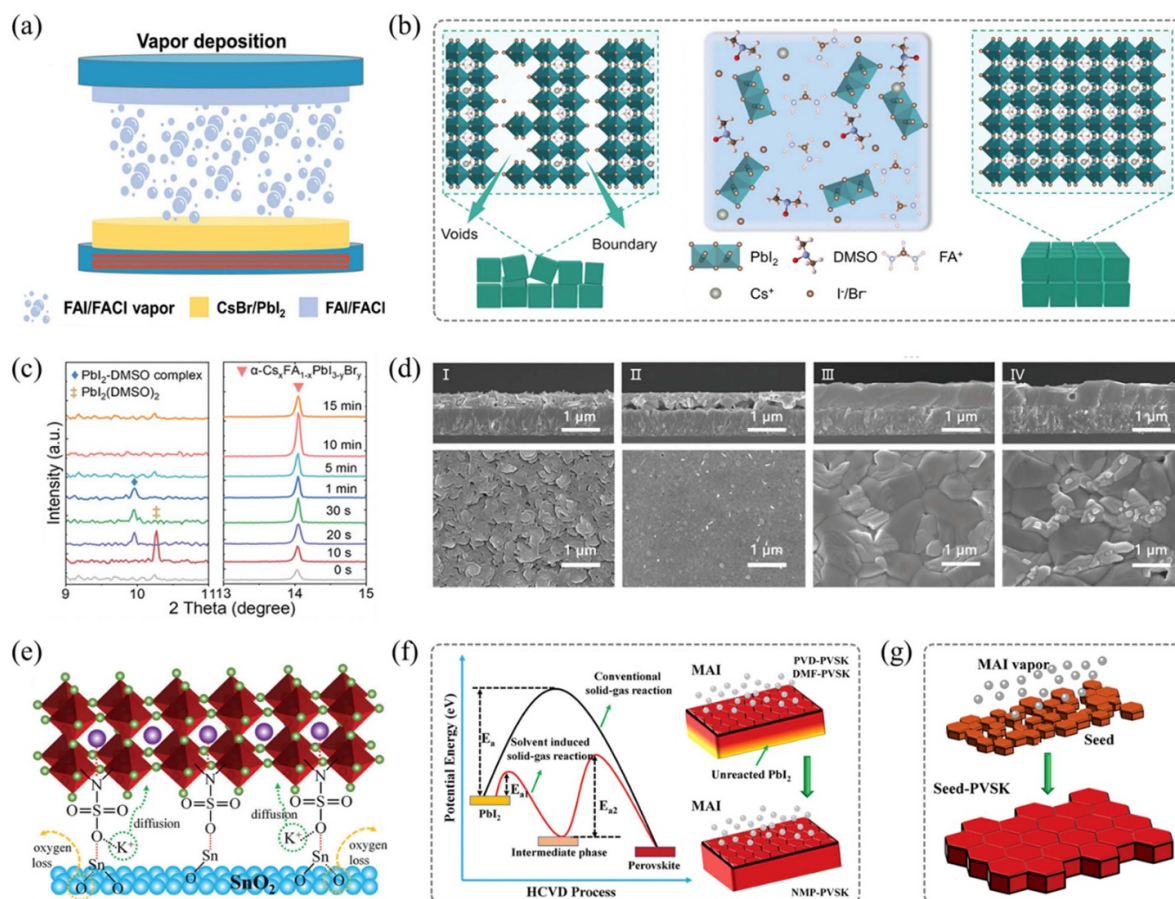


Figure 19. (a) Schematic of CVD. (b) Schematic of spontaneous nucleation crystallization and recrystallization processes. (c) *In situ* XRD patterns of PVK films obtained during the treatment. (a)–(c) [256] John Wiley & Sons. © 2023 Wiley-VCH GmbH. (d) SEM images (cross-section images on top and top-view images on bottom). PbI_2 film deposited by (I) evaporation and (II) solution process. PVK film deposited by (III) evaporation and (IV) solution process. [257] John Wiley & Sons. © 2023 Wiley-VCH GmbH. (e) Schematic of the ETL/PVK interface passivation with $\text{H}_2\text{KNO}_3\text{S}$. (f) Schematic of the nucleation and growth of PVKs. (g) Schematic of the seed growth of PVKs. (e)–(g) [258] John Wiley & Sons. © 2023 The Authors. Advanced Energy Materials published by Wiley-VCH GmbH.

before entering the Energy Market. To accelerate the commercialization of PSCs, several methods have been employed for improving the device stability: PVK composition optimization [259–265], surface and interface passivation [259, 266–271], molecular design of carrier transport material [146, 177, 272–276], electrode modification [277], and rational encapsulation [278, 279], among others [81, 280, 281].

Herein, annual research progress and strategies for improving the device stability under mono environment stress (humidity, temperature, and light soaking) and operating condition will be introduced. Meanwhile, considering the future application in space and flexible electronics, device stability against radiation and mechanical stress will also be briefly described. Note that only the stability of single-junction and lead-based PSCs has been summarized herein.

6.2. Humidity stability

Organic–inorganic hybrid halide PVK is an ionic material that can be relatively easily dissolved in polar solvents, such as water. However, PVKs experience humidity instability [282]. The degradation paths of PVKs with different components are

different. MAPbI_3 degrades under humid conditions as follows: first, the reversible formation of a monohydrated chain of PVK and the formation of dehydrated PVKs with reduced dimensionality occur. Then, water-catalyzed decomposition of MAPbI_3 to PbI_2 , MA, and HI occurs [283–285]. In contrast, during the degradation of FAPbI_3 under humid conditions, cubic-to-hexagonal phase transition tends to occur first. Thus, the FA^+ rotational movement is inhibited under humid condition. Then, the relatively strong hydrogen bonding between FA^+ and water affected the weak interaction between FA^+ and I^- in the $[\text{PbI}_6]^{4-}$ sublattice, inducing irreversible degradation from the hexagonal phase to PbI_2 [286]. Meanwhile, for the degradation of mixed-cation PVK under humid conditions, a surface reaction pathway involving the dissolution of FAI by water and iodide oxidation by oxygen was proposed recently (figure 20(a)). The FAI was shifted into thermodynamically unstable regions by increasing the Cs/FA ratio, leading to undesirable phase transformations [287]. As for mixed Sn–Pb halide PVKs under humid conditions, Hillhouse *et al* revealed that degradation induced by moisture and illumination alone was negligible compared with the effects of oxygen in the mixed Sn–Pb PVK absorbers. Sn^{2+} oxidized

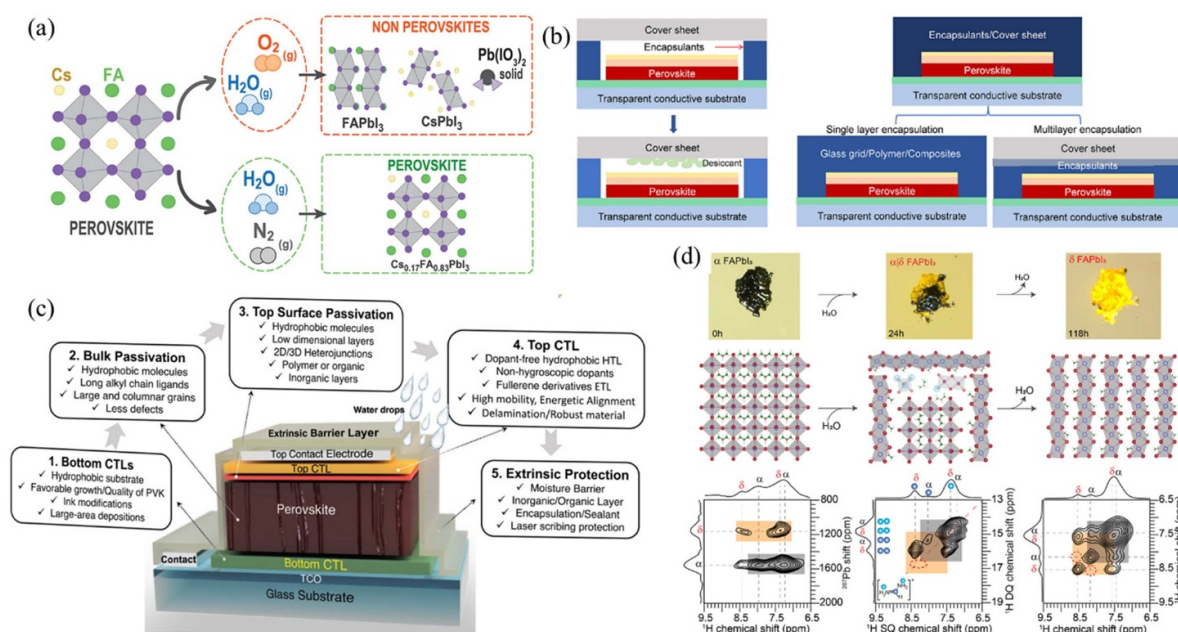


Figure 20. (a) Water and oxygen causing degradation in formamidinium-based halide PVKs. Reproduced from [287]. CC BY 4.0. (b) Encapsulation structures of PSCs with (left) and without the external gap (right). Reprinted from [278], © 2023 Elsevier Inc. (c) Schematics representing the thin-film single-junction PSC architecture before final encapsulation into a module and strategies to circumvent the hygroscopic nature of MHP and hole/electron contacts. [289] John Wiley & Sons. © 2023 Wiley-VCH GmbH. (d) Structural transformation of FAPbI₃ under humid conditions. Reprinted with permission from [290]. Copyright (2022) American Chemical Society.

to Sn⁴⁺, thereby decomposing thin FA_{0.75}Cs_{0.25}Pb_{0.5}Sn_{0.5}I₃ films. In other words, when neutral oxygen molecules were adsorbed onto the absorber surface in unoccupied adsorption sites, the adsorbed oxygen molecules oxidized Sn²⁺ to Sn⁴⁺, yielding V_{Sn}²⁻ vacancies in the PVK crystal. As the number of vacancies increased, the PVK structure was destroyed, producing PbI₂, CsI, FAI, and I₂. Moreover, water accelerated the oxidation of Sn²⁺ to Sn⁴⁺ [288].

Moisture instability of PVKs can be effectively addressed via encapsulation. PVKs are highly sensitive to UV light, temperature, and humidity; therefore, the encapsulation of commercial photovoltaic devices (such as silicon solar cells) must be further improved to avoid the loss of efficiency (figure 20(b)) and ensure the stable operation of PSCs [278, 291, 292]. Nevertheless, encapsulation cannot solve all the issues caused by moisture instability. For instance, the fabrication of photovoltaic modules involves performing several steps, such as laser processing, subcell interconnection, and encapsulation, in ambient atmosphere (figure 20(c)) [289]. Therefore, the moisture resilience of the device itself must be improved. Passivation of the PVK surface/bulk defects [279], increasing the size of PVK grains to reduce grain boundaries [290], and increasing the hydrophobicity of the charge transport layers are effective ways to improve the moisture resilience of PSCs (figure 20(d)) [293, 294].

Moisture-induced performance degradation of PSCs is primarily caused by the mass transfer of metal atoms from the electrode into the PVK layer. To avoid this, alkali metal salts, small organic molecules, polymers, and metal oxides are used as the cathode interlayer to block the

direct contact of the PVK layer with the metal cathode. Yu *et al* [277] used an alcohol-soluble surfactant-encapsulated polyoxometalate complex [(C₈H₁₇)₄N]₄ [SiW₁₂O₄₀] (TOASiW₁₂) in PSCs. TOASiW₁₂/Al-based devices with a PCE of 20.64% can maintain over 80% of the initial PCE after 350 h of storage in an ambient atmosphere with 45% RH, which is superior to that of the commonly used BCP interlayer.

6.3. Thermal stability

The performance of PSCs deteriorates under heat due to the degradation of organic matter in the devices such as the A site cations in the PVK absorber and organic charge transfer materials (spiro-OMeTAD, PCBM, and PEDOT:PSS). Therefore, defects in PVK, interface properties, and packaging techniques can all affect the thermal stability of PSCs.

Surface passivation of 3D PVK absorbers using 2D organic cations such as BA⁺, PA⁺, and PEA⁺ is an effective pathway to improve the efficiency of PVK photovoltaic devices; however, the stability of device against heat stress was poor [259]. Surface and interface passivation by molecules, including Lewis acids, Lewis bases, and Zwitterions, is widely used to improve the device stability and photovoltaic performance. The passivation effect could be attributed to the strong interaction of the chalcogenide-based groups such as -O-, -S-, and -SO₄ with Pb-related cation defects [295]. Huang *et al* [267, 296] investigated the chemical processes occurring within these devices during their operation and demonstrated that the deprotonation of organic cations such as

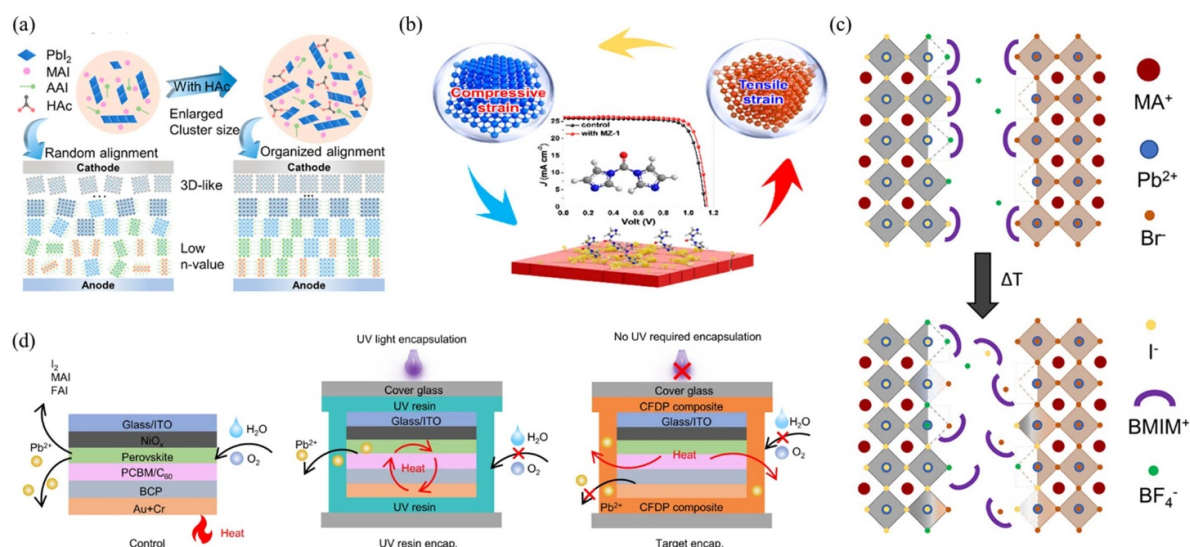


Figure 21. (a) Schematic of the 2D PVK film formation process using HAC. Reprinted with permission from [297]. Copyright (2023) American Chemical Society. (b) Illustrations of the tensile/compressive strains of PVK film and their effects. Reprinted with permission from [298]. Copyright (2023) American Chemical Society. (c) Proposed scheme of enhanced ion exchange for thermally induced halide mixing to form mixed-halide PVKs. The scheme shows the passivation of trap states at grain boundaries by BMIMBF₄. Reprinted with permission from [270]. Copyright (2023) American Chemical Society. (d) Scheme of the unencapsulated PSCs (left), PSCs with UV resin encapsulation (middle), and PSCs with CFDP encapsulation (right). Reproduced from [299]. CC BY 4.0.

PEA⁺ and BA⁺ in 2D PVKs primarily degrades the performance of solar cells operated at high temperatures. The HAC solvent [297] (figure 21(a)), which is a small molecule with an inorganic oxide dopant [275], can optimize the crystallization of low-dimensional PVKs and thus improve the thermal stability of devices.

In addition to surface defects of PVK, the buried interface properties of PSCs also affect their thermal stability. NiO_x has been widely used in IPSCs with superior thermal stability than n-i-p PSCs. However, due to cation deprotonation and iodide oxidation caused by Ni³⁺ sites, the device efficiency considerably degraded at high temperatures. By passivating the buried interface between NiO_x and PVK using fixed charge oxides such as SiO₂ and Al₂O₃, Yang *et al* [268] achieved IPSCs almost no efficiency loss after aging under 1-sun illumination at 85 °C for 2000 h in ambient air. The p-i-n PSCs containing additives with a high acid dissociation constant (pKa) maintained over 90% of their initial PCE after light soaking in an open circuit and 90 °C for 1500 h.

PVK is an absorbing material for PSCs, and its intrinsic properties are another key factor determining the thermal stability of the PSCs. Compressive strain in the PVK lattice increases the carrier lifetime and hole mobility and improves intrinsic stability [300]. Duan *et al* [298] designed an effective lattice-matching chelation strategy to modulate the strain of the crystal lattice of PVK films from tensile strain to compressive strain by anchoring bidentate imidazole (MZ-1) to the PVK lattice (figure 21(b)). The resulting PSC exhibited a dramatically improved efficiency of 24.61% and improved long-term thermal stability (60 °C, 500 h). ILs, such as BMIMBF₄, BMIMPF₆, have been widely used to prevent halide phase segregation and increase phase thermal stability. Gruninger *et al* investigated the mechanisms that changed halide

kinetics in mixed-halide PVK with an IL (figure 21(c)) and demonstrated that the presence of the IL increased the overall halide mixing rate, which was determined by the slowest halide migration rate [270].

Encapsulation engineering is another effective strategy to improve the thermal stability of PSCs. Wang *et al* [299] realized room-temperature nondestructive encapsulation by synthesizing a crosslinked fluoropropyl methylsiloxane-dimethylsiloxane multiblock polymer (CFDP) (figure 21(d)). The encapsulated CsMAFA PVK-based devices retained 98% of their initial PCE after 1000 h in the damp heat test (85 °C, 85% RH) and 95% of their initial PCE after 220 cycles in the thermal cycling test (−40 °C–85 °C).

6.4. Light soaking stability

Performance degradation of PSCs is usually caused by ion migration (metal and halide ions), carrier-driven phase segregation [301], and defect aggregation [302] under solar irradiation due to the photochemical activities of iodine-defects activated by their deep VB [261, 265]. In particularly, the iodine transport pathways from the PVK to the HTL layer can strongly influence light-induced halide segregation, ultimately determined by the HTL HOMO energy and halogen redox potentials [303] (figures 22(a) and (b)).

Strategies proposed for enhancing the PVK crystallinity and surface passivation effectively improved the device PCE but could not prevent light-induced instability. Low dimensional PVKs often have better stability, which helps to solve the photo-induced instability of PSCs. As shown in figure 22(c), the 2D mixed-halide PVK, PEA₂Pb-(I_{1-x}Br_x)₄, has superior phase photostability than its counterpart 3D

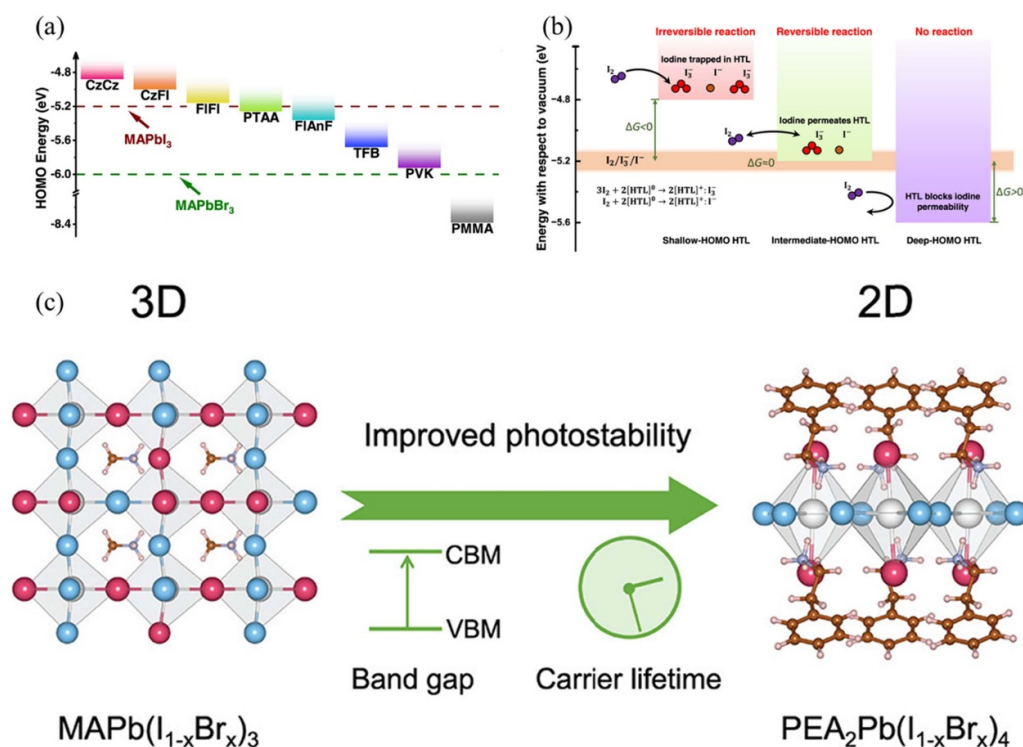


Figure 22. (a) HOMO energies of organic HTLs measured by UPS, where the VBM positions of PVKs are marked as dashed lines. (b) Schematic of reactions between I_2 and HTLs with different HOMO levels. (a), (b) Reprinted with permission from [303]. Copyright (2023) American Chemical Society. (c) Thermodynamic origin of the photostability of the 2D PVK $PEA_2Pb(I_{1-x}Br_x)_4$. Reproduced from [304]. CC BY 4.0.

PVK, $MAPb(I_{1-x}Br_x)_3$, under dark and illuminated conditions. Thermodynamic theory calculations showed that the enhanced phase stability was induced due to [304] (1) energetically favorable I–Br distribution, where I and Br anions were preferably located on different lattice sites; (2) the smaller band gap difference of the mixed parent phase and the nucleated low-band-gap phase, and (3) a much shorter photocarrier lifetime of 2D PVKs that reduced the driving force for phase segregation.

Residual lead iodide in PVK thin films is another source of photoinstability. Although a certain amount of residual PbI_2 improved photovoltaic performance, the device had poor light soaking stability. PbI_2 and I_0 are the photodegradation products of PbI_2 under light (threshold wavelength of 520 nm); these are deep-level defects, which could act as a carrier recombination center to exacerbate non-radiative recombination. Using a pre-embedding mixed A-cation halide (CsBr) strategy, Gao *et al* [305] successfully transformed the residual unstable PbI_2 near the buried interface into a more stable 3D PVK for improved light soaking stability.

6.5. Operational conditions

Halide diffusion from PVK into the HTL due to surface defects, particularly halide vacancies, during device operation limits its operational stability. Krishna achieved a T_{80} of

16 350 h using a rational molecular design strategy that passivated deleterious halide vacancies and suppressed defect-driven interfacial ion diffusion. The designed biphenyl-4,4'-dithiol passivator (figure 23(a)) passivated the defects in particular halide vacancies and led to the homogeneous work function on the PVK surface [306].

Similar to thermal stability, the volatile components and hygroscopic nature of dopants in the HTL cause morphological deformations that deteriorate the device efficiency and operational stability. To avoid heterogeneous doping composition and segregation microstructure, an implantation-assisted sequential doping (MISD) method (figure 23(b)) was developed for fabricating all evaporated HTLs, thereby eliminating postoxidation and light soaking [307]. The fabricated PSCs maintained 90% of their peak performance under continuous illumination for 3000 h. By simultaneously considering the hydrophobic property and iodine evaporation, Fang *et al* introduced b-cyclodextrin (b-CD) as an iodine trapper (figure 23(c)) and that the b-CD played a multifunctional in ensuring operational stability. (1) It bound with light-generated iodine (I_2) in PVK films and inhibited iodine escape under high temperatures. (2) These trapped I_2 also reacted with and consumed metallic Pb_0 defects and suppressed PVK degradation. Therefore, the device stability was markedly improved using ISOS-L-1 [maximum power point (MPP) tracking at 25 °C] and ISOS-L-2 (MPP tracking at 85 °C) [308].

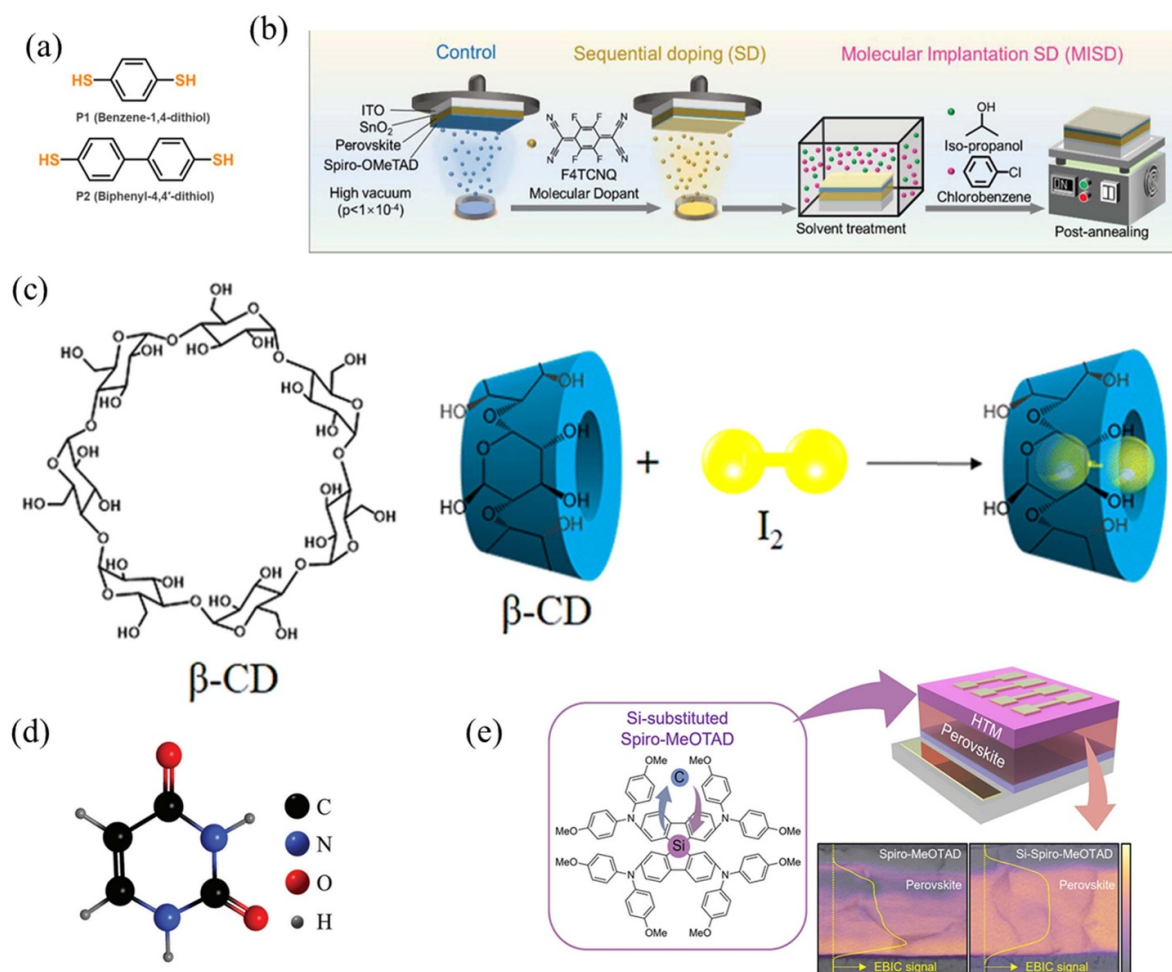


Figure 23. (a) Chemical structures of P1 and P2 molecules. Reprinted with permission from [306]. Copyright (2023) American Chemical Society. (b) Fabrication process of the HTL using different vacuum deposition techniques, including the control, SD, and MISD. [307] John Wiley & Sons. © 2023 Wiley-VCH GmbH. (c) Chemical structure of β -CD. Reproduced from [308] with permission from the Royal Society of Chemistry. (d) Structure of uracil. [266] John Wiley & Sons. © 2023 Wiley-VCH GmbH. (e) Si-substituted spirobifluorene hole-transporting material for PSCs. Reprinted with permission from [273]. Copyright (2023) American Chemical Society.

Buried-interface passivation is an effective approach for simultaneously improving device efficiency and stability. Wang *et al* [266] introduced uracil (figure 23(d)) into the SnO_2 and FAPbI_3 interface to passivate the defects, strengthen the grain boundaries, and increase the energy barrier from α - FAPbI_3 to δ - FAPbI_3 , thereby enhancing the stability of PVK films. The measurement of operational stability indicated that the device could maintain over 90% of its initial PCE after tracking for ~ 6000 h.

Designing a new type of HTM is another effective method to improve the operation stability of device. Luo *et al* synthesized Si-substituted spiro-MeOTAD by replacing the central carbon atom of spiro-MeOTAD with silicon atoms (figure 23(e)) [273]. The effective blocking Si-spiro HTMs have against metal ion migration due to strong intermolecular interactions, thereby enhancing the long-term operation stability of devices.

6.6. Radiation and mechanical stability

Solar panels are not only used on the earth's surface but also in the space; therefore, their radiation stability must be assessed. The radiation stability of $\text{Cs}_{0.04}\text{Rb}_{0.04}(\text{FA}_{0.65}\text{MA}_{0.35})_{0.92}\text{Pb}(\text{I}_{0.85}\text{Br}_{0.14}\text{Cl}_{0.01})_3$ PSCs was analyzed under extreme conditions of short-pulse (150 ns) 170 keV proton irradiation, which is equivalent to ~ 30 years at the low earth orbit. Results revealed its outstanding radiation stability along with slight degradation in its photovoltaic performance, which was mainly induced by proton irradiation and a considerable increase in the recombination losses resulting from bulk and surface traps [309].

Ensuring mechanical adhesion stability between the charge transfer layer and PVK thin films by reducing the trap density at the buried interface is also crucial for performance endurance. Bakr reported the successful growth of large-area

PVK single crystals on a hydrophilic HTL surface using SAM MeO–2PACz as the HTL. The as-fabricated single-crystal PSCs exhibited enhanced operational stability and PCEs of up to 23.1%. DFT modeling revealed that the enhanced mechanical adhesion stemmed from the stronger binding of MeO–2PACz extra functional groups (–MeO) to the PVK surfaces [177].

The formation and evolution of cracks in PVK films during thermal cycling affect their mechanical stability. Yuan *et al* [310] proposed a strain evolution strategy to inhibit cracks in PVK films by the *in situ* chemical crosslinking of TFEMA. This strategy can also be used to regulate the residual tensile strain into compression strain, thereby improving the device mechanical stability. The resulting device passes thermal-cycling qualification (IEC61215:2016, –40 °C–85 °C), retaining 95% of the initial PCE after 230 cycles. The strategies for increasing the grain boundary toughness coupled with the passivation of intragrain trap states can be an effective way to ultimately address the mechanical brittleness of the PVK polycrystalline films. By interacting with PVK via the bonding between O atoms and hydroxyl groups, ethyl cellulose (EC) was introduced as a ‘fiber-bridging’ component for interlinking the adjacent PVK halide octahedra. Using this approach, the Young’s modulus for three times, and hardness of the films [311].

6.7. Future perspectives

In summary, the stability of PSCs, PVK composition, device structure, maximum PCE, stability test conditions, and stability performance have undergone considerable advancements in 2023. The strategies adopted for these advancements are summarized in table 3. With considerable improvement in PSC stability, their commercialization is expected in the near future.

However, several issues have to be addressed to further improve the device stability, for which the following approaches have been proposed:

(1) Design new PVK materials

PVK structures can be stabilized by site cation doping in FAPbI₃ without losing the optimal bandgap for photovoltaic performance [321–323]. However, their intrinsic phase stability requires considerable improvement for meeting commercial requirements, which can be achieved by designing materials with high environmental resistance.

(2) Develop reliable encapsulation technology

Encapsulation is the best physical method to address this stability issue and enhance the lifetime of PSCs. However, due to the high chemical sensitivity of PVKs and organic materials in PSCs, the encapsulation materials and techniques need further improvement [278, 281].

(3) Unify stability assessment methods

Although the lifetime of PSCs has considerably improved, the reported stabilities in various studies cannot be accurately

compared due to the lack of unified evaluation criteria and uniform assessment method. Recently, ISOS protocols such as ISOS-S (dark storage), ISOS-L (light soaking), ISOS-O (outdoor), ISOS-T (thermal cycling), ISOS-LT (light–humidity–thermal cycling) have been used to assess the device stability (figure 24). In contrast, the outdoor lifetime of PSCs must also be predicted to accelerate their commercialization. However, the stability of PSCs can vary under cycled light, contrary to under constant illumination [324].

7. Lead toxicity and green solvents

Xi Jin^{1,2}, Pengfei Wu^{3,4}, Fei Zhang^{3,4} and Yan Jiang^{1,2}

¹ School of Materials Science and Engineering, Beijing Institute of Technology, Beijing 100081, People’s Republic of China

² Songshan Lake Materials Laboratory, Dongguan, Guangdong 523429, People’s Republic of China

³ School of Chemical Engineering and Technology, Tianjin University, Tianjin 300072, People’s Republic of China

⁴ Collaborative Innovation Center of Chemical Science and Engineering (Tianjin), Tianjin 300072, People’s Republic of China

7.1. Brief introduction

In the past decade, the PCE and stability of PSCs have considerably improved; thus, these devices will be commercialized in the near future [325]. However, state-of-the-art high-efficiency PSCs are manufactured using toxic materials such as lead in absorbers and harmful solvents in precursors. To prevent environmental issues and comply with environmental laws and regulations, it is imperative to ensure that PSCs are environmentally friendly and pollution-free throughout their life cycles [326, 327]. In this section, we discuss the main progress on reducing lead toxicity and using green solvents for PSCs.

7.2. Eco-friendly device processing

Solution processability is the unique advantage of PSCs compared to commercial PV technologies, as the manufacturing cost is considerably reduced [328, 329]. However, most precursor solvents such as DMF and antisolvents such as chlorobenzene (CB) are toxic and harmful to human health [321, 330]. Therefore, eco-friendly solvents must be developed for the commercialization of PSCs.

Biomass-derived green solvents with γ -valerolactone (GVL) and n-butyl acetate were prepared by Miao *et al* [331] (figure 25(a)) surprisingly, due to the high-valence $[\text{PbI}_x]^{2-x}$ complexes and the strong interaction between GVL and FA^+ , the FAPbI₃ PVK ink was stable up to one year. Minimodules with an aperture area of 12.25 cm² were fabricated using this green solvent approach, which achieved a certified efficiency of 20.23%. Thus, this method paved the path for the practical application of PSCs. Water is the most available and environmentally friendly solvent. $\text{Pb}(\text{NO}_3)_2/\text{H}_2\text{O}$ systems

Table 3. Summary of the device stability research progress.

PVK composition	Structure	Max PCE	Condition	Stability	Strategy	References
$\text{Rb}_{0.05}\text{Cs}_{0.05}\text{MA}_{0.05}\text{FA}_{0.85}\text{Pb}(\text{I}_{0.95}\text{Br}_{0.05})_3$	p-i-n	25.5%	25 °C–85 °C; white light-emitting diode at 1.2 sun; and 85% RH	<8% degradation after approximately 2560 h; >1000 h at 85 °C	Improving the ion-blocking properties of the self-SAM HTL	[81]
$\text{FA}_{0.85}\text{Cs}_{0.15}\text{Pb}(\text{I}_{0.95}\text{Br}_{0.05})_3$	p-i-n	22.26%	75 °C; 1 sun-equivalent white-light LED	93% of the initial efficiency of the device retained after continuous operation for 1000 h	Modulation of PVK decomposition with a robust $\text{Bi}/\text{Al}_2\text{O}_3/\text{parylene}$ multilayer barrier	[312]
CsMAFAPbI_3	p-i-n	21.91%	55 ± 5 °C; AM 1.5 illumination; and in the air.	The encapsulated device retained 81% of its original PCE after 1000 h	Synthesized a crosslinked fluoropropyl methylsiloxane–dimethylsiloxane multiblock polymer (CFDP) with good thermal stability	[299]
$\text{FA}_{0.9}\text{Cs}_{0.1}\text{PbI}_3$	p-i-n	24.1%	85 °C; simulated AM 1.5G illumination; and in an N_2 atmosphere	Maintained 90% of the initial efficiency after ~1500 h	Ammonium cation, PEAMA ⁺ , with a high acid dissociation constant (pK_{a})	[267]
$\text{FA}_{0.79}\text{MA}_{0.16}\text{Cs}_{0.05}\text{PbI}_3$	p-i-n	22.5%	85 °C; 1-sun illumination; and 50% RH	The device showed superior stability with almost no efficiency loss after MPP tracking at 85 °C for 2000 h	The ‘physical’ passivation method by producing AlO_x interlayers grown by ALD at the PVK/charge extraction layer heterojunction	[268]
$\text{Cs}_{0.05}(\text{MA}_{0.17}\text{FA}_{0.83})_{0.95}\text{Pb}(\text{I}_{0.83}\text{Br}_{0.17})_3$	p-i-n	19.12%	UVO: ultraviolet photons in the wavelength range of 200 nm	The devices retained their initial PCEs of 17.0% after 20 min of exposure	A silicon oxide barrier layer	[313]
$(\text{AA})_2\text{MA}_4\text{Pb}_5\text{I}_{16}$	p-i-n	18.55%	30 °C–40 °C; LED illumination (AM 1.5G, 100 mW cm^{-2}); and under a N_2 environment.	The device decayed slowly and maintained 80% of its initial PCE after 400 h	Introduced $\text{CH}_3\text{COOH}(\text{HAc})$ as a cosolvent	[297]
FAPbI_3	n-i-p	21.42%	70 °C; in the dark; and N_2 environment.	The devices had 2% efficiency loss at 70 °C	Developed a strategy of doping m-MTDATA HTLs with MoO_3	[275]
$(\text{FAPbI}_3)_x(\text{MAPbBr}_3)_{1-x}$	n-i-p	22.5%	At ambient temperature; under 1-sun illumination; and in an Ar atmosphere	The PSC retained 92.9% of its initial PCE after continuous light illumination for 120 h	The center carbon of Spiro-MeOTAD was substituted with a Si atom	[273]
$\text{CsPbI}_{3-x}\text{Br}_x$	n-i-p	20.59%	25 °C; Newport solar simulator (94 043 A) with an AM 1.5G spectrum, light intensity: 100 mW cm^{-2} ; and 25% RH	When the devices were aged for 3055 h, the optimized PSCs retained 91% of their initial PCE	A TrMAPbX_3 ($\text{X} = \text{Br}$ and I) PVK with a linearly rotatable skeleton was synthesized	[302]

(Continued.)

0.97(FAPbI ₃) 0.03(MAPbBr ₃)	n-i-p	23.22%	28 °C; under AM 1.5G 1-sun (100 mW cm ⁻²) illumination; and 30% RH.	The device maintained 87% of its initial PCE after 2000 h	An efficient passivation material (K2-PDT) was developed	[314]
Cs _{0.05} FA _{0.95} PbI ₃	p-i-n	24.29%	Room temperature; 1-sun illumination; and an inert atmosphere	The device maintained 75% of its initial PCE for up to 450 h (thermal stress and operational stability)	Compositional engineering using a single Cs-doped crystal	[178]
FA _{0.9} Cs _{0.1} PbI _{2.8} Br _{0.2}	n-i-p	23.17%	100 mW cm ⁻² , white LED and N ₂ atmosphere	Devices maintained 89.7% of their initial PCEs	Molecular engineering of nanographene-based HTMs and interface modifiers	[315]
CsPbI _{1.5} Br _{1.5}	p-i-n	4.25%	At room temperature; under AM 1.5G light; and in an ambient atmosphere	CsPbI _{1.5} Br _{1.5} retained approximately 90% PCE under 1 sun AM 1.5G illumination for 12 h	Polyvinylpyrrolidone (PVP) polymer-assisted <i>in situ</i> crystallization	[316]
Cs _{0.09} FA _{0.91} PbI ₃	n-i-p	20.26%	75 °C; 1 sun-equivalent illumination; and nitrogen environment	PSCs retained >80% of their original PCE after an operando stability test at 200 h and 75 °C	Infiltration of TiO _x via vapor-phase infiltration (VPI)	[280]
(FA _{0.833} MA _{0.17}) _{0.95} Cs _{0.05} Pb(I _{0.833} Br _{0.17}) ₃	p-i-n	20.67%	1-sun illumination and 40%–50% RH	The unencapsulated device retained 95% of PCE after 3000 h	A mixing engineering strategy that combined Me-4PACz SAM with conjugated polyelectrolyte PFN-Br	[272]
(FAPbI ₃) _{0.97} (MAPbBr ₃) _{0.03}	n-i-p	24.0%	40 °C; continuous 1-sun illumination; and in N ₂ environment.	Device retained 88% of its initial PCE after 2000 h at 40 °C and 1-sun illumination	Bifunctional aromatic ligands	[306]
CsPb _{0.6} Sn _{0.4} I ₃	p-i-n	16.79%	1 sun illumination (100 mW cm ⁻²) and in an N ₂ -filled glovebox	The device retained 90% retention of its initial PCE after 958 h under continuous illumination	A surface Sn (IV) hydrolysis (SSH) method	[264]
Sn PVK	p-i-n	12.1%	In dark and an N ₂ atmosphere	After dark storage measurements (~2800 h), the PCE increased from 6.4% to 7.5%	Surface modification of PEDOT:PSS with aromatic diammonium acetate	[150]
CsCl-FAPbI ₃	n-i-p	23.20%	25 °C and under 45%–65% RH	The device maintained 60% of its initial PCE after 1056 h	Residual chlorides were eliminated by post-heat treatment (PHT)	[317]

(Continued.)

Table 3. (Continued.)

PVK composition	Structure	Max PCE	Condition	Stability	Strategy	References
$\text{FA}_{0.6}\text{MA}_{0.4}\text{PbI}_3$	p-i-n	23.1%	1-sun (AM 1.5G) illumination and in a nitrogen-filled glovebox	The SC-PSC lost approximately 25% of its initial PCE after ~730 h of MPPT	Hydrophilic SAM MeO-2PACz HTL	[177]
$(\text{Cs}_{0.05}\text{FA}_{0.80}\text{MA}_{0.15})\text{Pb}(\text{I}_{0.95}\text{Br}_{0.05})_3$; FAPbI_3	n-i-p	23.50% and 24.61%	1 sun illumination	PCE stabilized at 23.63% initially and then decreased to 23.23% after 300 s at a constant potential and maximum power	The organic salt of bidentate imidazole	[298]
$\text{Cs}_{0.05}\text{MA}_{0.85}\text{FA}_{0.10}\text{Pb}(\text{I}_{0.97}\text{Br}_{0.03})_3$	n-i-p	22.92%	At room temperature; 100 mW cm^{-2} simulated AM 1.5G irradiation; and 65 \pm 5% RH	Approximately 88% of initial PCE was retained after aging 2900 h	A spontaneous internal encapsulation strategy by constructing a dual interfacial PVK heterojunction at the top and buried interfaces of the 3D PVK film	[318]
$\text{FA}_{0.9}\text{MA}_{0.03}\text{Cs}_{0.07}\text{PbI}_{2.76}\text{Br}_{0.24}$	n-i-p	22.3%	AM 1.5G illumination and in ambient conditions with 30% RH	Retained >90% of the initial PCE after 5200 h	A molecular implantation-assisted sequential doping (MISD) approach	[307]
$\text{FAMACsPb}(\text{ICl})_3$	n-i-p	24.23%	40 $^{\circ}\text{C}$ –50 $^{\circ}\text{C}$; an LED array with an intensity of 100 mW cm^{-2} ; and in a box with continuous N_2 flow	Maintained >90% of its initial PCE after tracking at its MPP for ~6000 h	Introduced uracil as a bifunctional additive into PVK films	[266]
$\text{FA}_{0.95}\text{Cs}_{0.05}\text{PbI}_3$	p-i-n	23.91%	White LED illumination (100 mW cm^{-2}) and in a nitrogen atmosphere	The devices maintained >93% of their initial PCEs after 1680 h of MPP tracking	<i>In situ</i> chemical crosslinking of the polymer TFEMA	[310]
$\text{FAPb}_x\text{Sn}_{1-x}\text{I}_3$	p-i-n	23.7%	50 \pm 5 $^{\circ}\text{C}$; 1-sun illumination; and in air	Retained 88% of its initial PCE for 1000 h	Tailored octylammonium tetrafluoroborate (OABF_4) additive	[319]
$\text{Rb}_{0.05}\text{Cs}_{0.05}(\text{FA}_{0.83}\text{MA}_{0.17})_{0.95}\text{Pb}(\text{I}_{0.83}\text{Br}_{0.17})_3$	n-i-p	21.95%	Room temperature; 1-sun illumination; and N_2 atmosphere	Almost no degradation after >1000 h of MPP tracking	Functionalized 2D titanium carbide (Ti_3C_2) MXene	[274]
$\text{MAPb}(\text{I}_{1-x}\text{Br}_x)_3$	p-i-n	21.23%	85 $^{\circ}\text{C}$ and in a nitrogen atmosphere	80% of the initial PCE was reached after >3500 h	A simplified dual-source vacuum deposition method	[320]
$\text{Cs}_{0.05}\text{MA}_{0.15}\text{FA}_{0.8}\text{Pb}(\text{I}_{0.75}\text{Br}_{0.25})_3$	n-i-p	24.12%	20 $^{\circ}\text{C}$ and in dry air (RH: 10%–20%)	The devices maintained >90% of their initial PCE after 8000 h	A uniform polymer internal package layer constructed using thermally triggered cross-linkable monomers	[279]

(Continued.)

$\text{Cs}_{0.05}(\text{MA}_{0.17}\text{FA}_{0.83})_{0.95}\text{Pb}(\text{I}_{0.83}\text{Br}_{0.17})_3$	p-i-n	15.26%	20 °C and 40% RH	Maintained 75% of the initial PCE after 600 h	Evaluated the effectiveness of oxygen, sulfur, and selenium-based interface passivator molecules [295]
$(\text{CsPbI}_3)_{0.05}[(\text{FAPbI}_3)_{0.90}(\text{MAPbBr}_3)_{0.10}]_{0.95}$	p-i-n	20.64%	In ambient environment with 45% RH	Retained 80% of its PCE after 350 h	The use of polyoxometalate complex $[(\text{C}_8\text{H}_{17})_4\text{N}]_4[\text{SiW}_{12}\text{O}_{40}]$ (TOASiW ₁₂) as the cathode layer [277]
$\text{FA}_{0.95}\text{Cs}_{0.05}\text{PbI}_3$	p-i-n	24.5%	40 °C; 1-sun illumination and in N ₂ atmosphere	Initial PCE of ~23% and stabilized at ~23.5% for >3500 h	Lewis base diphosphine molecule of 1,3-bis(diphenylphosphino)propane (DPPP) [294]
MAPbI_3	p-i-n	20.55%	Ambient air and 30% relative humidity	After 1900 h, the device maintained 89% of its initial PCE	By incorporating a natural ID material, ethyl cellulose (EC), within the PVK films [311]
PVK–PbI ₂ heterojunction	n-i-p	24.23%	65 °C; continuous AM 1.5G illumination (100 mW cm ⁻²); and N ₂ atmosphere	No obvious PCE degradation after illumination aging for 200 h	A high-quality PVK–PbI ₂ heterojunction film was constructed [265]
$\text{FA}_x\text{MA}_{1-x}\text{PbI}_3$	n-i-p	18.76%	30 °C and 80% relative humidity.	The PSCs maintained 95% of their initial efficiency after 2400 h	An organic–inorganic hybrid material ($\text{Al}_x\text{O}_y\text{C}_z$) was grown by plasma-enhanced MLD (PEMLD) [281]
$\text{FA}_x\text{Cs}_{1-x}\text{PbI}_3$	n-i-p	24.26%	25 ± 5 °C and under 1-sun illumination;	Maintained 94.7% of their initial efficiencies after operating for 1000 h	A pre-embedding mixed A-cation halide strategy [305]
FAPbI_3	n-i-p	24.7%	85 °C and AM 1.5G conditions	After 500 h of aging, the cells exhibited an average PCE retention rate of 92%	SBF-FC hole-transporting material, with a high glass-transition temperature [276]
$\text{Cs}_{0.05}\text{FA}_{0.95}\text{PbI}_3$	p-i-n	23.2%	25 °C; ISOS-L-1; and in the N ₂ glovebox	PSCs retained 91.8% of the highest efficiency after MPP tracking for 1000 h	By introducing β-cyclodextrin (β-CD) iodine trapping agent [308]
FAPbI_3	n-i-p	25.0%	85 °C; under N ₂ ; and 60 ± 10% relative humidity	Retained >92% of their initial efficiency for 1000 h	Introduced alkylammonium formates (AAFs) [260]
$\text{HA}_2\text{PbI}_2\text{Br}_2$ passivated FACsPbI_3 PVK	n-i-p	24.29%	1-sun illumination and a nitrogen atmosphere	Retained ~93% of its initial PCE after 1000 h	Developed $\text{HA}_2\text{PbI}_2\text{Br}_2$ -passivated FAC-based PVK [259]

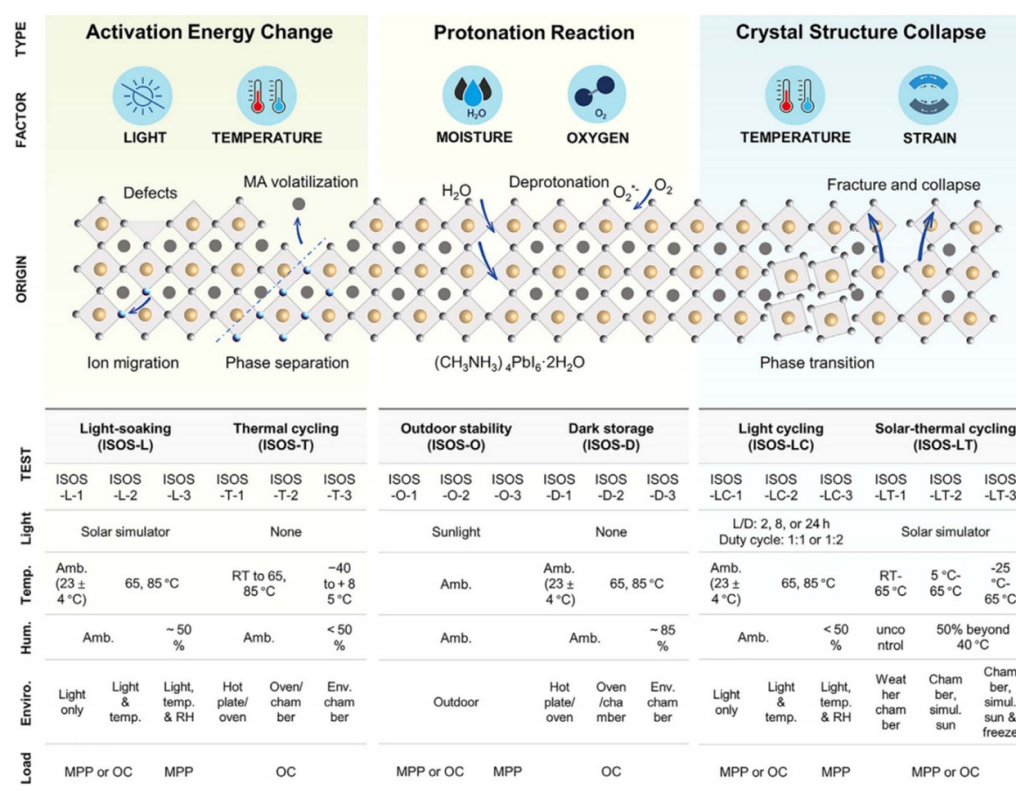


Figure 24. Schematic of PVK material degradation and overview of ISOS protocols for the properties of PVK materials and devices. Reprinted from [294], © 2023 Published by Elsevier Inc.

were explored for fabricating PSCs; however, they suffered from the incomplete conversion of Pb(NO₃)₂ to PVK [332]. Zhai *et al* [332] introduced a method to produce high-quality PSCs by modulating the formation kinetics of PVK using halide-free aqueous nanofluids (NFs; figure 25(b)). PSCs fabricated from PbCO₃ NFs exhibited an average PCE of 23.64% under dry air conditions and showed excellent stability under continuous light exposure. Later, the team investigated the crystallization of Pb(NO₃)₂ at different RHs [333]. Moisture in ambient air played a key role in the rate of nucleation of Pb(NO₃)₂ (figure 25(c)). They used potassium oleate to reduce the surface tension of water under dry air conditions and easily obtained high-quality, pinhole-free conformal PVK films with a PCE of 24.14%.

To address the toxicity issues with the widespread use of CB, environmentally friendly and more efficient antisolvents must be identified. Zhang *et al* [334] developed a green antisolvent, i.e. diethyl carbonate, which is not only environmentally friendly but also more suitable for preparing Sn-based PVKs. It decelerated the crystallization of FASnI₃, enabling preferred crystal orientation and less high-dimensional extended defects. Xiu *et al* [335] investigated a method by employing CsPbI₃ NCs functionalized green alkanes with ultralow polarity (alkane/NC) as antisolvents to fabricate high-quality PVKs. The alkane/NC method effectively solved the discontinuous film issue by providing sufficient heterogeneous nuclei and successfully suppressed phase segregation, which easily

occurred in CB-processed PVK films. PSCs using octane (OCT)/NCs showed an improved PCE from 21.59% for CB to 23.10%. Toxic solvents were commonly used in the preparation of charge transport layer in PSCs. To address this issue, Yu *et al* [336] treated an HTL (BTP1-2) with a green solvent, 2-methylanisole (2MA). This solvent enabled them to prepare IPSCs with an impressive PCE of 24.34%.

7.3. Mitigation of lead leakage during device operation

A comprehensive analysis of Pb toxicity in PVK photovoltaics indicates that the high lead dosage from lead-based devices cannot be ignored [337]. As the PCEs of lead-based PSCs have reached impressive levels, Pb leakage should be avoided on priority in addition to enhancing the operational lifetimes for the development of lead-based PSCs toward real-world applications. Various strategies have been proposed to reduce lead leakage without sacrificing device performance [338–341], such as introducing isolation or absorption layers and additives with suitable properties, including high lead adsorption, low aqueous solubility, acid/alkali resistance, and low cost [342–344]. Among them, polymer-based Pb-adsorbing layers and additives are widely used owing to their low cost and superior performance. By offering notable examples of preventing lead leakage, these methods pave the way for accelerating PVK photovoltaic technology toward sustainability, eco-friendliness, and industrialization.

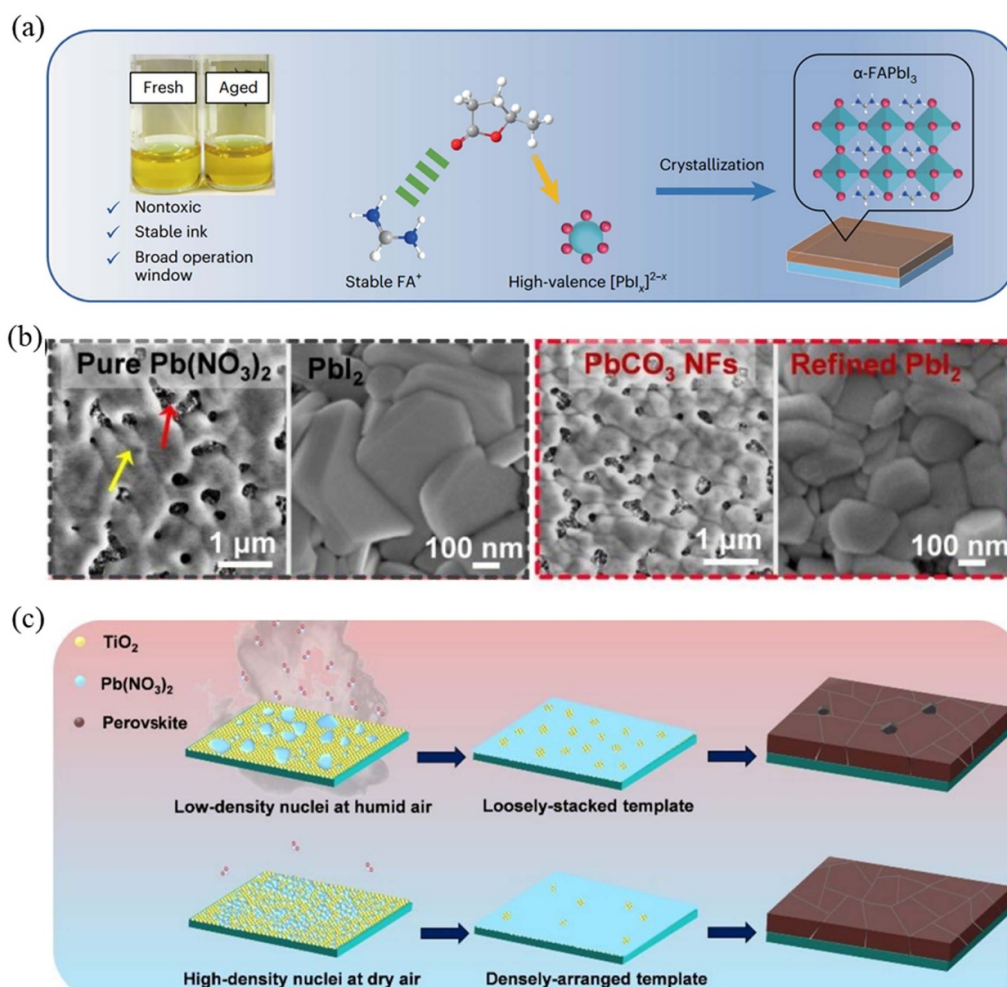


Figure 25. (a) Advantages of using GVL-based PVK precursor solution. Reproduced from [331], with permission from Springer Nature. (b) Pb(NO₃)₂ and PbI₂ films were prepared from pure Pb(NO₃)₂ solution and PbCO₃ NFs, respectively. Red and yellow arrows indicate mp-TiO₂ substrates and Pb(NO₃)₂ films, respectively. Reproduced from [332] with permission from the Royal Society of Chemistry. (c) Schematic of crystallization under different relative humidity. Reproduced from [333] with permission from the Royal Society of Chemistry.

A titanium dioxide (TiO₂) sponge was fabricated by Valastro *et al* [345], which proved to be an effective strategy for capture Pb leaked from damaged PSCs (figure 26(a)). TiO₂ was highly transparent and could be fabricated at room temperature. Taking the advantage of its mesoporous structure, Pb ions could be firmly fixed on the inner surfaces of the TiO₂ sponge, which yielded a considerable Pb sequestration efficiency (SQE) of 90.2% (figure 26(b)). More importantly, the TiO₂ sponge could be deposited via a solvent-free sputtering process, reducing environmental impacts and benefiting large-scale device production. Inspired by the prey behavior of spiders, Luo *et al* [346] introduced the 'mesoporous amino-grafted-carbon net (BCT)' on the glass substrate, which combined ethylenediamine and mesoporous matrices to capture Pb leaked from the broken device via chemical chelation and physical adsorption (figure 26(c)). Thus, the device with BCT (BG-PSC) exhibited a Pb SQE of >90%, regardless of acidic conditions and the use of DI water. This value was considerably higher than that of unencapsulated devices

(U-PSC) and devices covered with pure glass (G-PSC). Moreover, the device with BCT broken by hail in the Yellow River water had a much lower Pb leakage rate (only 8.4%) than the device with glass encapsulation (61.36%), verifying the superior Pb adsorption performance of BCT in complex environments (figure 26(d)). In addition to the polymer with a porous network, the supramolecule is a promising candidate for restraining Pb leakage. Yang *et al* [347] successfully embedded a crosslinking supramolecular complex (HP β CD–BTCA) into PVK films, which could effectively suppress the nonradiative recombination and facilitate the photo-induced separation of carriers (figure 26(e)). The built-in self-crosslinking of HP β CD–BTCA only released <14 ppb of Pb ions after 522 h of dynamic water scouring (figure 26(f)), complying with the standards of the US Environmental Protection Agency (15 ppb).

In addition to reducing Pb toxicity, PbI₂ can be further separated and recycled from end-to-life devices with HP β CD–BTCA modification. The device using recycled PbI₂ exhibited

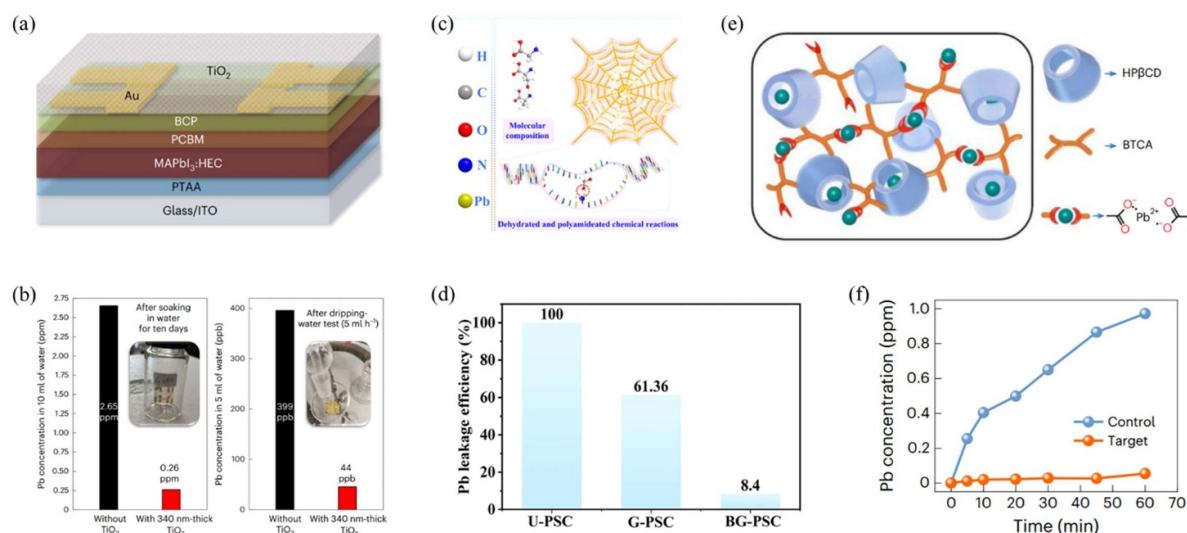


Figure 26. (a) Architecture of a semitransparent device with the TiO₂ layer. (b) Pb concentration of PSCs with and without TiO₂ (left) for 10 d in 10 ml of water. (a), (b) Reproduced from [345], with permission from Springer Nature. (c) Hunting mechanism of spider web from molecular composition to overall structure. (d) Pb SQEs of the damaged U-PSC, G-PSC, and BG-PSC in the Yellow River water. (c), (d) Reproduced from [346]. CC BY 4.0. (e) Schematic of lead capturing by crosslinking HPβCD-BTCA supramolecular complex. (f) Comparison of Pb sequestration for the damaged PSCs with or without HPβCD-BTCA. (e), (f) Reproduced from [347], with permission from Springer Nature.

a PCE of ~20%, demonstrating favorable cost-effectiveness and environmental soundness. Similarly, Zhang *et al* [348] designed and synthesized an additive for PVK precursors based on an *in situ* thermal crosslinking polymer, POF-HDDA. The device with POF-HDDA exhibited almost no drop in device performance after 1050 h of storage in ambient conditions and maintained 90% of its initial PCE after 4300 h of storage. Besides the enhanced environmental resistance, the Pb leakage inhibition rate was up to 85% due to the coordination interaction between Pb²⁺ and C=O in POF-HDDA. These polymer additives with multifunctional groups can inhibit Pb leakage in rigid PSCs and reduce Pb release from FPSCs into the environment. Xu *et al* [349] reported a polymer additive (PPG-mUPy-APDS) for enhancing the air stability and device flexibility of PSCs. The polymer, aggregated at grain boundaries and film surface, could block the immobilization of the Pb ions via chemically bonding with the -COOH groups.

7.4. Summary

Environmental sustainability is an essential criterion for developing PSCs. From the device fabrication viewpoint, further research effort is expected to explore advanced environmentally friendly solvents with high precursor solubility and superior substrate wettability that allow conformal coating of PVK and other functional layers in devices. From the device operation viewpoint, further investigation is anticipated to conceive more integral encapsulations with enhanced moisture, chemical, and lead resistance; perchance; and detoxification capacity using a combination of internal and external protection methodologies.

8. Future perspectives

In summary, the key progress of PSCs in 2023 was comprehensively summarized in six classifications: regular n-i-p PSCs, inverted p-i-n PSCs, PVK-based TSCs, PSMs, device stability, and lead toxicity and green solvents. Here, to gain a deeper understanding of the current research trends in PSC and provide guidance for future research in this field, we classify and prospect future research based on the research progress in 2023.

- (1) Regular n-i-p PSCs: Attributed to great efforts in crystal regulation of PVK, optimization of charge transport layer, and improvement of interface properties, the regular n-i-p PSCs achieved PCE of certified 25.8% in 2023. To further improve the photovoltaic performance of the regular n-i-p PSCs, the following measures may be adopted in future research. First, preparing high-quality FAPbI₃ PVKs with a wider absorption range through appropriate crystal growth control strategies is a key method to further improve PCE of regular n-i-p PSCs. Second, based on the structural characteristics of the materials, developing new passivating agents that are more suitable for passivating FAPbI₃ is another way to further refresh the PCE of regular n-i-p PSCs. Third, given the hygroscopicity and high cost of spiro-OMeTAD, it is necessary to develop new types of hole transport materials.
- (2) Inverted p-i-n PSCs: Owing to its unique advantages, IPSCs have attracted extensive attention in 2023. Thanks to the optimization of the charge transport layer, improvement of interface properties, and in-depth understanding of PVK crystal regulation, the highest certified PCE

of IPSCs was continuously refreshed to 25.8% in 2023. Although significant progress has been made in IPSCs over the past year, there are still some issues that need to be addressed. First, Similar to regular n-i-p PSCs, preparing high-quality MA-free and Br-free FAPbI₃ PVK through appropriate crystal growth control strategies is equally important for further refreshing the PCE of IPSCs. Second, another research focus next year will be on the design of new hole transport materials. For example, the interface mechanism of SAM molecules, which are widely used in high-efficiency IPSCs, still needs further research, including interface carrier dynamics, interactions with PVKs, and SAM stacking modes. In addition, the development of novel characterization techniques is of great significance for studying the properties of buried interfaces and further designing novel SAM molecules. Third, given the different properties from regular n-i-p PSCs, developing more suitable PVK surface passivation agents for IPSCs is crucial for further improving device efficiency.

- (3) PVK-based TSCs: The progresses in charge transporting materials, interconnecting layers, and preparation techniques of the subcells have greatly enhanced the PCE of PVK-based TSCs. Currently, the PCE of PVK-based TSCs is still much lower than the theoretical limit. Developing low-loss interconnecting layers and improving the performance of subcells would further improve the PCE of PVK-based TSCs.
- (4) PSMs: The diminishing disparity in PCE between large and small area devices suggests significant commercial promise for PSMs. However, to realize the commercialization of PSMs, several key challenges must be addressed, including the advancement of technologies for scalable fabrication, the formulation of PVK precursor inks conducive to depositing high-quality films over large areas, and the implementation of environmentally friendly and cost-effective preparation methods. Currently, there are many scientists and engineers constantly improving the PCE of PSMs, and more technological breakthroughs are expected in the future.
- (5) Device stability: Significant advancements in the stability of PSCs have paved the way for their anticipated commercialization in the near future. However, several issues have to be addressed to further improve the device stability, for which the following approaches have been proposed. First, more inherently stable PVK materials should be designed to meet commercial requirements, such as site cation doping in FAPbI₃ without losing the optimal bandgap. Second, the development of reliable encapsulation materials and technologies is crucial to protect sensitive PVK and organic materials in PSCs. Third, further unification of stability assessment methods under different stress conditions, such as ISOS-S (dark storage), ISOS-L (light soaking), ISOS-O (outdoor), ISOS-T (thermal cycling), ISOS-LT (light-humidity-thermal cycling), especially outdoor conditions, is essential to accelerate their commercialization process.
- (6) Lead toxicity and green solvents: Environmental sustainability is a crucial factor in the development of PSCs.

Future research endeavors should focus on investigating advanced environmentally friendly solvents with high precursor solubility and superior substrate wettability to enable the conformal coating of PVK and other functional layers in PSC devices. Additionally, further exploration is needed to develop more comprehensive encapsulation methods that offer improved resistance to moisture, chemicals, and lead, as well as enhanced detoxification capabilities through a combination of internal and external protective measures.

Acknowledgments

This work was financially supported by the National Natural Science Foundation of China (Nos. 22075221, 22379045, 62104170, 52102219, 52002140, U20A20252, 52102149, 52203237 and 22279083), Guangdong Basic and Applied Basic Research Foundation for Distinguished Young Scholar (No. 2021B1515020028), open research fund of Songshan Lake Materials Laboratory (No. 2021SLABFN17), Guangdong Provincial Key Laboratory of New and Renewable Energy Research and Development (No. E239kf0901), TCL Young Scholars Program, Natural Science Foundation of Shanghai (21ZR1404900), Ministry of Science and Technology of China (2021YFB3800104), Young Elite Scientists Sponsorship Program by CAST, Self-determined and Innovative Research Funds of HUST (2020kfyXJJS008), Natural Science Foundation of Hubei Province (2022CFA093), Innovation Project of Optics Valley Laboratory (Grant No. OVL2021BG008), Natural Science Foundation of Xinjiang (Grant No. 2022D01D79) and Guangdong Basic and Applied Basic Research Foundation (Grant No. 2022B1515120006).

ORCID iDs

Jianfeng Lu  <https://orcid.org/0000-0001-5586-4656>
 Qifan Xue  <https://orcid.org/0000-0003-0013-0721>
 Jia Liang  <https://orcid.org/0000-0002-4352-1581>
 Liming Ding  <https://orcid.org/0000-0001-6437-9150>
 Yan Jiang  <https://orcid.org/0000-0001-7665-1174>
 Wei Chen  <https://orcid.org/0000-0002-2418-9210>

References

- [1] Shi P *et al* 2023 Oriented nucleation in formamidinium perovskite for photovoltaics *Nature* **620** 323–7
- [2] Luo C, Zheng G, Gao F, Wang X, Zhan C, Gao X and Zhao Q 2023 Engineering the buried interface in perovskite solar cells via lattice-matched electron transport layer *Nat. Photon.* **17** 856–64
- [3] Park J, Kim J, Yun H S, Paik M J, Noh E, Mun H J, Kim M G, Shin T J and Seok S I 2023 Controlled growth of perovskite layers with volatile alkylammonium chlorides *Nature* **616** 724–30
- [4] Yan L *et al* 2023 Fabrication of perovskite solar cells in ambient air by blocking perovskite hydration with guanabenz acetate salt *Nat. Energy* **8** 1158–67

- [5] Huang Z *et al* 2023 Anion- π interactions suppress phase impurities in FAPbI₃ solar cells *Nature* **623** 531–7
- [6] Chen Y, Wang Q, Yao Y, Yang J, Tang W, Qiu W, Wu Y and Peng Q 2023 Synergistic transition metal ion co-doping and multiple functional additive passivation for realizing 25.30% efficiency perovskite solar cells *Energy Environ. Sci.* **16** 5243–54
- [7] Wang Y, Feng M, Chen H, Ren M, Wang H, Miao Y, Chen Y and Zhao Y 2023 Highly crystallized Cl-doped SnO₂ nanocrystals for stable aqueous dispersion toward high-performance perovskite photovoltaics *Adv. Mater.* **36** 2305849
- [8] Guo H, Xiang W, Fang Y, Li J and Lin Y 2023 Molecular bridge on buried interface for efficient and stable perovskite solar cells *Angew. Chem., Int. Ed.* **62** e202304568
- [9] Xu R *et al* 2023 Optimizing the buried interface in flexible perovskite solar cells to achieve over 24% efficiency and long-term stability *Adv. Mater.* **36** 2308039
- [10] Sheng W, He J, Yang J, Cai Q, Xiao S, Zhong Y, Tan L and Chen Y 2023 Multifunctional metal-organic frameworks capsules modulate reactivity of lead iodide toward efficient perovskite solar cells with UV resistance *Adv. Mater.* **35** 2301852
- [11] NREL *Best Research-Cell Efficiency Chart* (available at: <https://www.nrel.gov/pv/cell-efficiency.html>)
- [12] Yang L *et al* 2023 25.24%-efficiency FACsPbI₃ perovskite solar cells enabled by intermolecular esterification reaction of dl-carnitine hydrochloride *Adv. Mater.* **35** 2211545
- [13] Sun X, Li D, Zhao L, Zhang Y, Hu Q, Russell T P, Liu F, Wei J and Li H 2023 (111)-dominated perovskite films by antisolvent engineering *Adv. Mater.* **35** 2301115
- [14] Li M *et al* 2023 Orientated crystallization of FA-based perovskite via hydrogen-bonded polymer network for efficient and stable solar cells *Nat. Commun.* **14** 573
- [15] Meng Y *et al* 2023 Epitaxial growth of α -FAPbI₃ at a well-matched heterointerface for efficient perovskite solar cells and solar modules *Adv. Mater.* **36** 2309208
- [16] Ge Y, Wang H, Wang C, Guan H, Shao W, Wang T, Ke W, Tao C and Fang G 2023 Intermediate phase engineering with 2,2-azodi(2-methylbutyronitrile) for efficient and stable perovskite solar cells *Adv. Mater.* **35** 2210186
- [17] Yue W, Yang H, Cai H, Xiong Y, Zhou T, Liu Y, Zhao J, Huang F, Cheng Y-B and Zhong J 2023 Printable high-efficiency and stable FAPbBr₃ perovskite solar cells for multifunctional building-integrated photovoltaics *Adv. Mater.* **35** 2301548
- [18] Zhao C *et al* 2023 Stabilization of FAPbI₃ with multifunctional alkali-functionalized polymer *Adv. Mater.* **35** 2211619
- [19] Hu Y *et al* 2024 Seed-mediated growth for high-efficiency perovskite solar cells: the important role of seed surface *Angew. Chem., Int. Ed.* **63** e202316154
- [20] Yang T *et al* 2023 Amidino-based Dion-Jacobson 2D perovskite for efficient and stable 2D/3D heterostructure perovskite solar cells *Joule* **7** 574–86
- [21] Rui Y, Jin Z, Fan X, Li W, Li B, Li T, Wang Y, Wang L and Liang J 2022 Defect passivation and electrical conductivity enhancement in perovskite solar cells using functionalized graphene quantum dots *Mater. Futures* **1** 045101
- [22] You S *et al* 2023 Bifunctional hole-shuttle molecule for improved interfacial energy level alignment and defect passivation in perovskite solar cells *Nat. Energy* **8** 515–25
- [23] Alharbi E A *et al* 2023 Cooperative passivation of perovskite solar cells by alkyltrimethylammonium halide amphiphiles *Joule* **7** 183–200
- [24] Wu J, Li M-H, Fan J-T, Li Z B, Fan X-H, Xue D J and Hu J-S 2023 Regioselective multisite atomic-chlorine passivation enables efficient and stable perovskite solar cells *J. Am. Chem. Soc.* **145** 5872
- [25] Guo J, Meng G, Zhang X, Huang H, Shi J, Wang B, Hu X, Yuan J and Ma W 2023 Dual-interface modulation with covalent organic framework enables efficient and durable perovskite solar cells *Adv. Mater.* **35** 2302839
- [26] Yi Z, Xiao B, Li X, Luo Y, Jiang Q and Yang J 2023 Novel dual-modification strategy using Ce-containing compounds toward high-performance flexible perovskite solar cells *Nano Energy* **109** 108241
- [27] Li X R *et al* 2023 Trans-spatial structure additive passivated Sn(ii) for high-efficiency CsSnI₃ perovskite solar cells fabricated in humid air *Chemnanomat* **9** e202200481
- [28] Ren Y, Ren M, Xie X, Wang J, Cai Y, Yuan Y, Zhang J and Wang P 2021 A spiro-OMeTAD based semiconductor composite with over 100 °C glass transition temperature for durable perovskite solar cells *Nano Energy* **81** 105655
- [29] He L, Zhang Y, Wei Y, Cai Y, Zhang J and Wang P 2023 A helicene-based semiconducting polymer for stable and efficient perovskite solar cells *Matter* **6** 4013–31
- [30] Eperon G E, Paternò G M, Sutton R J, Zampetti A, Haghighirad A A, Cacialli F and Snaith H J 2015 Inorganic caesium lead iodide perovskite solar cells *J. Mater. Chem. A* **3** 19688–95
- [31] Mali S S, Patil J V, Shao J-Y, Zhong Y-W, Rondiya S R, Dzade N Y and Hong C K 2023 Phase-heterojunction all-inorganic perovskite solar cells surpassing 21.5% efficiency *Nat. Energy* **8** 989–1001
- [32] Khan U, Rauf A, Feng S, Akbar A R, Peng G, Zheng Q, Wu R, Khan M, Peng Z and Liu F 2023 Thermally stable and efficient CsF-doped all-inorganic CsPbI₂Br₂ perovskite solar cells exceeding 15% PCE *Inorg. Chem. Commun.* **153** 110862
- [33] Liu X, Lian H, Zhou Z, Zou C, Xie J, Zhang F, Yuan H, Yang S, Hou Y and Yang H G 2022 Stoichiometric dissolution of defective CsPbI₂Br surfaces for inorganic solar cells with 17.5% efficiency *Adv. Energy Mater.* **12** 2103933
- [34] Zhou Q, Duan J, Du J, Guo Q, Zhang Q, Yang X, Duan Y and Tang Q 2021 Tailored lattice “tape” to confine tensile interface for 11.08%-efficiency all-inorganic CsPbBr₃ perovskite solar cell with an ultrahigh voltage of 1.702 V *Adv. Sci.* **8** 2101418
- [35] Jeong M J, Jeon S W, Kim S Y and Noh J H 2023 High fill factor CsPbI₂Br perovskite solar cells via crystallization management *Adv. Energy Mater.* **13** 2300698
- [36] Xiao H, Zuo C, Zhang L, Zhang W, Hao F, Yi C, Liu F, Jin H and Ding L 2023 Efficient inorganic perovskite solar cells made by drop-coating in ambient air *Nano Energy* **106** 108061
- [37] Sun N *et al* 2024 Tailoring crystallization dynamics of CsPbI₃ for scalable production of efficient inorganic perovskite solar cells *Adv. Funct. Mater.* **34** 2309894
- [38] Li Z, Wang J, Deng Y, Xi J, Zhang Y, Liu C and Guo W 2023 Undoped hole transport layer toward efficient and stable inorganic perovskite solar cells *Adv. Funct. Mater.* **33** 2214562
- [39] Wang G-E, Xiao G-B, Li C-P, Fu Z-H, Cao J and Xu G 2023 Directional defect management in perovskites by in situ decomposition of organic metal chalcogenides for efficient solar cells *Angew. Chem., Int. Ed.* **62** e202313833
- [40] Kang C, Xu S, Rao H, Pan Z and Zhong X 2023 All-inorganic CsPb₂I₄Br/CsPbI₂Br 2D/3D bulk heterojunction boosting carbon-based CsPbI₂Br perovskite solar cells with an efficiency of over 15% *ACS Energy Lett.* **8** 909–16
- [41] Luo M, Wang S, Zhu Z, Shi B, Wang P, Hou G, Huang Q, Zhao Y and Zhang X 2024 Novel cathode buffer layer

- enabling over 21.6%/20.9% efficiency in wide bandgap/inorganic perovskite solar cells *Nano Energy* **121** 109162
- [42] Zhang N *et al* 2023 Illumination enhanced crystallization and defect passivation for high performance CsPbI₃ perovskite solar cells by sacrificing dye *Adv. Funct. Mater.* **33** 2303873
- [43] Liu C *et al* 2023 Retarding solid-state reactions enable efficient and stable all-inorganic perovskite solar cells and modules *Sci. Adv.* **9** eadg0087
- [44] Yue Y, Yang R, Zhang W, Cheng Q, Zhou H and Zhang Y 2024 Cesium cyclopropane acid-aided crystal growth enables efficient inorganic perovskite solar cells with a high moisture tolerance *Angew. Chem., Int. Ed.* **63** e202315717
- [45] Wang H, Yang M, Cai W and Zang Z 2023 Suppressing phase segregation in CsPbI₂Br₂ films via anchoring halide ions toward underwater solar cells *Nano Lett.* **23** 4479–86
- [46] Wu X, Wang S, Zhang J, Shiu H-W, Hsu Y-J, Yan H, Zhu J and Lu X 2023 Bypassing the non-perovskite yellow phase: revealing and regulating the crystallization pathways for efficient all-inorganic perovskite solar cells *Nano Energy* **117** 108907
- [47] Liao Y *et al* 2023 Anti-dissociation passivation via bidentate anchoring for efficient carbon-based CsPbI_{2.6}Br_{0.4} solar cells *Adv. Funct. Mater.* **33** 2214784
- [48] Wu L *et al* 2023 Stabilization of inorganic perovskite solar cells with a 2D Dion–Jacobson passivating layer *Adv. Mater.* **35** 2304150
- [49] Xiao H, Zuo C, Yan K, Jin Z, Cheng Y, Tian H, Xiao Z, Liu F, Ding Y and Ding L 2023 Highly efficient and air-stable inorganic perovskite solar cells enabled by polylactic acid modification *Adv. Energy Mater.* **13** 2300738
- [50] Zhang H *et al* 2023 Tailored cysteine-derived molecular structures toward efficient and stable inorganic perovskite solar cells *Adv. Mater.* **35** 2301140
- [51] Zhang H *et al* 2022 Fluorine-containing passivation layer via surface chelation for inorganic perovskite solar cells *Angew. Chem., Int. Ed.* **62** e202216634
- [52] Ren W, Ren J, Wu Y, Li S, Sun Q and Hao Y 2024 An extraordinary antisolvent ethyl cyanoformate for achieving high efficiency and stability P3HT-based CsPbI₃ perovskite solar cells *Adv. Funct. Mater.* **34** 2311260
- [53] Liu Y, Xu T, Xu Z, Zhang H, Yang T, Wang Z, Xiang W and Liu S 2024 Defect passivation and lithium ion coordination via hole transporting layer modification for high performance inorganic perovskite solar cells *Adv. Mater.* **36** 2306982
- [54] Chu X *et al* 2023 Surface in situ reconstruction of inorganic perovskite films enabling long carrier lifetimes and solar cells with 21% efficiency *Nat. Energy* **8** 372–80
- [55] Hu M, Risqi A M, Wu J, Chen L, Park J, Lee S-U, Yun H-S, Park B-W, Brabec C J and Seok S I 2023 Highly stable n–i–p structured formamidinium tin triiodide solar cells through the stabilization of surface Sn²⁺ cations *Adv. Funct. Mater.* **33** 2300693
- [56] Wang G Q, Cheng L, Bi J Y, Chang J R and Meng F N 2024 B-site doping with bismuth ion enhances the efficiency and stability of inorganic CsSnI₃ perovskite solar cell *Mater. Lett.* **354** 135394
- [57] Chung I, Song J-H, Im J, Androulakis J, Malliakas C D, Li H, Freeman A J, Kenney J T and Kanatzidis M G 2012 CsSnI₃: semiconductor or metal? High electrical conductivity and strong near-infrared photoluminescence from a single material. High hole mobility and phase-transitions *J. Am. Chem. Soc.* **134** 8579–87
- [58] Li B, Chang B, Pan L, Li Z, Fu L, He Z and Yin L 2020 Tin-based defects and passivation strategies in tin-related perovskite solar cells *ACS Energy Lett.* **5** 3752–72
- [59] Wu T, Cui D, Liu X, Luo X, Su H, Segawa H, Zhang Y, Wang Y and Han L 2021 Additive engineering toward high-performance tin perovskite solar cells *Solar RRL* **5** 2100034
- [60] Zhang S *et al* 2023 Minimizing buried interfacial defects for efficient inverted perovskite solar cells *Science* **380** 404–9
- [61] Li Z *et al* 2023 Stabilized hole-selective layer for high-performance inverted p–i–n perovskite solar cells *Science* **382** 284–9
- [62] Park S M *et al* 2023 Low-loss contacts on textured substrates for inverted perovskite solar cells *Nature* **624** 289–94
- [63] Chen R *et al* 2023 Reduction of bulk and surface defects in inverted methylammonium- and bromide-free formamidinium perovskite solar cells *Nat. Energy* **8** 839–49
- [64] Liang Z *et al* 2023 Homogenizing out-of-plane cation composition in perovskite solar cells *Nature* **624** 557–63
- [65] Tan Q *et al* 2023 Inverted perovskite solar cells using dimethylacridine-based dopants *Nature* **620** 545–51
- [66] Tiwari N, Arianita Dewi H, Erdenebileg E, Narayan Chauhan R, Mathews N, Mhaisalkar S and Bruno A 2021 Advances and potentials of NiO_x surface treatments for p–i–n perovskite solar cells *Solar RRL* **6** 2100700
- [67] Yin X, Guo Y, Xie H, Que W and Kong L B 2019 Nickel oxide as efficient hole transport materials for perovskite solar cells *Solar RRL* **3** 230452
- [68] Pan Z *et al* 2023 Side-chain functionalized polymer hole-transporting materials with defect passivation effect for highly efficient inverted quasi-2D perovskite solar cells *Adv. Funct. Mater.* **33** 2304881
- [69] Zhao P, He D, Li S, Cui H, Yang Y, Chen W, Salah A S, Feng Y and Zhang B 2023 Design of a unique hole-transporting molecule via introducing a chloro-involved chelating moiety for high-performance inverted perovskite solar cells *Adv. Funct. Mater.* **34** 2308795
- [70] Li H *et al* 2023 2D/3D heterojunction engineering at the buried interface towards high-performance inverted methylammonium-free perovskite solar cells *Nat. Energy* **8** 946–55
- [71] Li Z, Li B, Wu X, Sheppard S A, Zhang S, Gao D, Long N J and Zhu Z 2022 Organometallic-functionalized interfaces for highly efficient inverted perovskite solar cells *Science* **376** 416–20
- [72] Di Girolamo D, Matteocci F, Piccinni M, Di Carlo A and Dini D 2020 Anodically electrodeposited NiO nanoflakes as hole selective contact in efficient air processed p–i–n perovskite solar cells *Solar Energy Mater. Solar Cells* **205** 110288
- [73] Zhou Q, Qiu J, Wang Y, Yu M, Liu J and Zhang X 2021 Multifunctional chemical bridge and defect passivation for highly efficient inverted perovskite solar cells *ACS Energy Lett.* **6** 1596–606
- [74] Zhou Q S, Qiu J M, Zhuang R S, Mei X Y, Hua Y and Zhang X L 2023 Understanding the dopant of hole-transport polymers for efficient inverted perovskite solar cells with high electroluminescence *J. Mater. Chem. A* **11** 5199–211
- [75] Li B *et al* 2020 Reduced bilateral recombination by functional molecular interface engineering for efficient inverted perovskite solar cells *Nano Energy* **78** 105249
- [76] Stollerfoht M *et al* 2018 Visualization and suppression of interfacial recombination for high-efficiency large-area pin perovskite solar cells *Nat. Energy* **3** 847–54
- [77] Xu H *et al* 2023 Constructing robust heterointerfaces for carrier viaduct via interfacial molecular bridges enables efficient and stable inverted perovskite solar cells *Energy Environ. Sci.* **16** 5792–804

- [78] Ali F, Roldán-Carmona C, Sohail M and Nazeeruddin M K 2020 Applications of self-assembled monolayers for perovskite solar cells interface engineering to address efficiency and stability *Adv. Energy Mater.* **10** 2002989
- [79] Liu M, Bi L, Jiang W, Zeng Z, Tsang S W, Lin F R and Jen A K Y 2023 Compact hole-selective self-assembled monolayers enabled by disassembling micelles in solution for efficient perovskite solar cells *Adv. Mater.* **35** 2304415
- [80] Wu T *et al* 2023 Graphene-like conjugated molecule as hole-selective contact for operationally stable inverted perovskite solar cells and modules *Adv. Mater.* **35** 2300169
- [81] Jiang Q, Tirawat R, Kerner R A, Gaulding E A, Xian Y, Wang X, Newkirk J M, Yan Y, Berry J J and Zhu K 2023 Towards linking lab and field lifetimes of perovskite solar cells *Nature* **623** 313–8
- [82] Zheng X *et al* 2023 Co-deposition of hole-selective contact and absorber for improving the processability of perovskite solar cells *Nat. Energy* **8** 462–72
- [83] Peng W *et al* 2023 Reducing nonradiative recombination in perovskite solar cells with a porous insulator contact *Science* **379** 683–90
- [84] Li L *et al* 2022 Flexible all-perovskite tandem solar cells approaching 25% efficiency with molecule-bridged hole-selective contact *Nat. Energy* **7** 708–17
- [85] Ren Z, Cui Z, Shi X, Wang L, Dou Y, Wang F, Lin H, Yan H and Chen S 2023 Poly(carbazole phosphonic acid) as a versatile hole-transporting material for p-i-n perovskite solar cells and modules *Joule* **7** 2894–904
- [86] Huang Y *et al* 2023 Stabilization of α -phase FAPbI₃ via buffering interfacial region for efficient p-i-n perovskite solar cells *Adv. Funct. Mater.* **33** 2302375
- [87] Yu S *et al* 2023 Homogenized NiO_x nanoparticles for improved hole transport in inverted perovskite solar cells *Science* **382** 1399–404
- [88] Li C *et al* 2023 Rational design of Lewis base molecules for stable and efficient inverted perovskite solar cells *Science* **379** 690–4
- [89] Li G *et al* 2023 Highly efficient p-i-n perovskite solar cells that endure temperature variations *Science* **379** 399–403
- [90] Li F *et al* 2023 Hydrogen-bond-bridged intermediate for perovskite solar cells with enhanced efficiency and stability *Nat. Photon.* **17** 478–84
- [91] Jiang X *et al* 2023 Strain regulation via pseudo halide-based ionic liquid toward efficient and stable α -FAPbI₃ inverted perovskite solar cells *Adv. Energy Mater.* **13** 2300700
- [92] Wang T *et al* 2023 Synergistic defect healing and device encapsulation via structure regulation by silicone polymer enables durable inverted perovskite photovoltaics with high efficiency *Adv. Energy Mater.* **14** 2302552
- [93] Yuan X, Li R, Xiong Z, Li P, Odunmbaku G O, Sun K, Deng Y and Chen S 2023 Synergistic crystallization modulation and defects passivation via additive engineering stabilize perovskite films for efficient solar cells *Adv. Funct. Mater.* **33** 2215096
- [94] Li J *et al* 2023 The synergistic effect of pemirolast potassium on carrier management and strain release for high-performance inverted perovskite solar cells *Adv. Funct. Mater.* **33** 2301956
- [95] Yang J, Sheng W, Li X, Zhong Y, Su Y, Tan L and Chen Y 2023 Synergistic toughening and self-healing strategy for highly efficient and stable flexible perovskite solar cells *Adv. Funct. Mater.* **33** 2214984
- [96] Pan T *et al* 2023 Surface-energy-regulated growth of α -phase Cs_{0.03}FA_{0.97}PbI₃ for highly efficient and stable inverted perovskite solar cells *Adv. Mater.* **2208522** 35
- [97] Zhou Q, Qiu J, Zhuang R, Yu M, Liu J, Hua Y, Ding L and Zhang X 2023 Ionic liquid-induced multisite synergistic interactions for highly efficient inverted perovskite solar cells *ACS Appl. Mater. Interfaces* **15** 40676–86
- [98] Castriotta L A *et al* 2023 A universal multi-additive strategy to enhance efficiency and stability in inverted perovskite solar cells *Nano Energy* **109** 108268
- [99] Xie L, Liu J, Li J, Liu C, Pu Z, Xu P, Wang Y, Meng Y, Yang M and Ge Z 2023 A deformable additive on defects passivation and phase segregation inhibition enables the efficiency of inverted perovskite solar cells over 24% *Adv. Mater.* **35** 2302752
- [100] Li L *et al* 2023 Buried-interface engineering enables efficient and 1960-hour ISOS-L-2I stable inverted perovskite solar cells *Adv. Mater.* **36** 2303869
- [101] Cassella E J *et al* 2023 Binary solvent system used to fabricate fully annealing-free perovskite solar cells *Adv. Energy Mater.* **13** 2203468
- [102] Fang Y *et al* 2023 Tailoring precursor chemistry enabled room temperature-processed perovskite films in ambient air for efficient and stable solar cells with improved reproducibility *Adv. Funct. Mater.* **33** 2303674
- [103] Li M *et al* 2023 In situ surface reconstruction toward planar heterojunction for efficient and stable FAPbI₃ quantum dot solar cells *Adv. Mater.* **36** 2309890
- [104] Shen L *et al* 2023 Ion-diffusion management enables all-interface defect passivation of perovskite solar cells *Adv. Mater.* **35** 2301624
- [105] Wang J, Wang K, Zhang C, Liu S, Guan X, Liang C, Chen C C and Xie F 2023 Surface cleaning and passivation strategy for durable inverted formamidinium–cesium triiodide perovskite solar cells *Adv. Energy Mater.* **13** 2302169
- [106] Zheng Y, Wu X, Zhuang R, Tian C, Sun A, Tang C, Liu Y, Hua Y and Chen C C 2023 Managing interfacial hot-carrier cooling and extraction kinetics for inverted ma-free perovskite solar cells over 23% efficiency via Dion–Jacobson 2D capping layer *Adv. Funct. Mater.* **33** 2300576
- [107] Ramakrishnan S, Song D, Xu Y, Zhang X, Aksoy G, Cotlet M, Li M, Zhang Y and Yu Q 2023 Solvent-mediated formation of quasi-2D Dion–Jacobson phases on 3D perovskites for inverted solar cells over 23% efficiency *Adv. Energy Mater.* **13** 2302240
- [108] Guo H, Wang X, Li C, Hu H, Zhang H, Zhang L, Zhu W H and Wu Y 2023 Immobilizing surface halide in perovskite solar cells via calix[4]pyrrole *Adv. Mater.* **35** 2301871
- [109] Li D *et al* 2023 Surface regulation with polymerized small molecular acceptor towards efficient inverted perovskite solar cells *Adv. Energy Mater.* **13** 2204247
- [110] He Z, Li M, Jia H, Yu R, Zhang Y, Wang R, Dong Y, Liu X, Xu D and Tan Z 2023 Managing interfacial charged defects with multiple active sited macrocyclic valinomycin for efficient and stable inverted perovskite solar cells *Adv. Mater.* **35** 2304918
- [111] Zhang X *et al* 2023 Minimizing the interface-driven losses in inverted perovskite solar cells and modules *ACS Energy Lett.* **8** 2532–42
- [112] Guo X *et al* 2023 Mitigating surface deficiencies of perovskite single crystals enables efficient solar cells with enhanced moisture and reverse-bias stability *Adv. Funct. Mater.* **33** 2213995
- [113] Jiang Q *et al* 2022 Surface reaction for efficient and stable inverted perovskite solar cells *Nature* **611** 278–83
- [114] Jiang N, Zhang H-W, Liu Y-F, Wang Y-F, Yin D and Feng J 2023 Transfer-imprinting-assisted growth of 2D/3D perovskite heterojunction for efficient and stable flexible inverted perovskite solar cells *Nano Lett.* **23** 6116–23
- [115] Qian Y, Li J, Cao H, Ren Z, Dai X, Huang T, Zhang S, Qiu Y, Yang L and Yin S 2023 Passivating perovskites in air via an alternating cation interlayer phase formed by benzylamine vapor fumigation *Adv. Funct. Mater.* **33** 2214731

- [116] Shi W, Zhuang Q, Zhou R, Hou X, Zhao X, Kong J and Fuchter M J 2023 Enantiomerically pure fullerenes as a means to enhance the performance of perovskite solar cells *Adv. Energy Mater.* **13** 2300054
- [117] Sun X *et al* 2023 VOC of inverted perovskite solar cells based on n-doped PCBM exceeds 1.2 V: interface energy alignment and synergistic passivation *Adv. Energy Mater.* **13** 2302191
- [118] Shui Q-J *et al* 2023 Evaporable fullerene indanones with controlled amorphous morphology as electron transport layers for inverted perovskite solar cells *J. Am. Chem. Soc.* **145** 27307–15
- [119] Xiao M *et al* 2023 Engineering amorphous-crystallized interface of ZrN_x barriers for stable inverted perovskite solar cells *Adv. Mater.* **35** 2301684
- [120] Liu N *et al* 2023 Multifunctional anti-corrosive interface modification for inverted perovskite solar cells *Adv. Energy Mater.* **13** 2300025
- [121] Liu A, Li X, Zhang W, Yang H, Guo X, Lu C, Yuan H, Ou-Yang W and Fang J 2023 Ag electrode anticorrosion in inverted perovskite solar cells *Adv. Funct. Mater.* **34** 2307310
- [122] Cai P *et al* 2023 Tetrabutylammonium bromide functionalized $\text{Ti}_3\text{C}_2\text{T}_x$ MXene as versatile cathode buffer layer for efficient and stable inverted perovskite solar cells *Adv. Funct. Mater.* **33** 2300113
- [123] Qin W *et al* 2023 Suppressing non-radiative recombination in metal halide perovskite solar cells by synergistic effect of ferroelasticity *Nat. Commun.* **14** 256
- [124] Ali W, Qin W, Tian H, Guo J, Feng Z and Li C 2023 Tuning lattice structure of ferroelastic twin-domains achieving efficient perovskite solar cells *ACS Energy Lett.* **8** 5070–8
- [125] Duan C, Zou F, Wen Q, Qin M, Li J, Chen C, Lu X, Ding L and Yan K 2023 A bifunctional carbazide additive for durable CsSnI_3 perovskite solar cells *Adv. Mater.* **35** 2300503
- [126] Sun H *et al* 2023 Surface defects management by in situ etching with methanol for efficient inverted inorganic perovskite solar cells *Adv. Funct. Mater.* **33** 2213913
- [127] Wang S, Li M-H, Zhang Y, Jiang Y, Xu L, Wang F and Hu J-S 2023 Surface n-type band bending for stable inverted CsPbI_3 perovskite solar cells with over 20% efficiency *Energy Environ. Sci.* **16** 2572–8
- [128] Xu T, Xiang W, Yang J, Kubicki D J, Tress W, Chen T, Fang Z, Liu Y and Liu S 2023 Interface modification for efficient and stable inverted inorganic perovskite solar cells *Adv. Mater.* **35** 2303346
- [129] Wang S, Wang P, Shi B, Sun C, Sun H, Qi S, Huang Q, Xu S, Zhao Y and Zhang X 2023 Inorganic perovskite surface reconfiguration for stable inverted solar cells with 20.38% efficiency and its application in tandem devices *Adv. Mater.* **35** 2300581
- [130] Pu X, Cao Q, Su J, Yang J, Wang T, Zhang Y, Chen H, He X, Chen X and Li X 2023 One-step construction of a perovskite/ TiO_2 heterojunction toward highly stable inverted all-layer-inorganic CsPbI_2Br perovskite solar cells with 17.1% efficiency *Adv. Energy Mater.* **13** 2301607
- [131] Peng Z *et al* 2023 Reducing open-circuit voltage losses in all-inorganic perovskite cells by dedoping *ACS Energy Lett.* **8** 2077–85
- [132] Chen H *et al* 2023 Regulating surface potential maximizes voltage in all-perovskite tandems *Nature* **613** 676–81
- [133] Li T, He F, Liang J and Qi Y 2023 Functional layers in efficient and stable inverted tin-based perovskite solar cells *Joule* **7** 1966–91
- [134] Wang J *et al* 2023 Oriented attachment of tin halide perovskites for photovoltaic applications *ACS Energy Lett.* **8** 1590–6
- [135] Chang B, Li H, Wang L, Pan L, Wu Y, Liu Z and Yin L 2023 Molecular ferroelectric with directional polarization field for efficient tin-based perovskite solar cells *Adv. Funct. Mater.* **33** 2305852
- [136] Li T, Zhang Z, He F, Deng L, Yang Y, Mo X, Zhan Y and Liang J 2023 Alleviating the crystallization dynamics and suppressing the oxidation process for tin-based perovskite solar cells with fill factors exceeding 80% *Adv. Funct. Mater.* **33** 2308457
- [137] Zheng C *et al* 2023 Dual effects of slow recrystallization and defects passivation achieve efficient tin-based perovskite solar cells with good stability up to one year *Adv. Funct. Mater.* **33** 2212106
- [138] Liu G, Jiang X, Feng W, Yang G, Chen X, Ning Z and Wu W Q 2023 Synergic electron and defect compensation minimizes voltage loss in lead-free perovskite solar cells *Angew. Chem., Int. Ed.* **62** e202305551
- [139] Rao H, Su Y, Liu G, Zhou H, Yang J, Sheng W, Zhong Y, Tan L and Chen Y 2023 Monodisperse adducts-induced homogeneous nucleation towards high-quality tin-based perovskite film *Angew. Chem., Int. Ed.* **62** e202306712
- [140] Sun C *et al* 2023 Well-defined fullerene bisadducts enable high-performance tin-based perovskite solar cells *Adv. Mater.* **35** 2205603
- [141] Yang P *et al* 2023 Efficient tin-based perovskite solar cells enabled by precisely synthesized single-isomer fullerene bisadducts with regulated molecular packing *J. Am. Chem. Soc.* **146** 2494–502
- [142] Kitamura T *et al* 2023 Sn perovskite solar cells with tin oxide nanoparticle layer as hole transport layer *ACS Energy Lett.* **8** 3565–8
- [143] Afraj S N, Kuan C H, Lin J S, Ni J S, Velusamy A, Chen M C and Diao E W G 2023 Quinoxaline-based X-shaped sensitizers as self-assembled monolayer for tin perovskite solar cells *Adv. Funct. Mater.* **33** 2213939
- [144] Li B, Zhang C, Gao D, Sun X, Zhang S, Li Z, Gong J, Li S and Zhu Z 2023 Suppressing oxidation at perovskite– NiO_x interface for efficient and stable tin perovskite solar cells *Adv. Mater.* **36** 2309768
- [145] Wang L *et al* 2023 14.31% power conversion efficiency of Sn-based perovskite solar cells via efficient reduction of Sn^{4+} *Angew. Chem., Int. Ed.* **62** e202307228
- [146] Song D, Ramakrishnan S, Xu Y and Yu Q 2023 Designing effective hole transport layers in tin perovskite solar cells *ACS Energy Lett.* **8** 4162–72
- [147] Balasaravanan R *et al* 2023 Triphenylamine (TPA)-functionalized structural isomeric polythiophenes as dopant free hole-transporting materials for tin perovskite solar cells *Adv. Energy Mater.* **13** 2302047
- [148] Kuan C H, Balasaravanan R, Hsu S M, Ni J S, Tsai Y T, Zhang Z X, Chen M C and Diao E W G 2023 Dopant-free pyrrolopyrrole-based (PPr) polymeric hole-transporting materials for efficient tin-based perovskite solar cells with stability over 6000 h *Adv. Mater.* **35** 2300681
- [149] Aktas E *et al* 2023 One-step solution deposition of tin-perovskite onto a self-assembled monolayer with a DMSO-free solvent system *ACS Energy Lett.* **8** 5170–4
- [150] Song D, Li H, Xu Y and Yu Q 2023 Amplifying hole extraction characteristics of PEDOT:PSS via post-treatment with aromatic diammonium acetates for tin perovskite solar cells *ACS Energy Lett.* **8** 3280–7
- [151] Sun Q, Gu A, Yu H, Shen Y and Wang M 2023 A single crystal derived precursor for improving the performance of CsSnI_3 perovskite solar cells *J. Mater. Chem. A* **11** 17292–7
- [152] Meng X, Wu T, Liu X, He X, Noda T, Wang Y, Segawa H and Han L 2020 Highly reproducible and efficient FASnI_3 perovskite solar cells fabricated with volatilizable reducing solvent *J. Phys. Chem. Lett.* **11** 2965–71

- [153] Yan L, Ma J, Li P, Zang S, Han L, Zhang Y and Song Y 2022 Charge-carrier transport in quasi-2D Ruddlesden–Popper perovskite solar cells *Adv. Mater.* **34** 2106822
- [154] Cao Q, Li P, Chen W, Zang S, Han L, Zhang Y and Song Y 2022 Two-dimensional perovskites: impacts of species, components, and properties of organic spacers on solar cells *Nano Today* **43** 101394
- [155] Peng S, Ma J, Li P, Zang S, Zhang Y and Song Y 2022 Regulation of quantum wells width distribution in 2D perovskite films for photovoltaic application *Adv. Funct. Mater.* **32** 2205289
- [156] Zhao R, Guo L, Zhu H, Zhang T, Li P, Zhang Y and Song Y 2023 Regulation of quantum wells width distribution in quasi-2D perovskite films for high-performance photodetectors *Adv. Mater.* **35** 2301232
- [157] Li P, Zhang Y, Liang C, Xing G, Liu X, Li F, Liu X, Hu X, Shao G and Song Y 2018 Phase pure 2D perovskite for high-performance 2D–3D heterostructured perovskite solar cells *Adv. Mater.* **30** 1805323
- [158] Li P, Liu X, Zhang Y, Liang C, Chen G, Li F, Su M, Xing G, Tao X and Song Y 2020 Low-dimensional Dion–Jacobson-phase lead-free perovskites for high-performance photovoltaics with improved stability *Angew. Chem., Int. Ed.* **59** 6909–14
- [159] Zhu H, Ma J, Li P, Zang S, Zhang Y and Song Y 2022 Low-dimensional Sn-based perovskites: evolution and future prospects of solar cells *Chem* **8** 2939–60
- [160] Li P *et al* 2023 Dredging the charge-carrier transfer pathway for efficient low-dimensional Ruddlesden–Popper perovskite solar cells *Angew. Chem., Int. Ed.* **62** e202217910
- [161] Zhang Y *et al* 2023 Highly efficient and stable fa-based quasi-2D Ruddlesden–Popper perovskite solar cells by the incorporation of β -fluorophenylethanamine cations *Adv. Mater.* **35** 2210836
- [162] Chen M, Dong X, Xin Y, Gao Y, Fu Q, Wang R, Xu Z, Chen Y and Liu Y 2023 Crystal growth regulation of Ruddlesden–Popper perovskites via self-assembly of semiconductor spacers for efficient solar cells *Angew. Chem., Int. Ed.* **63** e202315943
- [163] Dong X, Chen M, Wang R, Ling Q, Hu Z, Liu H, Xin Y, Yang Y, Wang J and Liu Y 2023 Quantum confinement breaking: orbital coupling in 2D Ruddlesden–Popper perovskites enables efficient solar cells *Adv. Energy Mater.* **13** 2301006
- [164] Wang R, Dong X, Ling Q, Hu Z, Gao Y, Chen Y and Liu Y 2023 Nucleation and crystallization in 2D Ruddlesden–Popper perovskites using formamidinium-based organic semiconductor spacers for efficient solar cells *Angew. Chem., Int. Ed.* **62** e202314690
- [165] Ahmad S, Guan M, Kim J, He X, Ren Z, Zhang H, Su H and Choy W C H 2023 High-quality pure-phase MA-free formamidinium Dion–Jacobson 2D perovskites for stable unencapsulated photovoltaics *Adv. Energy Mater.* **14** 2302774
- [166] Wu G *et al* 2023 Crystallinity and phase control in formamidinium-based Dion–Jacobson 2D perovskite via seed-induced growth for efficient photovoltaics *Adv. Mater.* **35** 2303061
- [167] Kim J H *et al* 2023 Efficient and stable quasi-2D Ruddlesden–Popper perovskite solar cells by tailoring crystal orientation and passivating surface defects *Adv. Mater.* **35** 2302143
- [168] Chen L *et al* 2023 In situ SnSe deposition as passivation for scalable and stable quasi-2D lead–tin perovskite solar cells *Energy Environ. Sci.* **16** 5315–24
- [169] Qin Z, Pols M, Qin M, Zhang J, Yan H, Tao S and Lu X 2023 Over-18%-efficiency quasi-2D Ruddlesden–Popper Pb–Sn mixed perovskite solar cells by compositional engineering *ACS Energy Lett.* **8** 3188–95
- [170] Wang H, Yang F, Li X and Zhang P 2023 Fully printed high-performance quasi-two-dimensional perovskite solar cells via multifunctional interfacial engineering *Adv. Funct. Mater.* **34** 2312250
- [171] Zhang Y, Zhang Y, Niu B, Huang Y, Wu H, Fu W and Chen H 2023 Construction of 2D/3D/2D-structured perovskite for high-performance and stable solar cells *Adv. Funct. Mater.* **33** 2307949
- [172] Meftahi N *et al* 2023 Machine learning enhanced high-throughput fabrication and optimization of quasi-2D Ruddlesden–Popper perovskite solar cells *Adv. Energy Mater.* **13** 2203859
- [173] Wu M *et al* 2023 Crystallization regulation by self-assembling liquid crystal template enables efficient and stable perovskite solar cells *Angew. Chem., Int. Ed.* **62** e202313472
- [174] Pandey S, Ko J, Park B, Byun J and Lee M-J 2023 Single crystal perovskite-based solar cells: growth, challenges, and potential strategies *Chem. Eng. J.* **466** 143019
- [175] Lou Y, Zhang S, Gu Z, Wang N, Wang S, Zhang Y and Song Y 2023 Perovskite single crystals: dimensional control, optoelectronic properties, and applications *Mater. Today* **62** 225–50
- [176] Ghasemi M, Yuan S, Fan J, Jia B and Wen X 2023 Challenges in the development of metal-halide perovskite single crystal solar cells *J. Mater. Chem. A* **11** 3822–48
- [177] Almasabi K *et al* 2023 Hole-transporting self-assembled monolayer enables efficient single-crystal perovskite solar cells with enhanced stability *ACS Energy Lett.* **8** 950–6
- [178] Lintangpradipto M N, Zhu H, Shao B, Mir W J, Gutierrez-Arzaluz L, Turedi B, Abulikemu M, Mohammed O F and Bakr O M 2023 Single-crystal methylammonium-free perovskite solar cells with efficiencies exceeding 24% and high thermal stability *ACS Energy Lett.* **8** 4915–22
- [179] Liu N, Li N, Jiang C, Lv M, Wu J and Chen Z 2024 Perovskite single crystals with self-cleaning surface for efficient photovoltaics *Angew. Chem., Int. Ed.* **63** 202314089
- [180] Song Z, Gao Y, Zou Y, Zhang H, Wang R, Chen Y, Chen Y and Liu Y 2024 Single-crystal-assisted in situ phase reconstruction enables efficient and stable 2D/3D perovskite solar cells *J. Am. Chem. Soc.* **146** 1657–66
- [181] Han B *et al* 2023 Rational design of ferroelectric 2D perovskite for improving the efficiency of flexible perovskite solar cells over 23% *Angew. Chem., Int. Ed.* **62** e202217526
- [182] Chen Z *et al* 2023 Perovskite grain-boundary manipulation using room-temperature dynamic self-healing “ligaments” for developing highly stable flexible perovskite solar cells with 23.8% efficiency *Adv. Mater.* **35** e2300513
- [183] Liu C *et al* 2023 Concurrent top and buried surface optimization for flexible perovskite solar cells with high efficiency and stability *Adv. Funct. Mater.* **33** 2212698
- [184] Meng Y *et al* 2023 Pre-buried ETL with bottom-up strategy toward flexible perovskite solar cells with efficiency over 23% *Adv. Funct. Mater.* **33** 2214788
- [185] Cai W *et al* 2023 Interfacial engineering for efficient low-temperature flexible perovskite solar cells *Angew. Chem., Int. Ed.* **62** e202309398
- [186] Aydin E *et al* 2023 Enhanced optoelectronic coupling for perovskite/silicon tandem solar cells *Nature* **623** 732–8
- [187] Mariotti S *et al* 2023 Interface engineering for high-performance, triple-halide perovskite–silicon tandem solar cells *Science* **381** 63–69

- [188] Chin X Y *et al* 2023 Interface passivation for 31.25%-efficient perovskite/silicon tandem solar cells *Science* **381** 59–63
- [189] Lin R *et al* 2023 All-perovskite tandem solar cells with 3D/3D bilayer perovskite heterojunction *Nature* **620** 994–1000
- [190] Zhou S *et al* 2023 Aspartate all-in-one doping strategy enables efficient all-perovskite tandems *Nature* **624** 69–73
- [191] Liu C *et al* 2023 Bimolecularly passivated interface enables efficient and stable inverted perovskite solar cells *Science* **382** 810–5
- [192] Wang X *et al* 2023 Highly efficient perovskite/organic tandem solar cells enabled by mixed-cation surface modulation *Adv. Mater.* **35** 2305946
- [193] An Y *et al* 2023 Optimizing crystallization in wide-bandgap mixed halide perovskites for high-efficiency solar cells *Adv. Mater.* **36** e2306568
- [194] Duong T *et al* 2023 Bulk incorporation with 4-methylphenethylammonium chloride for efficient and stable methylammonium-free perovskite and perovskite-silicon tandem solar cells *Adv. Energy Mater.* **13** 2203607
- [195] Guan H *et al* 2023 Regulating crystal orientation via ligand anchoring enables efficient wide-bandgap perovskite solar cells and tandems *Adv. Mater.* **36** 2307987
- [196] Liang H *et al* 2023 29.9%-efficient, commercially viable perovskite/CuInSe₂ thin-film tandem solar cells *Joule* **7** 2859–72
- [197] Liu Z *et al* 2023 Reducing perovskite/C₆₀ interface losses via sequential interface engineering for efficient perovskite/silicon tandem solar cell *Adv. Mater.* **36** 2308370
- [198] Zheng J, Ying Z, Yang Z, Lin Z, Wei H, Chen L, Yang X, Zeng Y, Li X and Ye J 2023 Polycrystalline silicon tunnelling recombination layers for high-efficiency perovskite/tunnel oxide passivating contact tandem solar cells *Nat. Energy* **8** 1250–61
- [199] Ren N *et al* 2023 Multifunctional additive CdAc₂ for efficient perovskite-based solar cells *Adv. Mater.* **35** 2211806
- [200] Li X *et al* 2023 Surface reconstruction for efficient and stable monolithic perovskite/silicon tandem solar cells with greatly suppressed residual strain *Adv. Mater.* **35** 2211962
- [201] Liu C *et al* 2023 Efficient all-perovskite tandem solar cells with low-optical-loss carbazoyl interconnecting layers *Angew. Chem., Int. Ed.* **62** e202313374
- [202] Wen J *et al* 2023 Heterojunction formed via 3D-to-2D perovskite conversion for photostable wide-bandgap perovskite solar cells *Nat. Commun.* **14** 7118
- [203] He R *et al* 2023 Improving interface quality for 1-cm² all-perovskite tandem solar cells *Nature* **618** 80–86
- [204] Jiang S, Wang R, Li M, Yu R, Wang F and Tan Z 2024 Synergistic electrical and light management enables efficient monolithic inorganic perovskite/organic tandem solar cells with over 24% efficiency *Energy Environ. Sci.* **17** 219–26
- [205] Mali S S, Patil J V, Steele J A, Nazeeruddin M K, Kim J H and Hong C K 2024 All-inorganic halide perovskites for air-processed “n-i-p” monolithic perovskite/organic hybrid tandem solar cells exceeding 23% efficiency *Energy Environ. Sci.* **17** 1046–60
- [206] Ma Z, Dong Y, Wang R, Xu Z, Li M and Tan Z 2023 Transparent recombination electrode with dual-functional transport and protective layer for efficient and stable monolithic perovskite/organic tandem solar cells *Adv. Mater.* **35** 2307502
- [207] Sun S Q *et al* 2023 All-inorganic perovskite-based monolithic perovskite/organic tandem solar cells with 23.21% efficiency by dual-interface engineering *Adv. Energy Mater.* **13** 2204347
- [208] Li Z *et al* 2023 In situ epitaxial growth of blocking structure in mixed-halide wide-band-gap perovskites for efficient photovoltaics *Joule* **7** 1363–81
- [209] Wu M *et al* 2023 Reconstruction of the indium tin oxide surface enhances the adsorption of high-density self-assembled monolayer for perovskite/silicon tandem solar cells *Adv. Funct. Mater.* **33** 2304708
- [210] Zhang W *et al* 2023 Bottom-up modification boosts the performance of narrow-bandgap lead–tin perovskite single-junction and tandem solar cells *Energy Environ. Sci.* **16** 5852–62
- [211] Yi Z *et al* 2024 Achieving a high open-circuit voltage of 1.339 V in 1.77 eV wide-bandgap perovskite solar cells via self-assembled monolayers *Energy Environ. Sci.* **17** 202–9
- [212] Liu X *et al* 2023 Over 28% efficiency perovskite/Cu(InGa)Se₂ tandem solar cells: highly efficient sub-cells and their bandgap matching *Energy Environ. Sci.* **16** 5029–42
- [213] Liu L *et al* 2023 2022 4-terminal inorganic perovskite/organic tandem solar cells offer 22% efficiency *Nano-Micro Lett.* **15** 23
- [214] Chittiboina G V, Singareddy A, Agarwal A, Bhatia S and Nair P R 2023 Intrinsic degradation-dependent energy yield estimates for perovskite/silicon tandem solar cells under field conditions *ACS Energy Lett.* **8** 2927–34
- [215] Li R *et al* 2023 UV encapsulated monolithic perovskite/silicon tandem solar cells for hundred-watt power system *ACS Energy Lett.* **8** 2414–22
- [216] Xu Z *et al* 2023 Reverse-bias resilience of monolithic perovskite/silicon tandem solar cells *Joule* **7** 1992–2002
- [217] Zeng Y *et al* 2023 Efficiency-loss analysis of monolithic perovskite/silicon tandem solar cells by identifying the patterns of a dual two-diode model’s current-voltage curves *J. Semicond.* **44** 082702
- [218] Zheng J *et al* 2023 Efficient monolithic perovskite–Si tandem solar cells enabled by an ultra-thin indium tin oxide interlayer *Energy Environ. Sci.* **16** 1223–33
- [219] Qiao L, Ye T, Wang P, Wang T, Zhang L, Sun R, Kong W and Yang X 2023 Crystallization enhancement and ionic defect passivation in wide-bandgap perovskite for efficient and stable all-perovskite tandem solar cells *Adv. Funct. Mater.* **24** 2308908
- [220] Zhao Y *et al* 2023 Reduced 0.418 V VOC-deficit of 1.73 eV wide-bandgap perovskite solar cells assisted by dual chlorides for efficient all-perovskite tandems *Energy Environ. Sci.* **16** 2080–9
- [221] Yang F *et al* 2024 Minimizing interfacial recombination in 1.8 eV triple-halide perovskites for 27.5% efficient all-perovskite tandems *Adv. Mater.* **36** 2307743
- [222] Huang L *et al* 2023 Efficient narrow-bandgap mixed tin-lead perovskite solar cells via natural tin oxide doping *Adv. Mater.* **35** 2301125
- [223] Luo J *et al* 2023 Improved carrier management via a multifunctional modifier for high-quality low-bandgap Sn-Pb perovskites and efficient all-perovskite tandem solar cells *Adv. Mater.* **35** 2300352
- [224] Sun H *et al* 2023 Scalable solution-processed hybrid electron transport layers for efficient all-perovskite tandem solar modules *Adv. Mater.* **36** 2308706
- [225] Shi Y, Sun J, Zhou J, Wen T, Zou C, Liu D, Liu F, Yang S, Deng Y and Yang Z 2023 High-speed deposition of large-area narrow-bandgap perovskite films for all-perovskite tandem solar mini-modules *Adv. Funct. Mater.* **33** 2307209
- [226] Ma T *et al* 2023 Hole transport layer-free low-bandgap perovskite solar cells for efficient all-perovskite tandems *Adv. Mater.* **32** 2308240
- [227] Wang R, Han M, Wang Y, Zhao J, Zhang J, Ding Y, Zhao Y, Zhang X and Hou G 2023 Recent progress on efficient

- perovskite/organic tandem solar cells *J. Energy Chem.* **83** 158–72
- [228] Xie G, Li H, Wang X, Fang J, Lin D, Wang D, Li S, He S and Qiu L 2023 Phase segregation and voltage loss mitigated highly efficient perovskite–organic tandem solar cells with a simple ambipolar SnO_x interconnecting layer *Adv. Funct. Mater.* **33** 2308794
- [229] Tang Y *et al* 2023 Solvent engineering of scalable deposited wide-bandgap perovskites for efficient monolithic perovskite–organic tandem solar cells *Nano Energy* **114** 108653
- [230] Sun J and Ding L 2023 Perovskite/organic tandem solar cells *J. Semicond.* **44** 020201
- [231] Yao Q *et al* 2023 Dual sub-cells modification enables high-efficiency n–i–p type monolithic perovskite/organic tandem solar cells *Adv. Funct. Mater.* **33** 2212599
- [232] Hu X, Li J, Wang C, Cui H, Liu Y, Zhou S, Guan H, Ke W, Tao C and Fang G 2023 Antimony potassium tartrate stabilizes wide-bandgap perovskites for inverted 4-T all-perovskite tandem solar cells with efficiencies over 26% *Nano-Micro Lett.* **15** 103
- [233] Park N-G and Zhu K 2020 Scalable fabrication and coating methods for perovskite solar cells and solar modules *Nat. Rev. Mater.* **5** 333–50
- [234] Gu H *et al* 2023 Design optimization of bifacial perovskite minimodules for improved efficiency and stability *Nat. Energy* **8** 675–84
- [235] Deng Y, Zheng X, Bai Y, Wang Q, Zhao J and Huang J 2018 Surfactant-controlled ink drying enables high-speed deposition of perovskite films for efficient photovoltaic modules *Nat. Energy* **3** 560–6
- [236] Jia Z, Peng J, Yu L, Jiang T, Li Y, Yao F, Ren F and Lin Q 2022 Spray-coating of AgI incorporated metal halide perovskites for high-performance x-ray detection *Chem. Eng. J.* **450** 138229
- [237] Zhang L *et al* 2021 Ambient inkjet-printed high-efficiency perovskite solar cells: manipulating the spreading and crystallization behaviors of picoliter perovskite droplets *Solar RRL* **5** 2100106
- [238] Chen C *et al* 2022 Perovskite solar cells based on screen-printed thin films *Nature* **612** 266–71
- [239] Ávila J, Momblona C, Boix P P, Sessolo M and Bolink H J 2017 Vapor-deposited perovskites: the route to high-performance solar cell production? *Joule* **1** 431–42
- [240] Tait J G, Merckx T, Li W, Wong C, Gehlhaar R, Cheyns D, Turbiez M and Heremans P 2015 Determination of solvent systems for blade coating thin film photovoltaics *Adv. Funct. Mater.* **25** 3393–8
- [241] Chao L, Niu T, Gao W, Ran C, Song L, Chen Y and Huang W 2021 Solvent engineering of the precursor solution toward large-area production of perovskite solar cells *Adv. Mater.* **33** 2005410
- [242] Hu Y, Chu Y, Wang Q, Zhang Z, Ming Y, Mei A, Rong Y and Han H 2019 Standardizing perovskite solar modules beyond cells *Joule* **3** 2076–85
- [243] Deng Y, Van Brackle C H, Dai X, Zhao J, Chen B and Huang J 2019 Tailoring solvent coordination for high-speed, room-temperature blading of perovskite photovoltaic films *Sci. Adv.* **5** eaax7537
- [244] Chen S, Dai X, Xu S, Jiao H, Zhao L and Huang J 2021 Stabilizing perovskite–substrate interfaces for high-performance perovskite modules *Science* **373** 902–7
- [245] Fei C *et al* 2023 Lead-chelating hole-transport layers for efficient and stable perovskite minimodules *Science* **380** 823–9
- [246] Chung J *et al* 2023 Engineering perovskite precursor inks for scalable production of high-efficiency perovskite photovoltaic modules *Adv. Energy Mater.* **13** 2300595
- [247] Wang L *et al* 2023 Surfactant engineering for perovskite solar cells and submodules *Matter* **6** 2987–3005
- [248] Li J *et al* 2021 20.8% slot-die coated MAPbI₃ perovskite solar cells by optimal DMSO-content and age of 2-ME based precursor inks *Adv. Energy Mater.* **11** 2003460
- [249] Li J *et al* 2023 Ink design enabling slot-die coated perovskite solar cells with >22% power conversion efficiency, micro-modules, and 1 year of outdoor performance evaluation *Adv. Energy Mater.* **13** 2203898
- [250] Sangale S S, Kwon S-N, Patil P, Lee H-J and Na S-I 2023 Locally supersaturated inks for a slot-die process to enable highly efficient and robust perovskite solar cells *Adv. Energy Mater.* **13** 2300537
- [251] Rana P J S *et al* 2023 Molecular locking with all-organic surface modifiers enables stable and efficient slot-die-coated methyl-ammonium-free perovskite solar modules *Adv. Mater.* **35** 2210176
- [252] Fan B, Xiong J, Zhang Y, Gong C, Li F, Meng X, Hu X, Yuan Z, Wang F and Chen Y 2022 A bionic interface to suppress the coffee-ring effect for reliable and flexible perovskite modules with a near-90% yield rate *Adv. Mater.* **34** 2201840
- [253] Yu X *et al* 2023 Moisture control enables high-performance sprayed perovskite solar cells under ambient conditions *Mater. Today Energy* **37** 101391
- [254] Chalkias D A, Mourtzikou A, Katsagounos G, Kalarakis A N and Stathatos E 2023 Development of greener and stable inkjet-printable perovskite precursor inks for all-printed annealing-free perovskite solar mini-modules manufacturing *Small Methods* **7** 2300664
- [255] Chen C, Ran C, Guo C, Yao Q, Wang J, Niu T, Li D, Chao L, Xia Y and Chen Y 2023 Fully screen-printed perovskite solar cells with 17% efficiency via tailoring confined perovskite crystallization within mesoporous layer *Adv. Energy Mater.* **13** 2302654
- [256] Wang Y *et al* 2023 Grain boundary elimination via recrystallization-assisted vapor deposition for efficient and stable perovskite solar cells and modules *Adv. Mater.* **35** 2304625
- [257] Tan L *et al* 2023 Combined vacuum evaporation and solution process for high-efficiency large-area perovskite solar cells with exceptional reproducibility *Adv. Mater.* **35** 2205027
- [258] Tong G *et al* 2023 Holistic strategies lead to enhanced efficiency and stability of hybrid chemical vapor deposition based perovskite solar cells and modules *Adv. Energy Mater.* **13** 2300153
- [259] Fan Y, Chen H, Liu X, Ren M, Liang Y, Wang Y, Miao Y, Chen Y and Zhao Y 2023 Myth behind metastable and stable n-hexylammonium bromide-based low-dimensional perovskites *J. Am. Chem. Soc.* **145** 8209–17
- [260] Kim D, Choi H, Jung W, Kim C, Park E Y, Kim S, Jeon N J, Song S and Park T 2023 Phase transition engineering for effective defect passivation to achieve highly efficient and stable perovskite solar cells *Energy Environ. Sci.* **16** 2045–55
- [261] Martani S *et al* 2023 Defect engineering to achieve photostable wide bandgap metal halide perovskites *ACS Energy Lett.* **8** 2801–8
- [262] Afshari H, Sourabh S, Chacon S A, Whiteside V R, Penner R C, Rout B, Kirmani A R, Luther J M, Eperon G E and Sellers I R 2023 FACsPb triple halide perovskite solar cells with thermal operation over 200 °C *ACS Energy Lett.* **8** 2408–13
- [263] Singh P, Soffer Y, Ceratti D R, Elbaum M, Oron D, Hodes G and Cahen D 2023 A-site cation dependence of self-healing in polycrystalline APbI₃ perovskite films *ACS Energy Lett.* **8** 2447–55
- [264] Yin J, Xu Z, Hu Q, Teobaldi G, Liu L M and Prezhdov O V 2023 Tuning octahedral tilting by doping to prevent

- detrimental phase transition and extend carrier lifetime in organometallic perovskites *J. Am. Chem. Soc.* **145** 5393–9
- [265] Cheng Y, Ma J, Luo H, Cai M, Xue T, Yu G, Ren Z, Song Y, Peng S and Zhang Y 2023 Unraveling segregation behavior of inactive secondary phase driven by ion-competition reaction for perovskite-2D PbI₂ heterojunction solar cells *Nano Energy* **115** 108690
- [266] Wang M, Sun H, Wang M, Meng L and Li L 2023 Uracil induced simultaneously strengthening grain boundaries and interfaces enables high-performance perovskite solar cells with superior operational stability *Adv. Mater.* **36** 2306415
- [267] Wang M, Shi Z, Fei C, Deng Z J D, Yang G, Dunfield S P, Fenning D P and Huang J 2023 Ammonium cations with high pK_a in perovskite solar cells for improved high-temperature photostability *Nat. Energy* **8** 1229–39
- [268] Yang Y *et al* 2023 Inverted perovskite solar cells with over 2,000 h operational stability at 85 °C using fixed charge passivation *Nat. Energy* **9** 37–46
- [269] Kuan C-H, Ko Y-A and Wei-Guang Diao E 2023 Surface and interfacial passivations for FASnI₃ solar cells with co-cations *ACS Energy Lett.* **8** 2423–5
- [270] Greve C, Ramming P, Griesbach M, Leupold N, Moos R, Köhler A, Herzig E M, Panzer F and Grüninger H 2023 To stop or to shuttle halides? The role of an ionic liquid in thermal halide mixing of hybrid perovskites *ACS Energy Lett.* **8** 5041–9
- [271] Zhang L *et al* 2024 The issues on the commercialization of perovskite solar cells *Mater. Futures* **3** 022101
- [272] Hossain K, Kulkarni A, Bothra U, Klingebiel B, Kirchartz T, Saliba M and Kabra D 2023 Resolving the hydrophobicity of the Me-4PACz hole transport layer for inverted perovskite solar cells with efficiency >20% *ACS Energy Lett.* **8** 3860–7
- [273] Luo Y, Chitumalla R K, Ham S-Y, Cakan D N, Kim T, Paek S, Meng Y S, Jang J, Fenning D P and Kim M-C 2023 A Si-substituted spirobifluorene hole-transporting material for perovskite solar cells *ACS Energy Lett.* **8** 5003–11
- [274] Karimipour M, Paingott Parambil A, Tabah Tanko K, Zhang T, Gao F and Lira-Cantu M 2023 Functionalized MXene/halide perovskite heterojunctions for perovskite solar cells stable under real outdoor conditions *Adv. Energy Mater.* **13** 2301959
- [275] Hong J, Xu Z, Lungwitz D, Scott J, Johnson H M, Kim Y-H, Kahn A and Rand B P 2023 Mitigating iodine diffusion by a MoO₃-organic composite hole transport layer for stable perovskite solar cells *ACS Energy Lett.* **8** 4984–92
- [276] Ren Y, Wei Y, Li T, Mu Y, Zhang M, Yuan Y, Zhang J and Wang P 2023 Spirobifluorene with an asymmetric fluorenylcarbazolamine electron-donor as the hole transport material increases thermostability and efficiency of perovskite solar cells *Energy Environ. Sci.* **16** 3534–42
- [277] Yu C, Hu Y, Yang J, Huang J, Li B, Wu L and Li F 2022 Efficient and stable inverted perovskite solar cells with TOASiW₁₂-modified Al as a cathode *Adv. Funct. Mater.* **33** 2209290
- [278] Chu Q-Q, Sun Z, Wang D, Cheng B, Wang H, Wong C-P and Fang B 2023 Encapsulation: the path to commercialization of stable perovskite solar cells *Matter* **6** 3838–63
- [279] Tian C *et al* 2023 In situ polymerizing internal encapsulation strategy enables stable perovskite solar cells toward lead leakage suppression *Adv. Funct. Mater.* **33** 2302270
- [280] Castro-Méndez A-F *et al* 2023 Vapor phase infiltration improves thermal stability of organic layers in perovskite solar cells *ACS Energy Lett.* **8** 844–52
- [281] Wang Z, Wang J, Li Z, Chen Z, Shangguan L, Fan S and Duan Y 2023 Crosslinking and densification by plasma-enhanced molecular layer deposition for hermetic seal of flexible perovskite solar cells *Nano Energy* **109** 108232
- [282] Lee J W and Park N G 2019 Chemical approaches for stabilizing perovskite solar cells *Adv. Energy Mater.* **10** 1903249
- [283] Frost J M, Butler K T, Brivio F, Hendon C H, van Schilfgaarde M and Walsh A 2014 Atomistic origins of high-performance in hybrid halide perovskite solar cells *Nano Lett.* **14** 2584–90
- [284] Leguy A M A *et al* 2015 Reversible hydration of CH₃NH₃PbI₃ in films, single crystals, and solar cells *Chem. Mater.* **27** 3397–407
- [285] Song Z, Abate A, Waththage S C, Liyanage G K, Phillips A B, Steiner U, Graetzel M and Heben M J 2016 Perovskite solar cell stability in humid air: partially reversible phase transitions in the PbI₂-CH₃NH₃I-H₂O system *Adv. Energy Mater.* **6** 1600846
- [286] Liu X, Luo D, Lu Z H, Yun J S, Saliba M, Seok S I and Zhang W 2023 Stabilization of photoactive phases for perovskite photovoltaics *Nat. Rev. Chem.* **7** 462–79
- [287] Hidalgo J *et al* 2023 Synergistic role of water and oxygen leads to degradation in formamidinium-based halide perovskites *J. Am. Chem. Soc.* **145** 24549–57
- [288] Meng Y, Sunkari P P, Meilä M and Hillhouse H W 2023 Chemical reaction kinetics of the decomposition of low-bandgap tin-lead halide perovskite films and the effect on the ambipolar diffusion length *ACS Energy Lett.* **8** 1688–96
- [289] Azmi R, Zhumagali S, Bristow H, Zhang S, Yazmaciyan A, Pininti A R, Utomo D S, Subbiah A S and De Wolf S 2023 Moisture-resilient perovskite solar cells for enhanced stability *Adv. Mater.* **36** e2211317
- [290] Raval P, Kennard R M, Vasileiadou E S, Dahlman C J, Spanopoulos I, Chabinyc M L, Kanatzidis M and Manjunatha Reddy G N 2022 Understanding instability in formamidinium lead halide perovskites: kinetics of transformative reactions at grain and subgrain boundaries *ACS Energy Lett.* **7** 1534–43
- [291] Shi L *et al* 2020 Gas chromatography-mass spectrometry analyses of encapsulated stable perovskite solar cells *Science* **368** eaba2412
- [292] Aitola K, Gava Sonai G, Markkanen M, Jaqueline Kaschuk J, Hou X, Miettunen K and Lund P D 2022 Encapsulation of commercial and emerging solar cells with focus on perovskite solar cells *Sol. Energy* **237** 264–83
- [293] You S *et al* 2023 Radical polymeric p-doping and grain modulation for stable, efficient perovskite solar modules *Science* **379** 288–94
- [294] Li B, Li S, Gong J, Wu X, Li Z, Gao D, Zhao D, Zhang C, Wang Y and Zhu Z 2023 Fundamental understanding of stability for halide perovskite photovoltaics: the importance of interfaces *Chem* **10** 35–47
- [295] Sadhu A, Guo Y, Salim T, Sun Q, Mhaisalkar S G, Sum T C and Wong L H 2023 Elucidating the role of chalcogenide-based interface passivators in enhancing the stability of perovskite solar cells *Adv. Funct. Mater.* **33** 2305215
- [296] Ramadan A J 2023 Perovskite solar cells take the heat *Nat. Energy* **8** 1186–7
- [297] Yue T *et al* 2023 A binary solution strategy enables high-efficiency quasi-2D perovskite solar cells with excellent thermal stability *ACS Nano* **17** 14632–43
- [298] Duan G *et al* 2023 Fabricate the compressive-strained perovskite solar cells through the lattice-matching chelation *ACS Energy Lett.* **8** 2308–15
- [299] Wang T, Yang J, Cao Q, Pu X, Li Y, Chen H, Zhao J, Zhang Y, Chen X and Li X 2023 Room temperature nondestructive encapsulation via self-crosslinked fluorosilicone polymer enables damp heat-stable

- sustainable perovskite solar cells *Nat. Commun.* **14** 1342
- [300] Le H K D, Lin C-K, Jin J, Zhang Y, Lin Z, Vailionis A, Tamura N and Yang P 2023 Quantification of strain and its impact on the phase stabilization of all-inorganic cesium lead iodide perovskites *Matter* **6** 2368–82
- [301] Peng S *et al* 2023 Kinetics and mechanism of light-induced phase separation in a mixed-halide perovskite *Matter* **6** 2052–65
- [302] Wu W, Xiong H, Deng J, Wang M, Zheng H, Wu M, Yuan S, Ma Z, Fan J and Li W 2023 Rotatable skeleton for the alleviation of thermally accumulated defects in inorganic perovskite solar cells *ACS Energy Lett.* **8** 2284–91
- [303] Xu Z *et al* 2023 Origins of photoluminescence instabilities at halide perovskite/organic hole transport layer interfaces *J. Am. Chem. Soc.* **145** 11846–58
- [304] Chen Z, Xue H, Brocks G, Bobbert P A and Tao S 2023 Thermodynamic origin of the photostability of the two-dimensional perovskite $\text{PEA}_2\text{Pb}(\text{I}_{1-x}\text{Bx})_4$ *ACS Energy Lett.* **8** 943–9
- [305] Gao Y *et al* 2023 Elimination of unstable residual lead iodide near the buried interface for the stability improvement of perovskite solar cells *Energy Environ. Sci.* **16** 2295–303
- [306] Krishna A *et al* 2023 Mitigating the heterointerface driven instability in perovskite photovoltaics *ACS Energy Lett.* **8** 3604–13
- [307] Du G, Yang L, Dong P, Qi L, Che Y, Wang X, Zhang X and Zhang J 2023 Sequential molecule-doped hole conductor to achieve >23% perovskite solar cells with 3000-hour operational stability *Adv. Mater.* **35** 2303692
- [308] Li X, Yang H, Liu A, Lu C, Yuan H, Zhang W and Fang J 2023 Iodine-trapping strategy for light-heat stable inverted perovskite solar cells under ISOS protocols *Energy Environ. Sci.* **16** 6071–7
- [309] Parkhomenko H P *et al* 2023 Impact of a short-pulse high-intense proton irradiation on high-performance perovskite solar cells *Adv. Funct. Mater.* **34** 2310404
- [310] Yuan G *et al* 2023 Inhibited crack development by compressive strain in perovskite solar cells with improved mechanical stability *Adv. Mater.* **35** 2211257
- [311] Jin B, Ren L, Gou Y, Ma R, Liang Z, Li Z, Dong B, Zhao L, Wang S and Wu C 2023 Fiber-bridging-induced toughening of perovskite for resistance to crack propagation *Matter* **6** 1622–38
- [312] Zhou J *et al* 2023 Modulation of perovskite degradation with multiple-barrier for light-heat stable perovskite solar cells *Nat. Commun.* **14** 6120
- [313] Kirmani A R *et al* 2023 Metal oxide barrier layers for terrestrial and space perovskite photovoltaics *Nat. Energy* **8** 191–202
- [314] Fu G, Lee D-K, Ma C and Park N-G 2023 Disulfidation interfacial engineering toward stable, lead-immobilizable perovskite solar cells *ACS Energy Lett.* **8** 4563–71
- [315] Kim S-G, de Monfreid T, Kim J-H, Goubard F, Berry J J, Zhu K, Bui T-T and Park N-G 2023 Nanographene coupled with interfacial pyrene derivatives for thermally stable perovskite solar cells *ACS Energy Lett.* **8** 2267–75
- [316] Pasha A *et al* 2023 Cationic and anionic vacancy healing for suppressed halide exchange and phase segregation in perovskite solar cells *ACS Energy Lett.* **8** 3081–7
- [317] Kang D-H, Lee S-U and Park N-G 2023 Effect of residual chloride in FAPbI_3 film on photovoltaic performance and stability of perovskite solar cell *ACS Energy Lett.* **8** 2122–9
- [318] Li D, Xing Z, Meng X, Hu X, Hu T and Chen Y 2023 Spontaneous internal encapsulation via dual interfacial perovskite heterojunction enables highly efficient and stable perovskite solar cells *Nano Lett.* **23** 3484–92
- [319] Wang J, Uddin M A, Chen B, Ying X, Ni Z, Zhou Y, Li M, Wang M, Yu Z and Huang J 2023 Enhancing photostability of Sn-Pb perovskite solar cells by an alkylammonium pseudo-halogen additive *Adv. Energy Mater.* **13** 2204115
- [320] Gil-Escrig L *et al* 2023 Efficient and thermally stable wide bandgap perovskite solar cells by dual-source vacuum deposition *Adv. Funct. Mater.* **33** 2214357
- [321] Wu X *et al* 2023 Eco-friendly perovskite solar cells: from materials design to device processing and recycling *EcoMat* **5** e12352
- [322] Yu B, Tan S, Li D and Meng Q 2023 The stability of inorganic perovskite solar cells: from materials to devices *Mater. Futures* **2** 032101
- [323] Wang S, Li M-H, Jiang Y and Hu J-S 2023 Instability of solution-processed perovskite films: origin and mitigation strategies *Mater. Futures* **2** 012102
- [324] Khenkin M *et al* 2024 Light cycling as a key to understanding the outdoor behaviour of perovskite solar cells *Energy Environ. Sci.* **17** 602–10
- [325] Liu W, Raza H, Hu X, Liu S, Liu Z and Chen W 2023 Key bottlenecks and distinct contradictions in fast commercialization of perovskite solar cells *Mater. Futures* **2** 012103
- [326] Jiang Y, Qiu L, Juarez-Perez E J, Ono L K, Hu Z, Liu Z, Wu Z, Meng L, Wang Q and Qi Y 2019 Reduction of lead leakage from damaged lead halide perovskite solar modules using self-healing polymer-based encapsulation *Nat. Energy* **4** 585–93
- [327] Jin X, Yang Y, Zhao T, Wu X, Liu B, Han M, Chen W, Chen T, Hu J-S and Jiang Y 2022 Mitigating potential lead leakage risk of perovskite solar cells by device architecture engineering from exterior to interior *ACS Energy Lett.* **7** 3618–36
- [328] Yang D, Yang R, Priya S and Liu S 2019 Recent advances in flexible perovskite solar cells: fabrication and applications *Angew. Chem., Int. Ed.* **58** 4466–83
- [329] Zhu Y, Hu M, Xu M, Zhang B, Huang F, Cheng Y-B and Lu J 2022 Bilayer metal halide perovskite for efficient and stable solar cells and modules *Mater. Futures* **1** 042102
- [330] Podapangi S K, Jafarzadeh F, Mattiello S, Korukonda T B, Singh A, Beverina L and Brown T M 2023 Green solvents, materials, and lead-free semiconductors for sustainable fabrication of perovskite solar cells *RSC Adv.* **13** 18165–206
- [331] Miao Y, Ren M, Chen Y, Wang H, Chen H, Liu X, Wang T and Zhao Y 2023 Green solvent enabled scalable processing of perovskite solar cells with high efficiency *Nat. Sustain.* **6** 1465–73
- [332] Zhai P, Ren L, Zhang Y, Xu Z, Wu Y, Zhao K, Zhang L and Liu S 2023 Performance-limiting formation kinetics in green water-processed perovskite solar cells *Energy Environ. Sci.* **16** 3014–24
- [333] Zhang Y, Ren L, Zhai P, Xin J, Wu J, Zhang Q, Chen X, Zhao K, Zhang L and (Frank) Liu S 2024 The synergistic effect of dry air and surfactants enables water to be a promising green solvent for stable and efficient perovskite solar cells *Energy Environ. Sci.* **17** 296–306
- [334] Zhang Z *et al* 2023 Green-antisolvent-regulated distribution of p-type self-doping enables tin perovskite solar cells with an efficiency of over 14% *Energy Environ. Sci.* **16** 3430–40
- [335] Xiu J *et al* 2023 A sustainable approach using nanocrystals functionalized green alkanes as efficient antisolvents to fabricate high-quality perovskite films *Adv. Energy Mater.* **13** 2300566
- [336] Yu X, Gao D, Li Z, Sun X, Li B, Zhu Z and Li Z 2023 Green-solvent processable dopant-free hole transporting materials for inverted perovskite solar cells *Angew. Chem., Int. Ed.* **62** e202218752

- [337] Zhang H, Lee J-W, Nasti G, Handy R, Abate A, Grätzel M and Park N-G 2023 Lead immobilization for environmentally sustainable perovskite solar cells *Nature* **617** 687–95
- [338] Wu P, Wang S, Li X and Zhang F 2022 Beyond efficiency fever: preventing lead leakage for perovskite solar cells *Matter* **5** 1137–61
- [339] Li X, Zhang F, He H, Berry J J, Zhu K and Xu T 2020 On-device lead sequestration for perovskite solar cells *Nature* **578** 555–8
- [340] Li X, Zhang F, Wang J, Tong J, Xu T and Zhu K 2021 On-device lead-absorbing tapes for sustainable perovskite solar cells *Nat. Sustain.* **4** 1038–41
- [341] Chen S, Deng Y, Gu H, Xu S, Wang S, Yu Z, Blum V and Huang J 2020 Trapping lead in perovskite solar modules with abundant and low-cost cation-exchange resins *Nat. Energy* **5** 1003–11
- [342] Xu D, Mai R, Jiang Y, Chen C, Wang R, Xu Z, Kempa K, Zhou G, Liu J-M and Gao J 2022 An internal encapsulating layer for efficient, stable, repairable and low-lead-leakage perovskite solar cells *Energy Environ. Sci.* **15** 3891–900
- [343] Chen S S, Deng Y H, Xiao X, Xu S, Rudd P N and Huang J S 2021 Preventing lead leakage with built-in resin layers for sustainable perovskite solar cells *Nat. Sustain.* **4** 636–43
- [344] Xiao X *et al* 2021 Lead-adsorbing ionogel-based encapsulation for impact-resistant, stable, and lead-safe perovskite modules *Sci. Adv.* **7** eabi8249
- [345] Valastro S *et al* 2023 Preventing lead leakage in perovskite solar cells with a sustainable titanium dioxide sponge *Nat. Sustain.* **6** 974–83
- [346] Luo H, Li P, Ma J, Li X, Zhu H, Cheng Y, Li Q, Xu Q, Zhang Y and Song Y 2023 Bioinspired “cage traps” for closed-loop lead management of perovskite solar cells under real-world contamination assessment *Nat. Commun.* **14** 4730
- [347] Yang M, Tian T, Fang Y, Li W-G, Liu G, Feng W, Xu M and Wu W-Q 2023 Reducing lead toxicity of perovskite solar cells with a built-in supramolecular complex *Nat. Sustain.* **6** 1455–64
- [348] Zhang J *et al* 2023 Thermally crosslinked f-rich polymer to inhibit lead leakage for sustainable perovskite solar cells and modules *Angew. Chem., Int. Ed.* **62** e202305221
- [349] Xu Y, Guo X, Lin Z, Wang Q, Su J, Zhang J, Hao Y, Yang K and Chang J 2023 Perovskite films regulation via hydrogen-bonded polymer network for efficient and stable perovskite solar cells *Angew. Chem., Int. Ed.* **62** e202306229